UNIVERSITY OF CALIFORNIA SAN DIEGO

Function of Hole Transport Layer Components in Perovskite Solar Cells

A dissertation submitted in partial satisfaction of the
requirements for the degree Doctor of Philosophy

in

NanoEngineering

by

Shen Wang

Committee in charge:

Professor Ying Shirley Meng, Chair
Professor Darren J. Lipomi
Professor Wei Xiong
Professor Kesong Yang
Professor Paul Yu

2018

The Dissertation of Shen Wang is approved, and it is acceptable in quality and form for publication on microfilm and electronically:

Chair

University of California San Diego

2018

DEDICATION

To my parents: Defeng Wang and Jianhua Wang

To my beloved fiancé, Mengyue Jia

TABLE OF CONTENTS

LIST OF FIGURES

LIST OF TABLES

ACKNOWLEDGEMENTS

Beijing, the city I stayed in for over 7 years to pursue my B.S. and M.S. degrees, suffers from terrible smog during the winter every year. During this time I would see the city sky turn from blue to gray which urged me to want to resolve this issue. This motivated me to pursue photovoltaic devices as my research topic and provide a greener future for Beijing and other cities in my home country. As a student with Chemistry as my background, I hoped my research project could link molecular behaviors with the performance of photovoltaic devices. Thanks to the Laboratory for Energy Storage and Conversion (LESC) at UCSD, I was able to make my dream come true. First of all, I want to take this opportunity to express a deep sense of gratitude to my Ph. D. advisor Prof. Ying Shirley Meng. It has been my great honor to learn and work with Dr. Meng. All this research could not have come true without her constant support, patient guidance, and valuable suggestions. Moreover, she is an excellent role model for the time management and perfect balancing of work and family. I also appreciate the help of Professor Wei Xiong, who gave helpful suggestions that prompted critical thinking on my research and showed me the way to understand and analyze data deeply and carefully. I would also like to thank my committee members: Professor Darren J. Lipomi, Professor Kesong Yang and Professor Paul Yu for their guidance and time.

My mother Ms. Defeng Wang has been my backbone and support to allow me to enjoy this wonderful 5 year academic journey. Also, I am grateful to my father Dr. Jianhua Wang. I still remember how proud I felt to be mentioned in his Ph.D. thesis 14 years ago. Time flies like an arrow; he departed us 6 years ago but he has a special place in my acknowledgment. To be an excellent professor was his unfinished business, and now I feel proud to be on the path to academic success. I especially want to thank to my fiancé Ms. Mengyue Jia for her constant

support, love, and encouragement to finish this thesis. It is extraordinary for us to share the beauty of love, music and science.

I would like to acknowledge my collaborators and co-authors at UC San Diego: Mr. Pritesh Parikh for his indispensable help on my project for materials synthesis, device optimization, daily discussion, and atom probe tomography experiment. Ms. Sophia Valenzuela for her assistance on the hole transport layer preparation and characterization. Dr. Mahsa Sina for her help with TEM experiments, Dr. Xuefeng Wang for his contributions on XPS, and Mr. Yingmin Li for the discussion on FTIR. I appreciate the help of my previous and current undergraduate assistants: Ms. Taylor M. Uekert, Mr. Brian P. Shahbazian, Ms. Zihan Huang, and Ms. Amanda Cabreros. I wish all of them a bright future with their own researches in graduate school. Thanks to Professor David P. Fenning and his graduate students Ms. Yanqi Luo and Ms. Xueying Li for the inspiring discussions. I am grateful for the help from the Laboratory for Energy Storage and Conversion group members (past and present): Dr. Danna Qian, Dr. Haodong Liu, Dr. Chuze Ma, Dr. Judith Alvarado, Mr. Alex C. MacRae, and Mr. Chandler J. Miller.

Additionally, I would like to show my gratitude to my external collaborators and co-authors: Dr. Wen Yuan from Michigan State University, for his inspiration, discussion and support on the Spiro-OMeTAD oxidation study; Ms. Marcella Günther from the University of Würzburg, for her assistance on the tBP-LiTFSI characterizations; Dr. Arun Devaraj from the Pacific Northwest National Laboratory (PNNL), for his guidance and analysis on the APT. Dr. Juan-Pablo Correa-Baena from the Massachusetts Institute of Technology, for his guidance on the perovskite solar cell fabrication.

Finally, I would like to thank my funding resources: the seed funding from the Sustainable Power and Energy Center (SPEC) under the Frontier of Innovation Award by the Vice Chancellor of Research at the University of California San Diego, the Jacobs Graduate Fellowship by Jacobs School of Engineering at UC San Diego, and the California Energy Commission EPIC Advance Breakthrough Award (EPC-16-050).

Chapter 5, in full, is a reprint of the material "Spectrum-dependent Spiro-OMeTAD Oxidization Mechanism in Perovskite Solar Cells" as it appears in the ACS Applied Materials & Interfaces, Wang, S., Yuan, W., Meng, Y. S., 2015, 7(44), 24791. The dissertation author was the primary investigator and first author of this paper. All of the tests were performed and analyzed by the author.

Chapter 6, in full, is a reprint of the material "Role of 4-tert-Butylpyridine as a Hole Transport Layer Morphological Controller in Perovskite Solar Cells", Nano Letters, Wang, S., Sina, M., Parikh, P., Uekert, T., Shahbazian, B., Devaraj, A., Meng, Y. S., 2016, 16(9), 5594. The dissertation author was the primary investigator and co-first author of this paper. All of the experiment parts were performed and analyzed by the author except for the energy-filtered transmission electron microscope and atom probe tomography.

Chapter 7, in full, is a reprint of the material "tBP-LiTFSI Complexes in Perovskite Solar Cells", Wang, S., Huang, Z., Wang, X., Li, Y., Günther, M., Valenzuela, S., Parikh, P., Xiong, W., Meng, Y. S., 2018 (in preparation). The dissertation author was the primary investigator and first author of this paper. All of the experiment parts were performed by the author except for the XPS.

VITA

2010 Bachelor of Science in Chemistry

Peking University

2013 Master of Science in Condensed Matter Physics

Chinese Academy of Sciences

2018 Doctor of Philosophy in NanoEngineering

University of California San Diego

PUBLICATIONS

(* authors contributed equally to the work)

1. **Wang, S**., Zhang, Q. X., Xu, Y. Z., Li, D. M., Luo, Y. H., Meng, Q., "Single-step in-situ Preparation of Thin Film Electrolyte for Quasi-solid State Quantum Dot-sensitized Solar Cells", Journal of Power Sources, 2013, 224, 152

2. Yuan, W., Zhao, H., Hu, H., **Wang, S.**, Baker, G. L., "Synthesis and Characterization of the Hole-conducting Silica/Polymer Nanocomposites and Application in Solid-state Dye-sensitized Solar Cell", ACS Applied Materials & Interfaces, 2013, 5(10), 4155

3. Zhang, X., Huang, X., Yang, Y., **Wang, S.**, Gong, Y., Luo, Y., Li, D., Meng, Q., "Investigation on New $CuInS_2$/Carbon Composite Counter Electrodes for CdS/CdSe Cosensitized Solar Cells", ACS Applied Materials & Interfaces, 2013, 5(13), 5954

4. **Wang, S.**, Yuan, W., Meng, Y. S., "Spectrum-dependent Spiro-OMeTAD Oxidization Mechanism in Perovskite Solar Cells", ACS Applied Materials & Interfaces, 2015, 7(44), 24791

5. **Wang, S.***, Sina, M. *, Parikh, P., Uekert, T., Shahbazian, B., Devaraj, A., Meng, Y. S., "Role of 4-tert-Butylpyridine as a Hole Transport Layer Morphological Controller in Perovskite Solar Cells", Nano Letters, 2016, 16(9), 5594

6. Zhu, C., Yang, L., Seo, J. K., Zhang, X., **Wang, S.**, Shin, J., Chao, D., Zhang, H., Meng, Y.S. Fan, H.J., "Self-branched α-MnO_2/δ-MnO_2 Heterojunction Nanowires with Enhanced Pseudocapacitance", Materials Horizons, 2017, 4(3), 415

7. Alvarado, J., Ma, C., **Wang, S.**, Nguyen, K., Kodur, M., Meng, Y. S. "Improvement of the Cathode Electrolyte Interphase on P2-$Na_{2/3}Ni_{1/3}Mn_{2/3}O_2$ by Atomic Layer Deposition", ACS Applied Materials & Interfaces, 2017, 9(31), 26518

8. Wang, X., Zhang, M., Alvarado, J., **Wang, S.**, Sina, M., Lu, B., Bouwer, J., Xu, W., Xiao, J., Zhang, J., Liu, J., Meng, Y. S., "New Insights on the Structure of Electrochemically Deposited Lithium Metal and its Solid Electrolyte Interphases via Cryogenic TEM", Nano Letters, 2017, 17(12), 7606

9. Root, S. E., Carpenter, C. W., Kayser, L. V., Rodriquez, D., Davies, D. M., **Wang, S.**, Tan, S. T. M., Meng, Y. S., Lipomi, D. J. "Ionotactile Stimulation: Nonvolatile Ionic Gels for Human–Machine Interfaces", ACS Omega, 2018, 3(1), 662

10. Wang, X., Li, Y., Bi, X., Ma, L., Wu, T., Sina, M., **Wang, S.**, Zhang, M., Alvarado, J., Lu, B., Banerjee, A., Amine, K., Lu, J., Meng, Y.S., "Hybrid Li-Ion and Li-O_2 Battery with Zero-Polarization Enabled by Oxyhalogen-Sulfur Electrochemistry", Joule, 2018 (under review)

11. **Wang, S.**, Huang, Z., Wang, X., Li, Y., Günther, M., Valenzuela, S., Parikh, P., Xiong, W., Meng, Y. S., "tBP-LiTFSI Complexes in Perovskite Solar Cells", 2018 (in preparation)

12. Fang,Y., Ran, S., Xie, W., **Wang, S.**, Meng, Y. S., Maple, M. B., "Transition from Semiconducting to Metallic Ground State in High-Quality Single Crystalline FeSi", Proceedings of the National Academy of Sciences of the United States of America, 2018 (under review)

13. Correa-Baena, J.-P., Luo, Y., Brenner, T. M., Snaider, J., Sun, S., Li, X., Jensen, M. A., Nienhaus, L., Wieghold, S., Poindexter, J. R, **Wang, S.**, Meng, Y. S., Wang, T., Lai, B., Bawendi, M. J., Huang, L., Fenning, D. P., Buonassisi, T., "Homogenization of Halide Distribution and Carrier Dynamics in Alloyed Organic-Inorganic Perovskites", Science, 2018 (under review)

ABSTRACT OF THE DISSERTATION

Function of Hole Transport Layer Components in Perovskite Solar Cells

by

Shen Wang

Doctor of Philosophy in NanoEngineering

University of California, San Diego, 2018

Professor Ying Shirley Meng, Chair

The perovskite solar cell (PSC) is a photovoltaic device. With the tunable bandgap, long carrier diffusion length, and low exciton binding energy of various perovskite materials, power conversion efficiency (PCE) of 22.7% has been achieved. Though PSCs have high energy conversion efficiencies and low manufacturing cost, low device stability limits its further application and commercialization.

One of the major bottlenecks hindering the improvement of device stability is the interaction of components in the hole transport layer: lithium bis(trifluoromethanesulfonyl)imide (LiTFSI) and 4-tert-butylpyridine (tBP). LiTFSI is hygroscopic and accelerates perovskite decomposition. tBP, which evaporates easily, is corrosive to perovskite materials. Previous research has assumed that tBP and LiTFSI have similar working mechanisms in perovskite solar cells as what they performed in solid-state dye-sensitized solar cells (ss-DSSCs). However, due to the different device configurations and functional layers, it is necessary to understand the actual functions of these hole transport layer components in PSCs in order to further improve device stability and efficiency.

In our study, a spectrum-dependent mechanism for the oxidation of hole transport material 2,2′,7,7′-tetrakis(N,N-di-p-methoxyphenylamine)-9,9′-spirobifluorene (Spiro-OMeTAD) with LiTFSI in PSCs was proposed. The perovskite layer plays different roles in the Spiro-OMeTAD oxidization for various spectral ranges. Regarding tBP, we confirmed its role as a HTL morphology controller in PSCs for the first time. Our observations suggest that tBP significantly improves the uniformity of the HTL and avoids accumulation of LiTFSI. We also observed the formation of tBP-LiTFSI complexes in PSCs. These complexes in PSCs can alleviate the negative effects of tBP and LiTFSI while maintaining their positive effects on perovskite materials. Consequently, a minor change of tBP:LiTFSI ratio displays huge influences on the stability of perovskite. As a result, the PSCs fabricated with our suggested tBP:LiTFSI ratio have decreased efficiency variation with enhanced device stability. Our understanding of the functions of these hole transport layer components and perovskite on a molecular level paves the way for further improvements to PSCs performance.

Chapter 1. Motivation and Outline

Human and social development is strongly reliant on energy. Fossil fuels, the primary energy resource, exhaust much faster than renewables. On the other hand, pollution due to the usage of fossil fuels is still unavoidable. Combustion of fossil fuels can generate sulfur dioxides, nitrogen oxides, harmful organics, heavy metals, and even radioactive materials.[1] Carbon dioxide, the main product from combustion of fossil fuels, has a net increase of 10.65 billion tons per year.[2] Though under debate in US government nowadays, global attention has been drawn to eliminate this greenhouse gas to protect the earth.

Solar energy, the light and heat radiant from the sun, is considered as one of the candidates to substitute fossil fuel energy. It is clean, renewable and abundant. The total solar energy which is adsorbed by earth within 1 hour can support the energy usage cross the entire world for 1 year.[3] However, due to the light intensity variation and low energy density across the globe, new techniques need to be developed to apply solar energy efficiently. Solar cells are a series of photovoltaic devices which can convert solar power into electricity. China and India, two of the largest developing countries in the world, claim that by 2040 the share of all renewables in total power generation will reach 40%.[4]

There are three generations of solar cells that have been developed since the first silicon-based solar cell demonstrated at Bell Laboratory in 1954.[5] The first generation of solar cells is based on mono/poly crystalline silicon materials which combine the n-doped and p-doped silicon to form a p-n junction. The abundance of silicon in the earth's crust and the high stability of Si-based device enable the first generation of solar cells to still be the dominant photovoltaic device in the market.[6] However, the high purity requirement of the materials and high manufacturing

temperature which increases its cost, limits the further application for silicon solar cell to compete with other novel energy conversion devices. [6]

The second generation of solar cells were then designed and developed to overcome the shortcomings of traditional Si-based photovoltaic devices. This generation of solar cells is based on thin film devices. Semiconductor materials such as CdTe, $CuInGaSe_2$, and amorphous silicon have been applied in this generation of devices, bringing down the manufacturing cost. Moreover, the low device manufacturing temperature enables these materials to be applied on various substrates such as glass, polymers, and metal foils. This enables photovoltaic devices to be used for multiple purposes: such as power grid, soft electronics and even wearable devices.[7] But the toxicity of the elements in thin film solar cell drew public concern although recycling of the device materials is under fast development. On the other hand, the scarcity of materials in these devices limits its further marketing.[8]

The third generation of solar cells is based on nano, polymeric, or organic materials. Organic photovoltaic devices, dye-sensitized solar cells, quantum-dot solar cells, perovskite solar cells and other recently developed photovoltaic devices all belong to this generation. Some fabrication methods such as doctor-blading, chemical bath deposition, and roll-to-roll technology have been applied for the fabrication of these devices. These methods can further reduce the manufacturing cost compared with the first two generations of solar cells. The abundance of carbon element guarantees that an even cheaper price of the third generation solar cells is achievable. The low fabrication temperature for these devices ensures the third generation solar cells can be applied on flexible and stretchable substrates. However, comparing with the first two generations of solar cells, the efficiency and stability of third generation solar cells is relatively low.[9] Majority of the third generation solar cells' energy conversion efficiency is around 10%

while the first two generation devices are over 20%.[10] The commercialization of the third generation of solar cells is still under development. Figure 1.1 displayed different solar cells and their best efficiency:

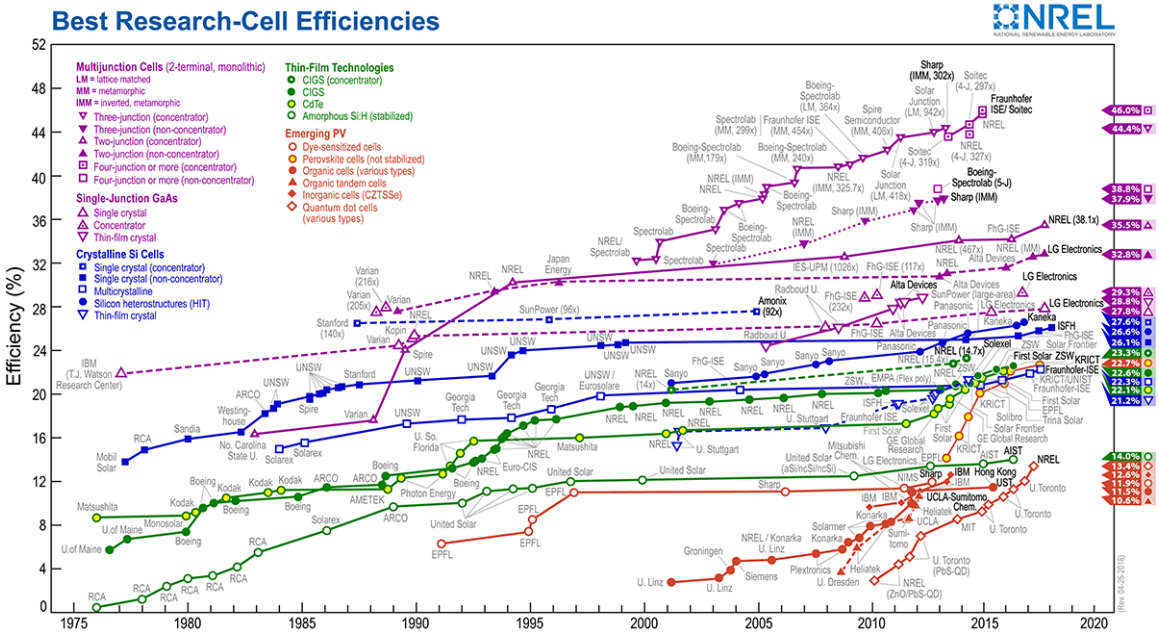

Figure 1.1 Best Research-Cell Efficiencies[10]

A perovskite solar cell is an emerging photovoltaic device that has been developed since 2009.[11] In past 9 years, the efficiency has improved from 3.8% to 22.7%.[10] The devices are based on halide perovskite with a p-i-n configuration. The high energy conversion efficiency can compete with the first two generation devices. Unlike a traditional dye-sensitized solar cell based on a solid-liquid junction, the perovskite solar cell is all solid state which can reduce the encapsulation cost. The major issue which limits the commercialization of perovskite solar cell is its stability.[12] Light, oxygen and moisture are all factors that influence the stability of perovskite materials. On the other hand, majority of the hole transport materials used have lower stability than perovskite materials which can be considered as the bottleneck to further limit the device

stability. Moreover, moisture and oxygen can diffuse through the hole transport layer and then interact with perovskite layer, that means it is crucial to improve the device stability by enhancing the hole transport layer stability.[13] My research focuses on understanding the function and working mechanisms of the hole transport layer components in the perovskite solar cells. The understanding of these components can point out the clear direction to further enhance the device performance.

In the first part of my thesis, the objectives are to develop perovskite solar cells with high performance. Different configurations of perovskite solar cells were designed and fabricated in past few years in our laboratory to finally achieve near 20% light-to-electricity conversion efficiency. The objectives in the second part of my thesis are to understand the function and working mechanisms of hole transport layer components in perovskite solar cells. Actually these two parts mutually influence each other: the understanding of functions for the hole transport layer components helped with the development of high performance perovskite solar cells, and vice versa. **Chapter 2** gives a brief introduction on perovskite solar cells and all its functional layers in devices. The advanced characterization techniques I applied in my thesis are introduced in **Chapter 3**. It includes focused ion beam and transmission electron microscope. **Chapter 4** focuses on the rational design and fabrication of high performance perovskite solar cells in our laboratory. Two configurations of perovskite solar cells were fabricated: One is with mesoporous TiO_2 as the electron transport layer while another one is based on the planar SnO_x. **Chapter 5** mainly discuss the functions of LiTFSI in the hole transport layer of perovskite solar cells and how it oxidize the hole transport materials to influence the device performance. **Chapter 6** aims at the roles of tBP in perovskite solar cells. As the only liquid components in device, it greatly impacts the hole transport layer morphology and device stability. **Chapter 7** shows that

complexes are formed between tBP and LiTFSI. The formation of tBP-LiTFSI complexes alleviates the negative effects of these materials in perovskite solar cells while maintains their positive effects. Based on the understanding of tBP-LiTFSI complexes, a new tBP:LiTFSI ratio was suggested to substitute the empirical ratio which is applied by most laboratories in this field. **Chapter 8** is the summary for these studies. Future work is also discussed in this chapter.

Chapter 2. Introduction

2.1. Introduction of Perovskite Solar Cells (PSCs)

The first perovskite solar cells (PSCs) research was inspired by the dye-sensitized solar cells- a solid-liquid junction photovoltaic device which was had been studied since 1991.[14] The perovskite materials was defined as the sensitizer and loaded on meso-porous TiO_2. This sensitized-photoanode was immersed in iodide-based liquid electrolyte with a 3.8% efficiency.[11] This work was reported in 2009 by Professor Miyasaka group which applied $CH_3NH_3PbI_3$ and $CH_3NH_3PbBr_3$ perovskite materials. The main reason for the relatively low efficiency could be attributed to the instability of perovskite solar cell in iodide electrolyte. Later then, the first solid-state perovskite solar cell was reported in 2012 with 10.2% efficiency.[15] Though it was termed as a solid-state hole transport layer materials in dye-sensitized solar cells from this work, it actually functioned as both a photo absorber and a hole transport layer. The actual all-solid-state perovskite solar cell was reported in late 2012. Professor Henry Snaith from University of Oxford introduced the solid-state organic molecule 2,2',7,7'-Tetrakis-(N,N-di-4-methoxyphenylamino)-9,9'-spirobifluorene (Spiro-OMeTAD) as the hole transport layer materials, which can prevent the dissolution of perovskite absorber to improve the device stability.[16] Near 10% efficiency was achieved by applying meso-porous TiO_2 as the photoanode in the perovskite device. Further experiments show that 12% efficiency for the perovskite solar cells which applied porous Al_2O_3 scaffold. In 2013, planar structure perovskite solar cell was developed with a 15% efficiency.[17] Unlike previous publication the perovskite absorber layer was prepared based on solution-process such as spin-coating, the perovskite film in this work was made by co-evaporation method. Another breakthrough method was reported by Professor

Michael Gratzel's lab, sequential deposition method was applied to prepare much denser perovskite film which also achieved over 15% efficiency in meso-porous structure devices.[18] The structures for all the devices mentioned before, can be termed as 'n-i-p' structure, which electron transport layer was on conductive glass side while hole transport layer was connected with metal contacts. In the same year, the 'inverted' or 'p-i-n' structure PSCs was reported with 10% efficiency. The hole transport layer was on conductive glass side, while the electron transport layer was contacted with metal.[19] Later, the performance was further improved to compete with the 'n-i-p' PSCs.[20] In following years, more new architectures of PSCs had been reported, such as hole-transport layer-free PSCs, electron-transport layer-free PSCs and tandem PSCs.[21–23] The performance was increased from 3.8% in 2009 to 22.7% in late 2017.[10] Typical structures of PSCs were shown in Figure 2.1:

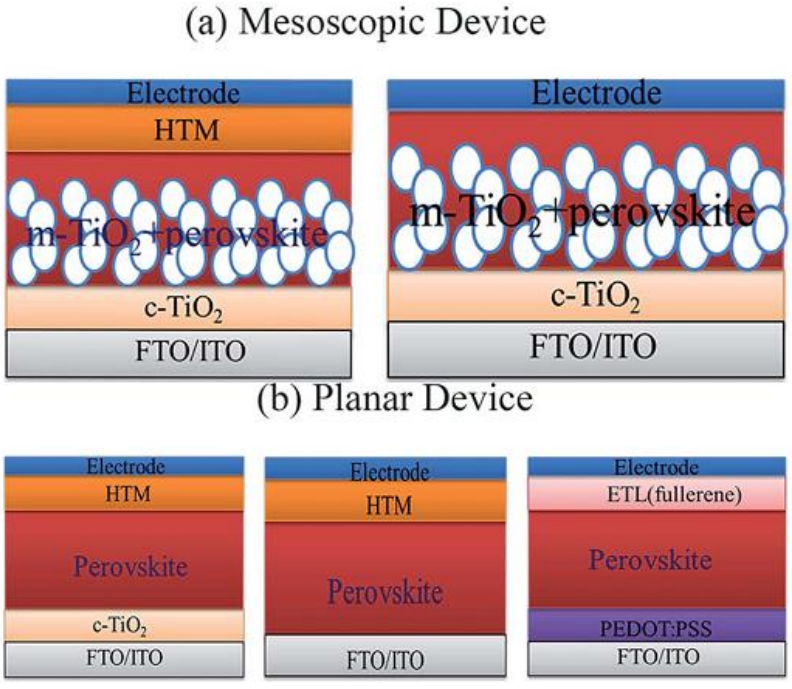

Figure 2.1 Different structures of perovskite solar cells [24]

There are three different layers in perovskite solar cells: The perovskite layer acts as the intrinsic layer in the device which generates electron-hole pairs after absorb photon from sun light. The electrons can be captured by the conduct band of electron transport layer, then the electrons will go to the external circuit. Later, the electrons can be recaptured by the hole transport layer to regenerate the excited perovskite layer to finish the entire cycle. Ideally, there is no compositional change during the entire cycle which can guarantee the long-term stability of the device.[25] On the other hand, these are several recombination process to limit the device performance: The injected electrons in the conduct band of electron transport layer can be either captured by the valence band of perovskite or hole transport layer. Also, the excited electrons in perovskite materials be captured by the valence band of hole transport layer. Some general radiation recombination processes in silicon solar cells exist in PSCs as well. To limit these charge recombination processes can be the pathway to enhance the performance of perovskite solar cells. The entire charge transfer/recombination processes were shown in Figure 2.2:

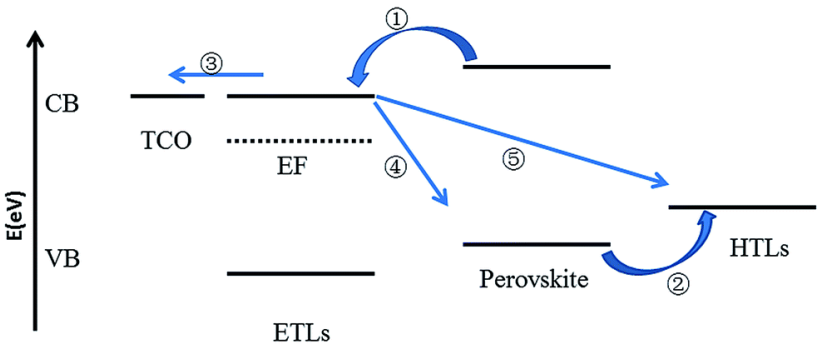

Route 1: Electron injection
Route 2: Hole injection
Route 3: Electron transport and collection
Route 4: Charge recombination in the interface between ETLs and perovskite
Route 5: Charge recombination between electrons in ETLs and the holes in HTLs

Figure 2.2 Charge transfer/recombination processes in PSCs [24]

The photocurrent hysteresis had been reported in PSCs. The photo-currents were different in the forward and reverse scanning directions during the device measurements. The reverse scan always has higher photocurrent then the forward scan as shown in Figure 2.3. This phenomenon enables the report of the device performance parameters more difficult: Either scan direction can not reflect the actual device performance.[26] There are several reasons to cause the hysteresis: The ion migration in perovskite film[27], the ferroelectricity in perovskite materials[28] and the ion diffusion cross hole transport layer and perovskite films[29]. Since there are multiple factors to cause the photocurrent hysteresis, nowadays, the main reason for the photocurrent hysteresis still under debate in perovskite solar cells.

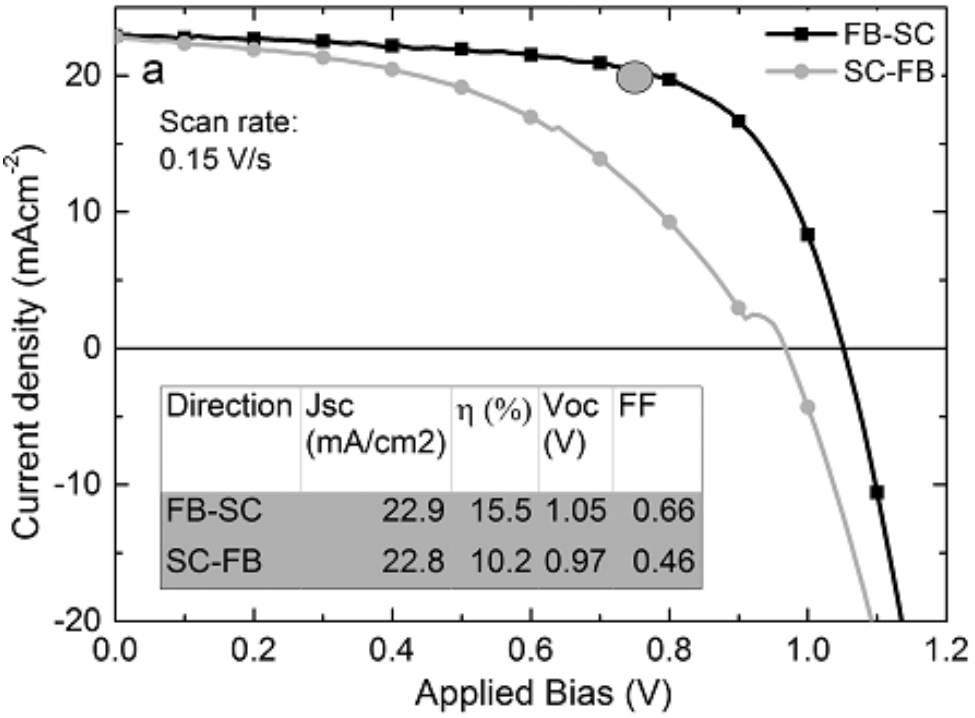

Figure 2.3 Hysteresis in PSCs: the J-V curves of the same PSC are different for the forward and reverse scan direction[26]

Following sessions will discuss about the different layers in perovskite solar cells.

2.2. Perovskite Intrinsic Layer

2.2.1 Structures and Physical Properties

Halide perovskite layer is the 'heart' in PSCs since it is the material to generate electron-hole pairs in devices. It can be considered as the intrinsic layer in PSCs, although it can be synthesized as a weakly p-type or n-type semiconductor (depending on its precursor composition).[30]

Perovskite was discovered in 1839, Russia and named by Lev Perovski. The material was orthorhombic CaTiO3.The general chemical formula for perovskite is ABX3. 'A' and 'B' are two different cations while X is an anion. The crystal structure for perovskite materials is shown in Figure 2.4.

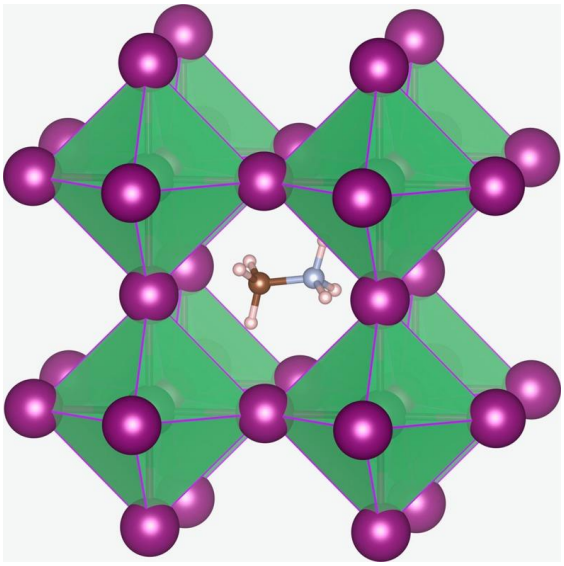

Figure 2.4 Perovskite Crystal Structure ($CH_3NH_3PbI_3$, Methylammonium cation occupies the central A site surrounded by 12 nearest-neighbor iodide ions in corner-sharing PbI_6 octahedral.)[31]

Both A and B sites are coordinated with X: The A site is in 12-fold coordination and the B site is in 6-fold coordination. To maintain a perovskite structure, the atomic radius for A, B and C ions are crucial. It can be evaluated by the tolerance factor t:

$$t' = \frac{r_A + r_X}{\sqrt{2}\,(r_B + r_X)} \qquad \text{(eq 2.1)}$$

In the equation, rA, rB and rx are the radius for A, B, and X respectively. The perovskite crystal structure is stable if the tolerance factor is within the range of 0.75 ~ 1.

The perovskite materials applied in PSCs are halide-based. The X site is halide such as I, Br or Cl. A site is methylammonium (MA), formamidinium (FA), or Cs. B site is Pb, Sn or Ge.[13] The halide perovskite materials is one of the best light absorbers since it has a direct bandgap near 1.33 eV- the bandgap of visible light.[32] The changeable composition is relevant with a tunable bandgap from 1.2 eV to 3.1 eV.[33] This tunable bandgap is decided by the size of ions in perovskite materials. Generally, a larger A or and X ion can reduce the band gap while a larger B ion can increase the bandgap. The exciton binding energy for halide perovskite materials is only between 4-53 meV. It ensures the charge extraction for these carriers is by drifting and diffusion which is more effective. On the other hand, perovskite materials also have long carrier diffusion lengths. Through perovskite single crystal measurements, its carrier diffusion length was calculated to be from 10-175 um, which is much longer than the film thickness in actual PSCs device.[34] Hence the carrier recombination is the limiting step. Temperature dependent phase changes was observed in perovskite, for example, there are three phases for $MAPbI_3$ perovskite at different temperatures: orthorhombic (<270K), tetragonal (270K-420K), and cubic phases (>420K).[35]

Ion Migration was observed in perovskite solar cells either under bias voltage, light or thermal conditions. Both halide ion and A site have been shown to migrate.[27,29] This ion migration triggers at least two impacts: 1 It helps with the self-doping of perovskite materials, which improves the carrier mobility. 2 Some migrations are irreversible, which finally impacts the devices stability.[36] The ion migration in perovskite film can even cross the hole transport layer to react with metal contacts to generate non-conductive barrier layer.[37]

2.2.2 Synthesis Methods and Additives

The halide perovskite materials is easy to synthesis: Unlike the Si-based semiconductor, or materials in the thin film solar cells which need high vacuum or high temperature conditions, majority of perovskite materials can be made by solution-based method at low temperature (<150 ℃). Spin-coating, sequential deposition, and doctor blading all can be applied for perovskite film preparation.[17,18,38] This is because of the low crystallization activation energy of perovskite (around 56.6-97.3 kJ/mol).[39] Figure 2.5 lists the general methods for preparing perovskite films.

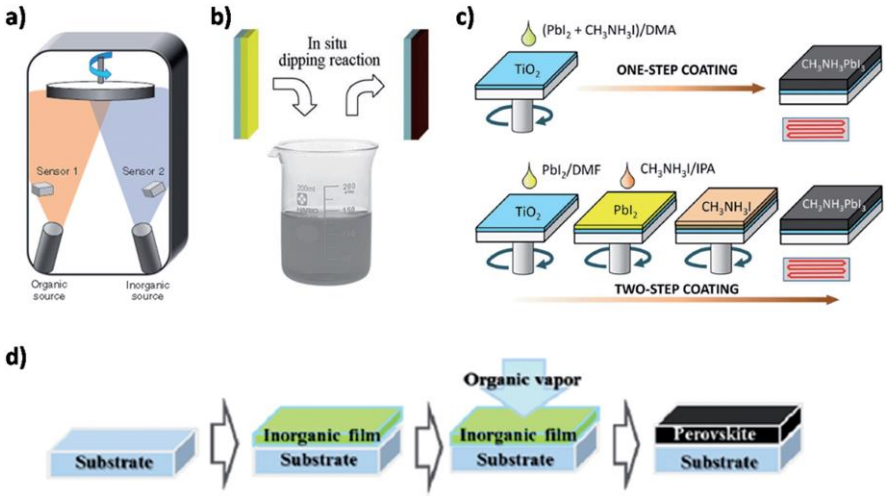

Figure 2.5 Different methods for preparing perovskite films [40]

The most frequently applied method is spin-coating. It consists of two different approaches: Single-step or one-step spin-coating method, which normally dissolves all components in one solvent (or mixed solvents). At the very end during the spin-coating of the solution, an anti-solvent which has low solubility to perovskite is poured onto the substrate to help with the crystallization of the perovskite from its intermediate state.[41] Another procedure is called 'sequential deposition' method: One of the precursors such as lead halide can be spin-coated onto the substrate first, then the entire substrate can be immersed in the solution of another precursor to convert into perovskite.[18] Solvents play a significant role in both methods since it can control the crystal growth process. The crystal growth rate is among the highest in DMF-based solution which results in poor surface coverage.[42] In this case, small amount of DMSO mixed with DMF to suppress the crystal growth lead to dense and uniform film coverage.

Some Lewis bases were added into perovskite solutions as shown in Figure 2.6 to either generate meta-stable intermediate state to improve film uniformity or passivate the surface defects of the device.[43]

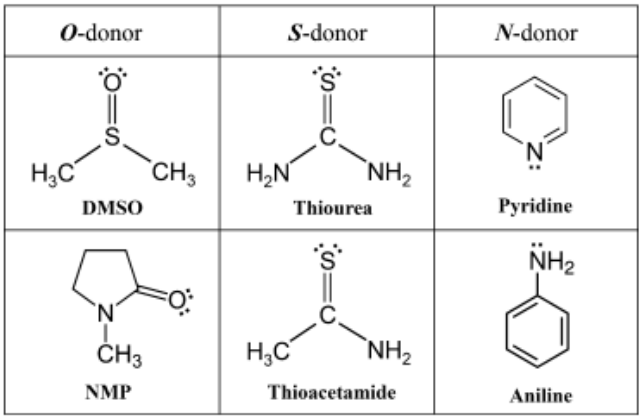

Figure 2.6 Lewis bases with oxygen donor (O-donor), sulfur donor (S-donor), and nitrogen donor (N-donor) in perovskite materials [43]

Actually, DMSO, the solvent in perovskite solution can also be considered as the Lewis base to play the similar role. With additional amount of Methylamine as the additive in DMF-based solution, better film coverage is achievable as well.[44] Methylamine gas was also applied as a post-treatment material to heal the defects in perovskite films.[45] With Lewis base tri-iodide in perovskite precursor solution, 22.1% efficiency was achieved in PSCs, the tri-iodide can reduce the deep defects in perovskite materials. [46]

Some groups also introduced polymers to improve the film quality, such as polyethylene glycol (PEG)[47] or polyvinyl pyridine(PVP)[48]. These polymers can improve the hydrophobicity of perovskite films and also act as a Lewis base to reduce the defects in perovskite materials.

2.2.3 Stability for Perovskite materials

The stability of perovskite materials is the main issue to limit the commercialization of PSCs. Moisture, oxygen, and light are all factors that can cause the degradation of perovskite.

Though according to previous reports, a small amount of moisture can be beneficial to device performance[49], water is still the main reason to degrade perovskite. Take $CH_3NH_3PbI_3$ perovskite as an example, the degradation involves several steps: Firstly, water can form an intermediate state with perovskite materials; this intermediate state is easy to decompose into PbI_2 and CH_3NH_3I. Water functions as the catalyst for the first two steps.[50] After that, CH_3NH_3I can further decomposed to CH_3NH_2 and HI while PbI_2 will react with moisture to form PbO.[51] The degradation from perovskite to PbI_2 and CH_3NH_3I is sort of 'acceptable' since the PbI_2 can be recycled by polar aprotic solvent to re-synthesize the perovskite materials, however, the formation of PbO can further enhance recycling difficulty. [52]

Oxygen can form free radicals in light condition together with TiO2, the free radical is detrimental to perovskite materials, especially for the organic components.[53] On the other hand, Oxygen is also crucial in some hole transport materials such as Spiro-OMeTAD.[54–56] The existence of oxygen can improve the hole conductivity of Spiro-OMeTAD which can finally improve the device performance.

The light-induced degradation can be divided by two parts: firstly, light generates multi-carriers in perovskite materials, the high density of carriers in perovskite materials can trigger the further degradation.[57] The second part is the light-induced thermal effects, which can also degrade perovskite materials.[58] Surprisingly, a recent work shows that, light can also be the key factor to improve the stability of device. A perovskite which contains FA, MA and Cs as the cation, shows that the exposure of light can trigger the crystal expansion effect to reduce the structural defects, as a result, the performance reached over 20.5% with over 1500 hours aging test under 1 sun.[59]

Other factors such as I_2 vapor,[57] components in hole transporting layer,[60] and ion migration[36] can also be the factors to influence the stability of perovskite materials.

2.3 Electron Transport Layer

Electron transport layer (ETL) is the layer which transfers the electrons generated from perovskite intrinsic layer. According to their functions, there are three different types of electron transport layers: the first type of electron transport layer is the n-type materials which only has the function to transfer electrons. For instance, the mesoporous TiO_2 normally plays this role in PSCs. In conventional PSCs, a blocking layer normally in-between of the electron transport layer and conductive glass is also used. It functions to block the electrons from being recaptured by the

hole transport layer. Materials with nano-structures are normally applied in this type of electron transport layer, such as nanotube, nanorod, nanowire, or nanocrystalline mesoporous layer.[18,61,62] The second type of electron transport layer still has the same function, however, it is for the inverted-structure PSCs. A blocking layer is normally in-between of this layer and the metal back contact. According to morphology, this layer normally prepared as a dense-thin film. The reason is because the perovskite has been deposited beneath this layer, thus a planar structure already can have the maximum contact area on the perovskite/electron transport layer interface. Organic hole electron transport layer such as organic [6,6]-phenyl-C61-butyric acid methyl ester (PCBM) can be attributed to this type of electron transport layer.[63,64] The third type of electron transport layer is bifunctional layer, which functions both as the electron transport layer and blocking layer. It is normally a thin film in between of perovskite layer and conducting glass. For instance, SnO_x in planar PSCs functioned in this way.[65] It requires that the layer should be dense enough to maximize the shunt resistance of the device and also thin enough to bring down the series resistance. Materials in the electron transport layer also have three different types: inorganic materials, organic materials, and polymers. An ideal electron transport material has a conduction band that aligns with the conduction band edge of perovskite materials, with faster electron transfer time than its recombination speed with the hole transport layer, and also a uniform contact with perovskite materials. Moreover, in conventional PSCs, the ETL should be transparent in order to maximize the incident photons captured by perovskite materials.[66]

One of the most frequently applied ETL materials is the anatase mesoporous TiO2. Its application in PSCs was inspired by dye-sensitized solar cells, which normally uses this material. The size of the nanocrystal TiO2 is around 20-30 nm and the pore size is above 50 nm. The perovskite band edge aligns with the conduction band of anatase TiO2. The nanocrystal and

mesoporous structure of the film, ensure high loading amount of perovskite materials.[18] However, the necessity of the high perovskite loading amount is questionable due to the ultra-high absorption coefficient of perovskite materials.[40] Several previous world records efficiency of PSCs applied meso-porous TiO2 as the ETL.[18,42,46] To further improve the electron conductivity, Li doping in TiO2 had been applied in several groups which improve the conductivity of the ETL and reached over 20% efficiency.[67] At the same time, there are several problems for mesoporous TiO2 in PSCs. It has a high annealing temperature (from 450 ℃ to 500 ℃), which limits its application to flexible substrates, also with more input energy the fabrication cost increases. On the other hand, the perovskite/TiO2 interface is unstable under intense light condition. The TiO2 can act as a catalyst to decompose the organic components in perovskite materials. [53]

Meso-porous Al_2O_3 ETL had been applied to substitute TiO_2, with higher stability and comparable efficiency even though its band edge does not align with perovskite materials. The authors proposed a mechanism that the electrons of perovskite do not need to cross the bulk of the ETL, the electrons can be transferred on the surface state of Al_2O_3.[16] SnO_x and ZnO have also been applied in PSCs. Both of them can be prepared in conventional device and inverted device with improved stability and lower fabrication temperature.[68,69] Figure 2.7 listed several materials for the ETL in PSCs.

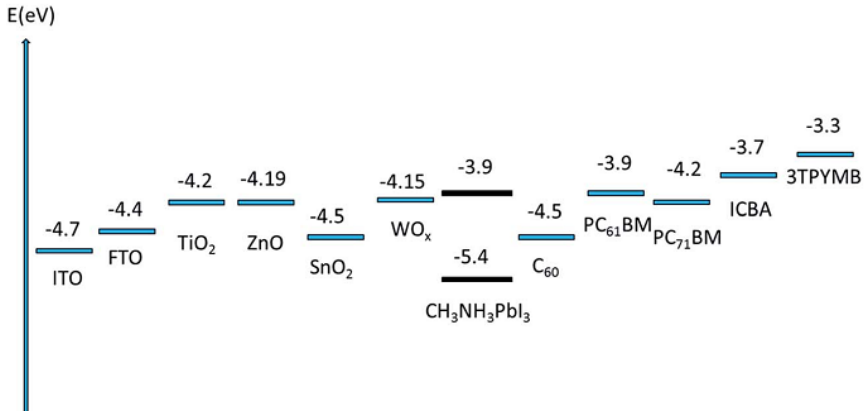

Figure 2.7 Materials for ETL in PSCs showing conduct band minimum/LUMO levels[24]

2.4 Hole Transport Layer

The ideal hole transport layer (HTL) should have high hole mobility (at least $>10^{-4}$ (cm^2 V^{-1} s^{-1})), close alignment with valence band of perovskite, good conductivity, and higher stability. Organic, inorganic and polymeric materials are all applied as the hole transport layer in PSCs. Figure 2.8 displayed the band diagram of HTL with their highest efficiency in perovskite solar cells. [70]

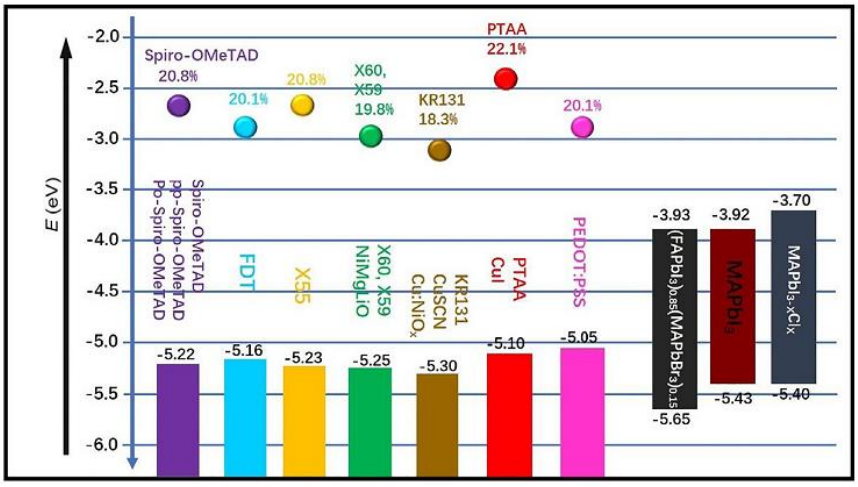

Figure 2.8 Schematic energy-level diagrams for representative HTMs used in PSCs including the most efficient perovskite light absorbers[70]

2.4.1 Organic Hole Transport Materials

Small organics can be easily dissolved in an organic solvent and because of its small size, it is good to contact with perovskite layer no matter which morphology the perovskite layer will be in. All of its physical properties can be adjusted by modifying its functional groups. Moreover, it has low price potentially, since majority of the elements in these type of HTL is abundant elements such as carbon, hydrogen and nitrogen.

One of the most frequently applied small organic hole transport materials in PSCs is 2,2,7,7-tetrakis(N,N-di-p-methoxyphenylamine)-9,9-spirobifluorene (Spiro-OMeTAD). This material had been applied in dye-sensitized solar cell prior to its use in PSCs. It had been introduced in PSCs to substitute the liquid electrolyte which not only improves the device stability, but also enhances the efficiency.[16,71] The triarylamine and spiro structure prevent the crystallization of this layer. However, its pristine state has relatively lower hole mobility ($<10^{-4}$ cm^2 V^{-1} s^{-1}) and conductivity (10^{-5} S cm^{-1}). Additives are necessary to improve these properties. In this case, lithium bistrifluoromethanesulfonimidate (LiTFSI) and 4-tert pyridine (tBP) had been applied together with Spiro-OMeTAD to get better performance. In dye-sensitized solar cells (DSSCs), LiTFSI functioned as the dopant to improve the conductivity and mobility by oxidizing the Spiro-OMeTAD. tBP is the charge recombination inhibitor, it can adsorb on the TiO2 to limit the contact between the hole transport layer and electron transport layer. When applied the combination of Spiro-OMeTAD, LiTFSI and tBP in PSCs, functions for tBP and LiTFSI had been reported as the same as that in DSSCs. However, due to the existence of perovskite capping layer, the electron transport layer/hole transport layer interface is limited, which means the function of tBP in PSCs may not be the same as DSSCs. Same with LiTFSI,

how it generates oxidized Spiro-OMeTAD in PSCs was unclear. More detailed discussion regarding the functions for tBP and LiTFSI in Spiro-OMeTAD will be shown in later chapters.

Though introducing tBP and LiTFSI improve the performance of PSCs with Spiro-OMeTAD, the stability of PSCs is also influenced. tBP is corrosive to perovskite materials and LiTFSI is hygroscopic and leads to water accumulation in the HTL. Both of these effects are detrimental to perovskite materials. As a result, several new small organic hole transport materials have been introduced, such as Pyrene derivatives, Thiophene derivatives, Triptycene derivatives, Triazine derivatives, and Triphenylamines derivatives. Some of them can display compatible efficiency with Spiro-OMeTAD.[72] Recently, EH44, a small organic molecule hole transport layer material had been introduced in PSCs. Without adding additive, the device can work effectively over 1000 hours with close to initial efficiency compared with Spiro-OMeTAD devices.[73]

2.4.2 Polymer Hole Transport Materials

Polymer hole transport materials have high mobility and conductivity. Compare with the organic hole transport materials, finding the proper organic solvent to dissolve polymers without dissolving perovskite materials is relatively difficult. That is why many polymer hole transport materials has alkyl side chain in order to get better solubility in conventionally used solvents. On the other hand, due to the larger size, the contact area between perovskite and polymer is limited, especially in the PSCs which has a meso-porous electrode.[42,74] However, the polymer hole transport materials normally have better stability than small organic materials, especially thermal stability. The band structure can be tuned not only by changing the units' functional group, but also by changing the degree of polymerization.

The most frequently applied polymer hole transport materials are Poly[bis(4-phenyl)(2,4,6-trimethylphenyl)amine] (PTAA) and Poly(3-hexylthiophene-2,5-diyl) (P3HT). Several world record efficiency PSCs had been fabricated with PTAA, the highest performance that PTAA-based PSCs is 22.1% efficiency.[46] On the other hand, both PTAA and P3HT need dopants such as LiTFSI and tBP to further improve the device performance. The stability for these polymer materials still need to be improved. As shown in Figure 2.9, the perovskite with polymer HTL PTAA, has lower stability than the perovskite with doped Spiro-OMeTAD.[75]

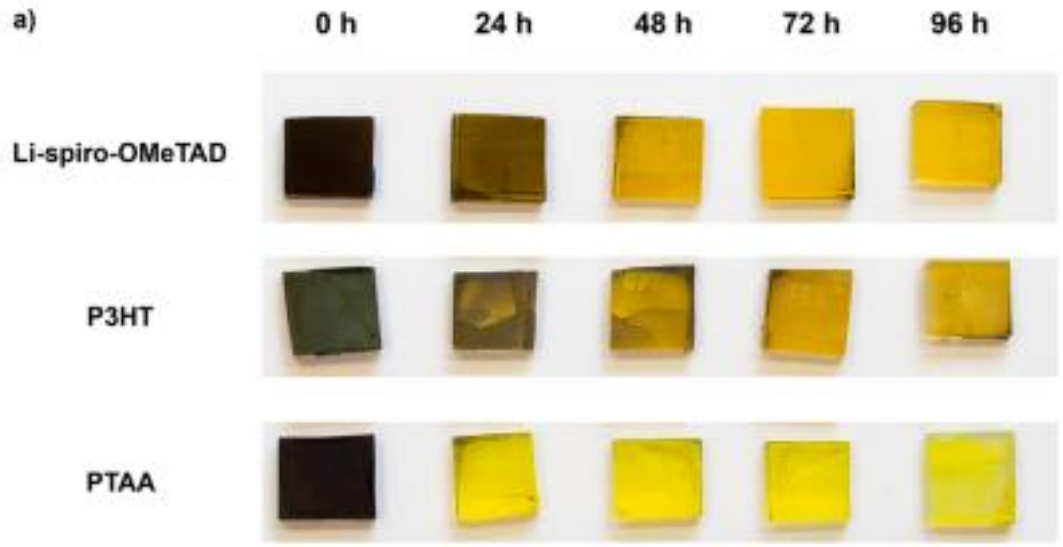

Figure 2.9 Stability of perovskite materials with different HTL[75]

2.4.3 Inorganic Hole Transport Materials

Inorganic hole transport materials are normally amorphous semiconductors because the crystallization of the HTL can reduce the contact at the perovskite/HTL interface. Some of the inorganic materials need sintering after deposition on substrate. Since the high temperature process can degrade perovskite, as a result, some of the inorganic hole transport materials can only be applied in the inverted configuration PSCs. The advantage for inorganic hole transport

materials in PSCs, is its higher stability than polymer/organic materials HTL. Majority of inorganic hole transport materials can be applied in PSCs without doping.[76]

NiO_x and CuSCN are the two inorganic hole transport materials applied in PSCs with high performance and stability. NiO_x, normally applied in the inverted configuration PSCs which need 600 ℃ annealing temperature. When combining with the ZnO as the electron transport layer in PSCs, the devices maintain its original efficiency for 60 days in light ambient condition.[68] The previous challenge for CuSCN was its reactivity with metal contacts. Professor Michael Grätzel group introduced the graphene barrier layer in between of the CuSCN and Au, which dramatically improved the stability on the CuSCN/Au interface. Together with the dynamic spin coating method for the hole transport layer, an over 20% efficiency had been achieved with >95% of initial efficiency at a maximum power point for 1000 hours at 60 ℃.[76]

Chapter 3. Advanced Characterization Tools

3.1. Focused Ion Beam (FIB)

Focused ion beam (FIB) is a technique which combines imaging with micro-machining functions. The ion beam is accelerated under the application of a bias and focused from 1-30 kV, it then scans the sample surface under high vacuum conditions. As a result, several species will be generated: the secondary electrons which can be applied for imaging, the escaped secondary ions and neutral atoms will be removed during micro-machining. Figure 3.1 displays the principle of FIB:

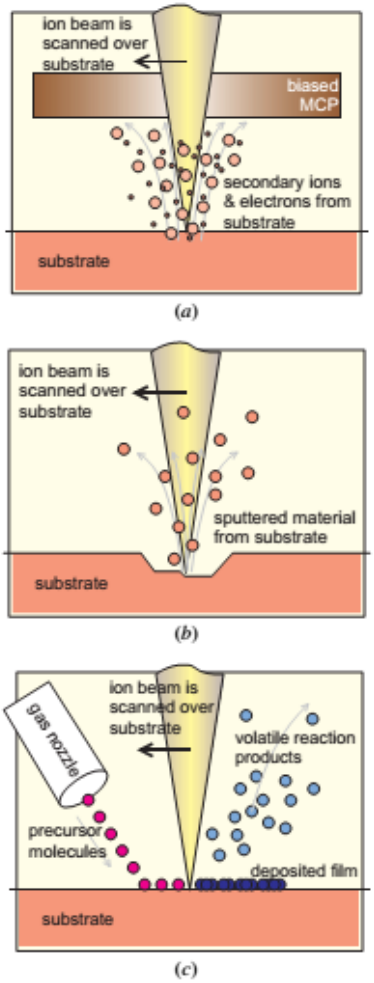

Figure 3.1 Principle of FIB (A) imaging, (B) milling and (C) deposition[77]

The core component in FIB is the ion beam column which is consists of an ion beam source and focusing lenses. There are three different types of the ion sources in FIB: (1) Liquid ion metal source; (2) Inductively coupled plasma source; and (3) Gas field ionization source. The liquid ion metal source is the most frequently applied one for its stability, long life time and good resolution. Due to the low vapor pressure in its liquid state, low boiling point (30℃) and low reactivity with the instrument, Ga^+ is the main source for this type of FIB. The molten Ga^+ flows to the tip of a Tungsten needle. With a strong electric field (~10V/nm), a Taylor cone is formed on the order of 5 nm because of the combined effects of surface tension and electrostatic force. Ga^+ is emitted when the metal loses electrons in the electric field and the ejected ions are focused by the electrostatic lenses. As shown in Figure 3.2:

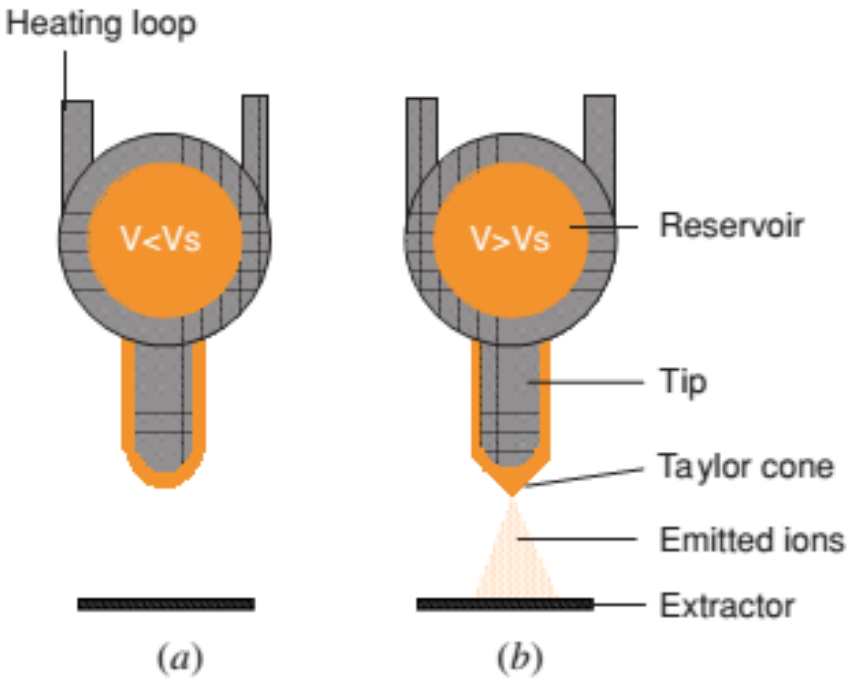

Figure 3.2 Schematic of the liquid metal ion source operation (LMIS): (A) tip applied voltage is below critical threshold voltage, Vs; (B) tip applied voltage exceeds extraction voltage Vs; the Taylor cone and ion emission appear.[78]

The imaging function for FIB is more like a scanning electron microscope (SEM), only difference is the source is changed from electrons (SEM) into ions (FIB). This change can supply more information about the materials: the ion-induced secondary electrons can show better contrast than the electron-induced secondary electrons. This is because the ion-induced secondary electrons rely on the crystal orientation, atomic composition, and surface morphology of the sample's surface.

As a destructive technique, materials can be milled away by FIB, so several micro-machining processes such as etching, lithography, patterning, and thinning is achievable. The sample can be thinned to less than 100 nm by FIB, which enables the observation of the full PSCs structure in transmission electron microscope (TEM) at high magnification. Figure 3.3 displays the entire processes for the preparing of the TEM PSCs specimen in FIB:

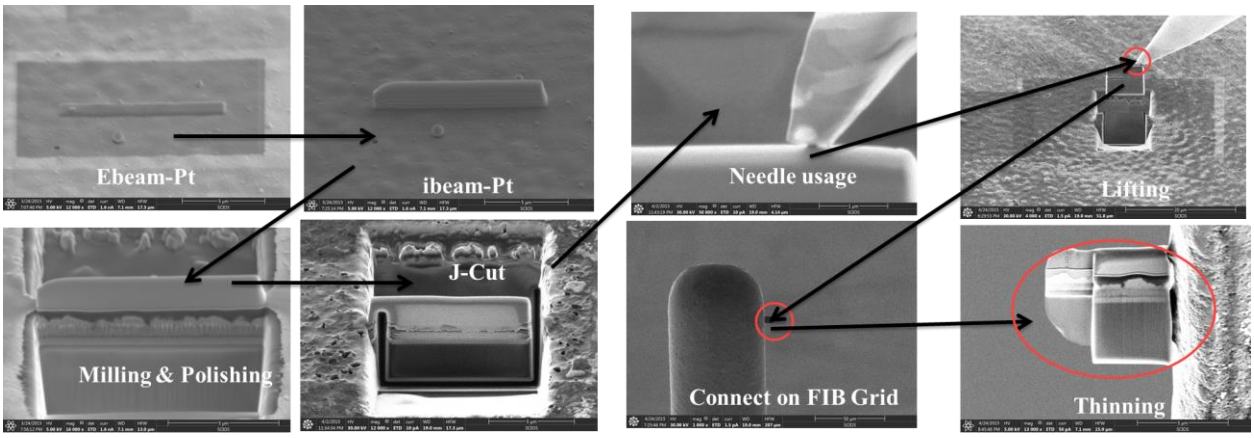

Figure 3.3 Entire processes for the preparing of the TEM PSCs specimen in FIB

3.2 Transmission Electron Microscopy (TEM)

Transmission Electron Microscopy (TEM) was applied in our project to characterize the materials and devices in nm or sub-nm scale. A beam of electrons is focused and transmitted through the specimen that is within 100 nm thickness. In some cases, particles which are thicker than 100 nm still can be observed in TEM by focusing on the edge of the materials. However, the

thickness of the samples in TEM is still one of the crucial factors to influence the quality of the image.[79]

The resolution of TEM is much higher than Scanning Electron Microscopy (SEM) and Optical Microscopy (OM). It is because the resolution of imaging techniques is determined by the wavenumber of imaging particles which can be evaluated by the Equation 3.1:

$$\lambda_e \approx \frac{h}{\sqrt{2m_0E\left(1+\frac{E}{2m_0c^2}\right)}} \qquad \text{(eq 3.1)}$$

Where, h is Planck's constant, E is the energy of the accelerated electron, c is the speed of light and m0 is the rest mass of an electron. The wavelength of OM is from 400-800 nm, according to Equation (1), in 200 kV TEM, the wavenumber which can be achieved is 0.00251 nm, to ensure the observation of samples at higher magnification. Due to the lower accelerating voltage, SEM has at least one magnitude lower resolution than TEM. The working mechanism for TEM is shown in Figure 3.4:

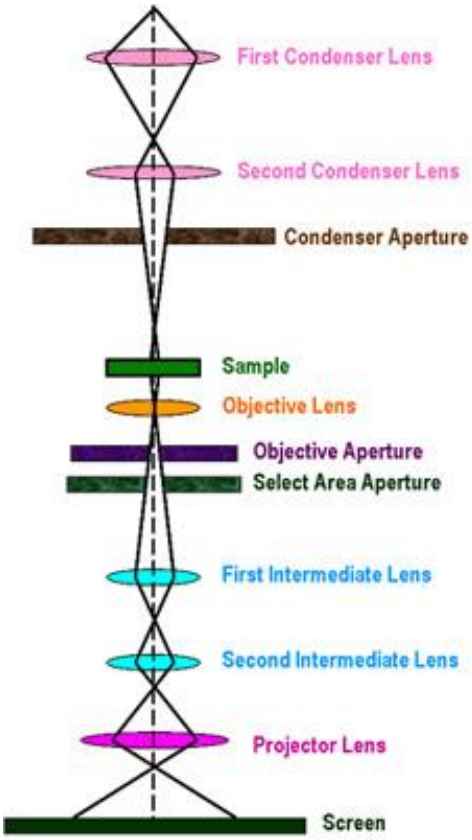

Figure 3.4 The schematic outline of a TEM[80]

The high resolution of TEM enables it not only to supply the morphological information of materials/devices, but also can show the structural information. Diffraction and crystal lattice can be observed in TEM in both image mode and diffraction mode. Moreover, electron energy loss spectroscopy and energy dispersive x-ray spectroscopy can be observed in TEM as well which can supply the compositional information about the specimen. [81]

In our study, TEM was applied for observing the full device structure of PSCs. The specimen was made by FIB as discussed in last session. In FIB, the specimen was lifted-up from a PSCs and thinned within 100 nm on an omni-probe grid for observing in TEM. Bright-field mode was applied in TEM for observing our device. The images will be shown and discussed in later chapters.

One special issue need to be stated that, the electron beam stability for halide perovskite materials in TEM is weak. Samples can be destroyed in seconds due to the instability of the organic components in perovskite materials. However, in PSCs specimen, this problem have not been observed yet, which can be attributed to the good thermal conductivity of HTL which may help with the improvement of the stability of perovskite materials in PSCs specimen for TEM.

Chapter 4. Chapter 4 Design and Fabrication Perovskite Solar Cells

In our research, two different configurations of PSCs have been designed and fabricated: one is mesoporous PSCs, and the other one is planar PSCs. Both of them are conventional structure with photoanode located on the conductive glass side.

4.1 PSCs with Meso-Porous Electrode

The meso-porous PSCs in our research, is based on TiO_2 mesoporous photoanode layer. This structure was inspired by the solid-state dye-sensitized solar cell.[71] It consists of compact TiO_2, mesoporous TiO_2, perovskite, hole transport layer and gold metal back contact. Figure 4.1 displays the morphology of the PSCs we fabricated:

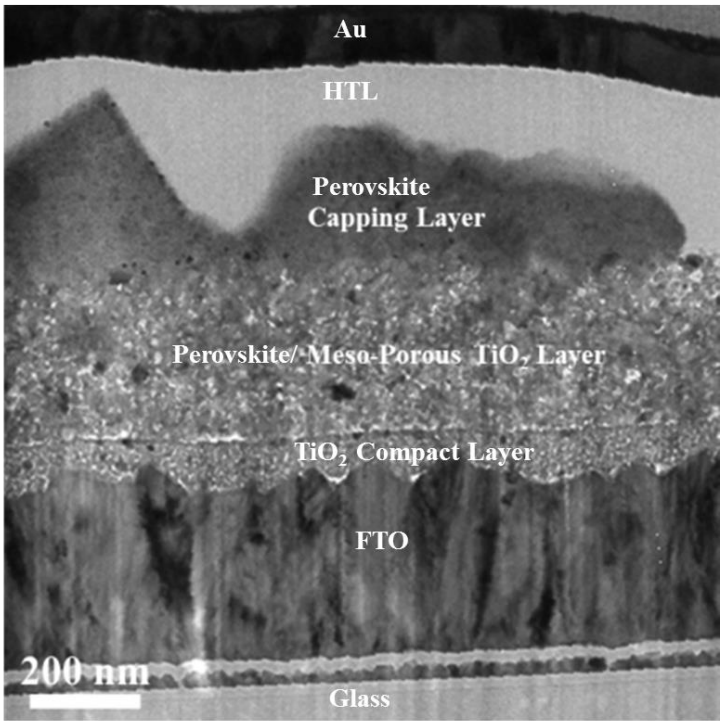

Figure 4.1 Morphology of the PSC (Bright Field-TEM Image) with meso-porous electrode fabricated in the Laboratory of Energy Storage and Conversion, UCSD [56]

The device fabrication recipe was based on reference[18] with some modifications. The preparation of TiO_2 compact layer was changed from spray pyrolysis to spin-coating method in order to adapt to our lab facility. As a result, this layer has a more flat morphology compare with the FTO substrate. This may influence the non-uniform series resistance due to the varying film thickness of the compact layer. On the other hand, the spin-coated compact layer (80-100 nm) has to be thicker than the spray-pyrolysis compact layer (~30 nm) to avoid the pin-hole-induced short circuit. As a result, it has higher series resistance than spray-pyrolysis compact layer. This 'compromised' method leads to a slightly lower efficiency in the final device.

The compact layer was annealed at 500 ℃ to form TiO_2 from its precursor. After that, $TiCl_4$ treatment was applied to further limit the short circuit current between hole transport layer and compact layer. The $TiCl_4$ treatment can help with the formation of some amorphous TiO_2 on the compact layer in order to reduce the pin-holes after annealing.

On top of the compact layer, the mesoporous TiO_2 layer was prepared by spin-coating. The commercial TiO_2 paste (Dyesol 18NR-T) is a mixture of 30 nm TiO_2 anatase nanocrystal, hydroxyethyl cellulose (EC) and terpineol. Terpineol functions as the solvent to disperse TiO_2 particles since it has high viscosity to ensure particle suspension and low boiling point (220 ℃) which is easy to be evaporated during the film annealing. The EC was applied as the pore-making agent, during the film annealing process. This polymer can be burned to generate pores. The pores were easy for the filtration of perovskite materials which guarantees a larger contact area between TiO_2 and perovskite.

The perovskite layer was prepared by sequential deposition method: PbI_2 was spin-coated on top of mesoporous TiO_2 layer, and then the film was immersed in a methyl ammonium iodide solution to form perovskite. We added an air-spray step after the perovskite formation: Dry air

was introduced to blow the film after the dipping step to avoid the 'coffee ring' effect. This measure greatly improves the reproductively of our devices. As shown in Figure 4.2.

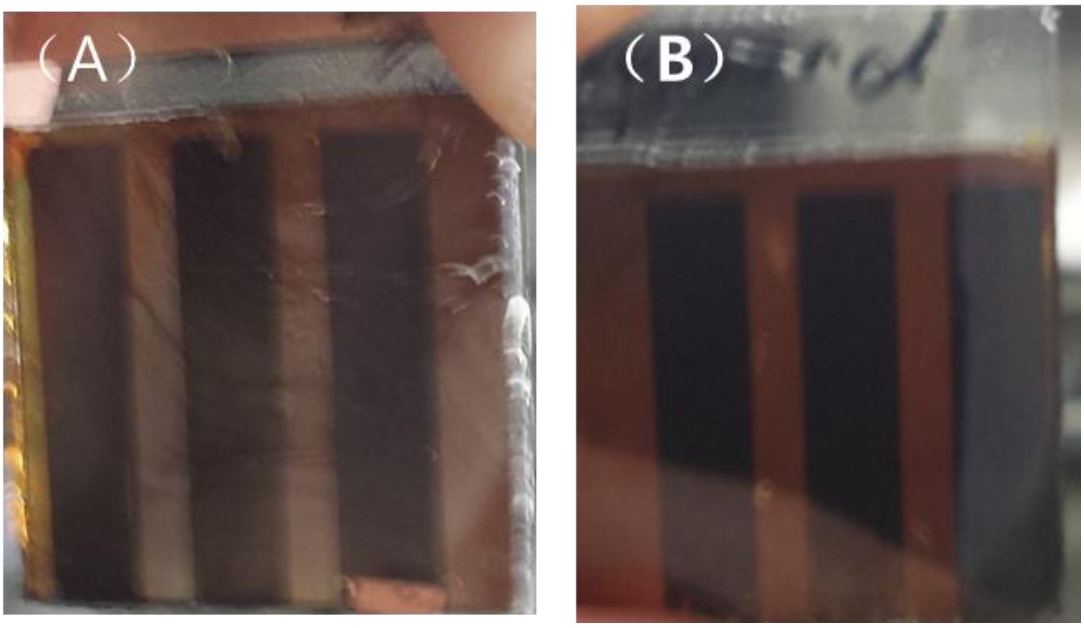

Figure 4.2 PSCs fabricated (A) without N_2 spray after perovskite sequential deposition; (B) with N_2 spray after perovskite sequential deposition

On the other hand, we also slowed down the spin-coating speed of PbI_2 (in the literature the speed is 6500 r.p.m. while in our recipe we use 3000 r.p.m.). It is because the lower r.p.m. shows better film coverage, and the better perovskite film coverage helped with the enhancement of the shunt resistance.

The hole transport layer was prepared by Spiro-OMeTAD, LiTFSI and tBP with spin-coating, and 80 nm of gold layer was prepared by e-beam evaporation. The reason that we applied e-beam evaporation instead of thermal evaporation in the reference, is because of the e-beam evaporation has lower temperature during deposition which has a less damaging effect on perovskite film.

The device performance of the PSC was shown in Figure 4.3 with over 12% efficiency.

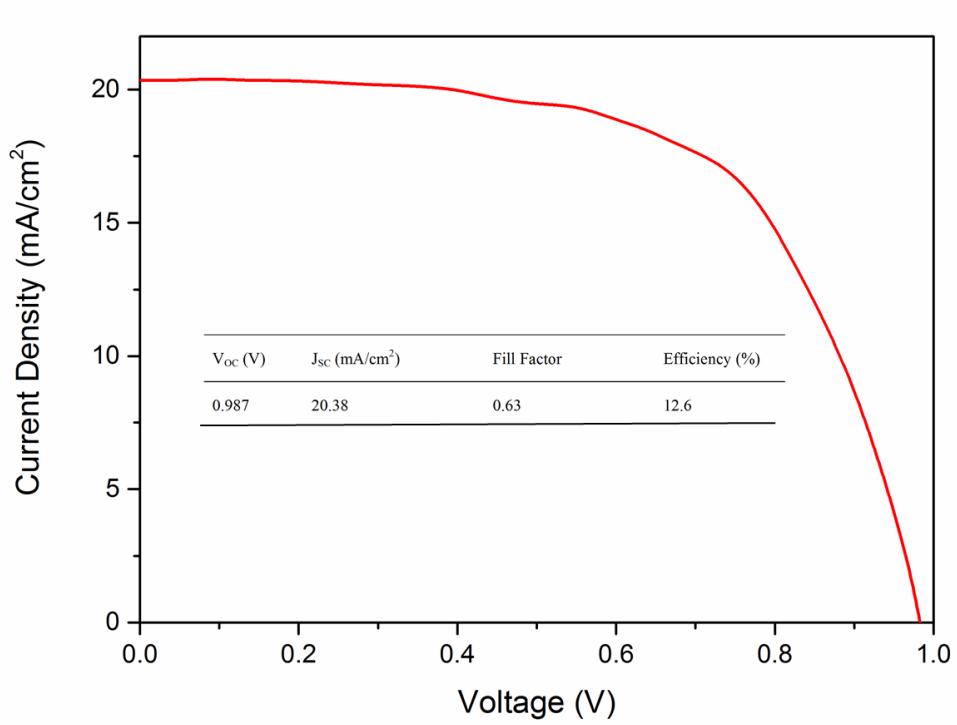

Figure 4.3 J-V curve of the PSC with meso-porous photoanode fabricated in the Laboratory of Energy Storage and Conversion, UCSD

4.2 Planar PSCs

The main reason for us to substitute the meso-porous PSCs to planar PSCs, is to lower the fabrication timeline with lower input energy during the device manufacturing: the mesoporous TiO_2 based PSCs need three annealing steps for the device fabrication (TiO_2 compact layer, $TiCl_4$ post treatment and meso-porous TiO_2) and the annealing temperature is 450 ℃ to 500 ℃. Regarding the planar PSCs, it just involves one annealing step and the SnO_x compact layer only need 180 ℃ annealing temperature. It includes compact SnO_x, perovskite, hole transport layer and gold back contact. The main recipe was based on reference[44] with some revisions. Figure 4.4 displayed the morphology of the PSCs we fabricated:

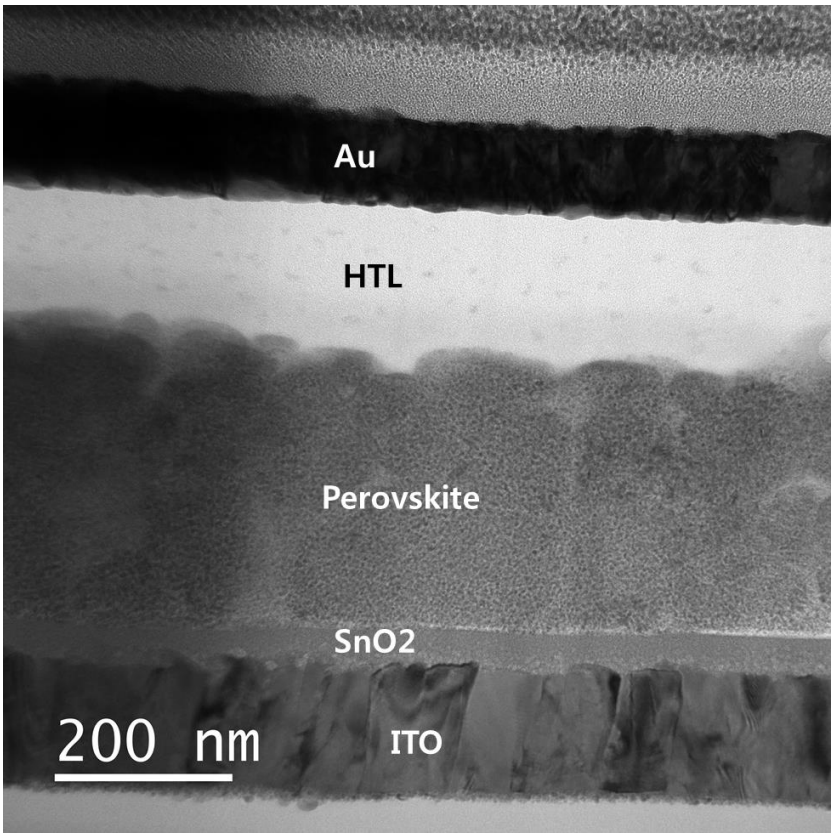

Figure 4.4 Morphology of the planar PSC (Bright Field-TEM Image) fabricated in the Laboratory of Energy Storage and Conversion, UCSD

The compact/electron transport layer was made with SnO_x by spin-coating method. SnO_x has higher electron conductivity and lower annealing temperature than TiO_2. On the other hand, for the low annealing temperature of SnO_x, ITO instead of FTO conduct glass can be applied as the substrate. Although ITO glass has lower sheet resistance than FTO glass, the TiO_2 device can only be prepared on FTO glass as ITO cannot withstand such high temperatures. On the contrary, SnO_x-based devices can use ITO glass for it only needs 180 ℃ annealing temperature. Moreover, the ITO has less roughness than FTO, which can ensure a uniform layer thickness of spin-coated SnO_x.

The perovskite layer was made with single-step method. The precursor solution contains equal molar ratios of PbI_2 and methyl ammonium iodide. Small amount of methyl amine was

added to the solution to reduce the defects in perovskite film.[44] The solvent is DMF according to the reference. 10 vol% of DMSO was added to the solution to slow down the crystallization of perovskite, which ensures better film coverage.

The hole transport layer also consists of Spiro-OMeTAD, tBP and LiTFSI. The LiTFSI was dissolved in acetonitrile which can dissolve perovskite. On the other hand, tBP is corrosive to perovskite. To reduce the corrosive effect from tBP and acetonitrile, dynamic spin-coating method was applied in our device: the hole transport layer solution was loaded while the film was spinning. This method can minimize the direct interaction between the perovskite film and the corrosive HTL components.

Same as the meso-porous PSCs, the Au layer was prepared by e-beam evaporation. To further reduce the heat during the deposition, a cooling stage was applied to control the temperature during the evaporation, which can further reduce the degradation due to the beam-induced thermal effect. The efficiency of the planar PSCs we fabricated was reached over 19% as shown in Figure 4.5:

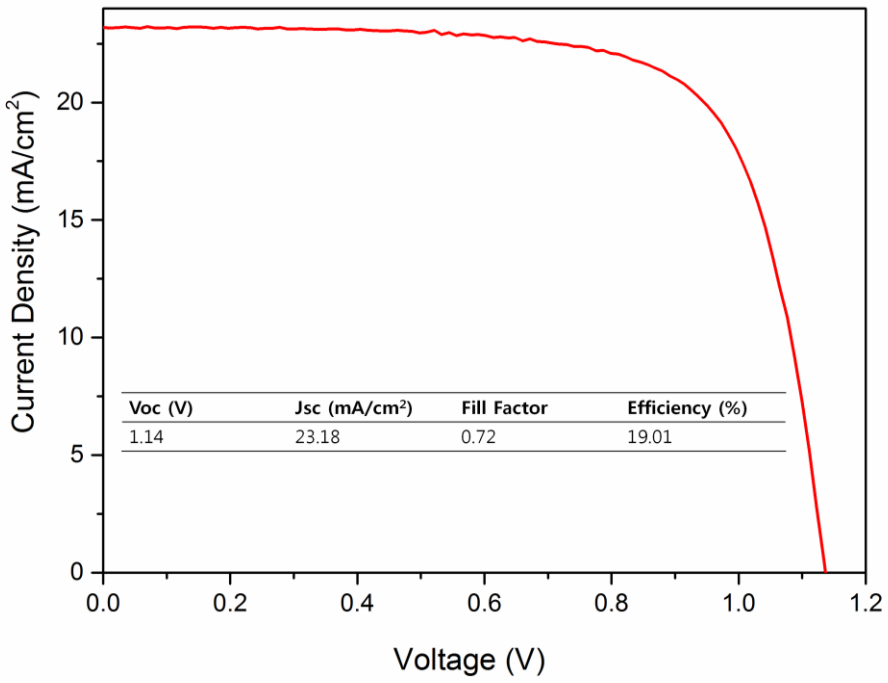

Figure 4.5 J-V curve of the planar structure PSC fabricated in the Laboratory of Energy Storage and Conversion, UCSD

Chapter 5. Spectrum-Dependent Spiro-OMeTAD Oxidization Mechanism in Perovskite Solar Cells

5.1. Introduction

Hybrid organic-inorganic perovskite solar cells (PSCs) have gained increasing attention as intriguing candidates for next-generation photovoltaic devices since 2009.[11] Recently, 20.1% power conversion efficiency has been achieved through intramolecular exchange reaction.[74] In addition to high efficiencies, PSCs are all-solid-state devices with low cost, a tunable band gap, and a scalable fabrication process, indicating its tremendous commercial prospects.[16–18,82–84] The key components of PSCs (which contains meso-porous TiO_2) include the blocking layer, metal oxide photoelectrode, perovskite layer, hole-transport material (HTM), and top electrode.[85] When photons excite the electrons from the valence band (VB) to the conduction band (CB) of the perovskite layer, excitons are generated. The excited electrons are injected into the CB of the metal oxide photoelectrode, and the holes are captured by the HTM in this charge separation process. The photogenerated electrons in the metal oxide are collected by a transparent conductive oxide and go to the external circuit. Electrons will recombine with holes at the top electrode to complete the circuit.[32] The photovoltage of the PSC is equal to the difference between the quasi-Fermi level of the metal oxide photoanode and the redox potential of the HTM.[25] The high hole collection efficiency at the perovskite/ HTM interface is one of the key factors needed to achieve better efficiency in PSCs.[86]

One of the major developments for PSCs in recent years is the substitution of the liquid electrolyte to the solid-state HTM 2,2′,7,7′-tetrakis(*N*,*N*-di-*p*-methoxyphenylamine)-9,9′-spirobifluorene (Spiro-OMeTAD). This substitution dramatically improves the stability and the efficiency of PSCs.[16,87] Unlike the liquid-based electrolyte, which can dissolve the perovskite

layer, the small organic molecule Spiro-OMeTAD, shown in Figure 5.1(A), is nonreactive to perovskite and is less volatile. The matched band gap with perovskite, amorphous nature, good conductivity with dopants, and high melting point for Spiro-OMeTAD make it one of the most adaptable HTMs in PSCs.[88–91] Recent research demonstrates that a >400 nm thickness of Spiro-OMeTAD HTM layer can guarantee a higher open-circuit voltage and hinder the charge recombination at the TiO_2/HTM interface. [92]

Surprisingly, the pristine uncharged form of Spiro-OMeTAD has a relatively low hole mobility and low conductivity before adding a *p*-dopant.[55] Additives play a key role in improving the hole conductivity of the Spiro-OMeTAD layer and ultimately increase the efficiency of PSCs. Bis(trifluoromethane)sulfonimide lithium salt (LiTFSI) has been reported as a *p*-dopant to enhance the conductivity and hole mobility of the Spiro-OMeTAD.[54,90,93–96] The function of LiTFSI in PSCs is quite similar to that in solid-state dye-sensitized solar cells (ss-DSSCs). Some of the lithium ions can intercalate into TiO_2 to downshift its conduction band, resulting in a higher photocurrent.[97–99] The rest of the lithium ions can react with oxygen and Spiro-OMeTAD to facilitate the generation of oxidized Spiro-OMeTAD. While the large anion $TFSI^-$, as shown in Figure 5.1(B), can stabilize the oxidized Spiro-OMeTAD as the counter-ion. [54,93,94,100–102]

There are two different proposed mechanisms in the literature on the generation of oxidized Spiro-OMeTAD with the assistance of LiTFSI in DSSCs. Ute B. Cappel et al. proposed a three-step mechanism where sensitizers are excited by photons and then the excited electrons are captured by oxygen. The oxidized Spiro-OMeTAD is created by regeneration of oxidized sensitizer. In the reactions, LiTFSI functions either as a catalyst or a stabilizer of the oxidized Spiro-OMeTAD.[54] The mechanism is written as:

$$Dye + hv \longrightarrow Dye^* \longrightarrow Dye^+ + e^-(TiO_2) \quad (1)$$

$$e^-(TiO_2) + O_2 \longrightarrow O_2^{\cdot -} \quad (2)$$

$$Dye^+ + Spiro \longrightarrow Dye + Spiro^+ \quad (3)$$

Later, Antonio Abate et al. proposed a two-step mechanism: first, equilibrium between Spiro-OMeTAD with oxygen and oxidized Spiro-OMeTAD (Spiro-OMeTAD$^{\cdot +}O_2^{\cdot -}$) exists; the equilibrium is moved forward by adding LiTFSI, because the superoxide radical O_2^- reacts with Li^+ to form Li_2O and Li_2O_2, and finally Spiro-OMeTAD$^{\cdot +}$TFSI$^-$ is generated.[100] The mechanism is written as:

$$\text{Spiro-OMeTAD} + O_2 \longleftrightarrow \text{Spiro-OMeTAD}^{\cdot +}O_2^{\cdot -} \quad (4)$$

$$\text{Spiro-OMeTAD}^{\cdot +}O_2^{\cdot -} + \text{LiTFSI} \longrightarrow \text{Spiro-OMeTAD}^{\cdot +}\text{TFSI}^- + Li_xO_y \quad (5)$$

The major difference between these two mechanisms is whether photons and sensitizers participate in the reactions. In the three-step mechanism, photons trigger the following reactions while the oxidized Spiro-OMeTAD is produced from the regeneration of sensitizers. In the two-step mechanism, neither photons nor sensitizers facilitated the formation of oxidized Spiro-OMeTAD. Moreover, initial illuminating treatment, which means to illuminate a solar cell for a while before testing its efficiency, also plays a key role on enhancing solar cell performance. It can be attributed to the Li^+ migration and Spiro-OMeTAD oxidization,[94] which supports the photons participating in the generation of the oxidized Spiro-OMeTAD.

Due to the similar device structure between DSSC and PSCs, the above mechanisms can be adapted to PSCs. Only few studies are focusing on the function of LiTFSI in the PSCs up to now. Exploring the relations between these mechanisms and PSCs can help understanding the function of photons, LiTFSI, and perovskite on the formation of oxidized Spiro-OMeTAD. It would allow us to find rational ways to further improve the efficiency of PSCs.

Herein, we report a systematic study of the origination of oxidized Spiro-OMeTAD in PSCs. With the combination of UV-Vis, a solar simulator equipped with longpass filters, four-point probe conductivity measurement and electrochemical impedance spectroscopy, a spectrum-dependent mechanism is proposed based on the wide absorption range of perovskite. This mechanism that reconciles the difference in previously proposed mechanisms is applicable for various visible spectrum ranges to increase the amount of oxidized Spiro-OMeTAD and finally, improve the efficiency of PSCs.

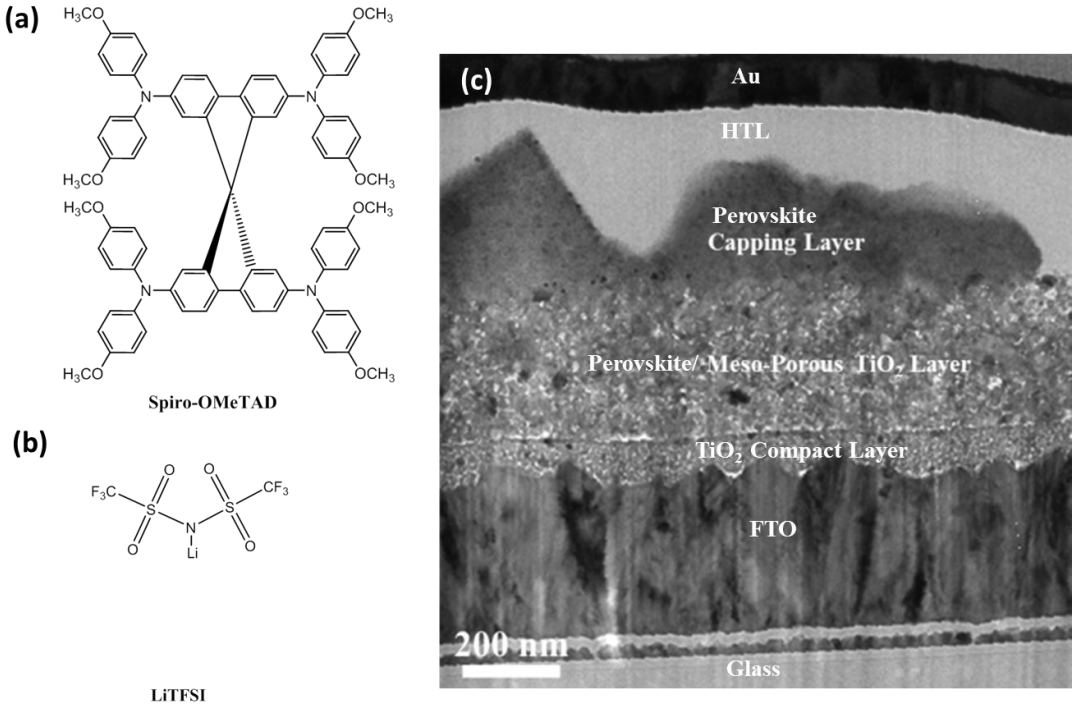

Figure 5.1 Molecular Structures of (A) Spiro-OMeTAD and (B) LiTFSI; (C) BF-TEM image from cross section view of full Perovskite Solar Cell

5.2 Experimental Methods

5.2.1 Reagents and Materials

All materials, unless stated otherwise, were purchased from Sigma Aldrich and used as received. Spiro-OMeTAD was purchased from Merck KGaA.

5.2.2 Synthesis of CH_3NH_3I

CH_3NH_3I was synthesized according to the reported procedure.[103] 14 ml Methylamine (40% in methanol, TCI) and 15 ml hydroiodic acid were mixed at 0℃ and stirred for an hour. The solution was evaporated at 90℃ for an hour to obtain the deep-brown primary product. The product was re-dissolved in ethanol at 70℃, precipitated and washed with diethyl ether several times until the product turned to white color. Finally, the product was dried at 60℃ in a vacuum oven for 24 h.

5.2.3 Device Fabrication

Perovskite solar cells were fabricated using the sequential deposition method.[18] FTO glasses (Pilkington, TEC-15) were cleaned by an ultrasonic bath with detergent water, alkaline ethanol solution, and deionized water, sequentially; each cleaning step lasted for 15 min. Then, the oxygen plasma cleaning step was applied for 10 min to remove the last traces of organic residues on the slides.

The TiO_2 blocking layer (BL) was spin-coated on the FTO substrates at 800 r.p.m. for one minute using 0.24 M titanium isopropoxide in 5 ml ethanol solution. The films were annealed at 500℃ for 30 min. After cooling down to room temperature, the films were immersed in 0.03 M aqueous $TiCl_4$ solution at 70℃ for 40 min and then gradually heated at 500℃ for 40 min after washing with deionized water. Commercial TiO_2 paste (Dyesol 18NRT, Dyesol) diluted in ethanol (2:7, weight ratio) was spin-coated on the films at 5,000 r.p.m for 30 sec and the film was annealed at 450℃ for 40 min to form the mesoporous TiO_2 layer.

PbI_2 solution (1 M) was prepared by 462 mg PbI_2 dissolved in 1 mL *N*,*N*-dimethylformamide (DMF) stirring at 80℃. The solution was spin coated on the films at 5000

r.p.m. for 90 sec. After spinning, the films were dried at 80℃ for 30 min and dipped in 2-propanol for 2 sec. Then the pre-wetted films were dipped in a solution of CH_3NH_3I in 2-propanol (10 mg ml^{-1}) for 2 min and dried at 80℃ for 30 min.

The 2,2',7,7'-teterakis(*N*,*N*-di-*p*-methoxyphenylamine)-9,9-spirobifluorene (Spiro-OMeTAD) solution was prepared by 100 mg of Spiro-OMeTAD, 28.8 μl 4-*tert*-butyl pyridine (tBP) and 17.7 μl lithium bis(trifluoromethanesulfonyl)imide (LiTFSI) solution (520 mg LiTFSI in 1 ml acetonitrile) in 1 ml of chlorobenzene. The solution was spin-coated on the $CH_3NH_3PbI_3$ layers at 3,000 r.p.m. for 1 min. Finally, 80 nm of gold was e-beam evaporated on the Spiro-OMeTAD-coated film.

The full perovskite solar cell structure is displayed in Figure 5.1(C). The image was taken by the bright field transmission electron microscope (BF-TEM). The sample was thinned within 100 nm by focusing ion beam before taking the TEM image.

Devices for measuring the resistance of the hole conductor were fabricated as follows with the Spiro-OMeTAD solution identical to that used for the PSC fabrication, the solution spin-coated on glass substrates with/without perovskite $CH_3NH_3PbI_3$ layer (the perovskite $CH_3NH_3PbI_3$ layer was prepared as the same procedure as the PSC) at 3,000 r.p.m. for 1 min, the Spiro-OMeTAD coated films covered with a 100 μm width spacer, and finally 80 nm of gold e-beam evaporated on the sample.

5.2.4 Device Characterization

Photocurrent density and voltage (J-V) were measured with a solar simulator with a 150 W xenon lamp (Solar Light SL07265, equipped with an AM1.5G filter, calibrated with a standard Si solar cell to simulate AM1.5 illumination (100 mW cm^{-2})) and a Keithley 2400 source meter. Before the J-V test, the solar simulator was marked with a 450 nm longpass filter

to illuminate the perovskite solar cell for one hour and test its efficiency at 0 min, 10 min, 30 min, and 1 h.

Electrochemical Impedance Spectra (EIS) were conducted using a Solartron 1287 electrochemical interface coupled with a Solartron 1455A frequency response analyzer. A 10 mV perturbation was applied, and the frequency was from 1 MHz to 1 Hz. The solar cell was illuminated by the solar simulator which was integrated with the 450 nm longpass filter for 1 h, and the solar cell was tested by the EIS at 0 min, 10 min, 30 min, and 1 h, respectively. Final results for EIS were fit with Z-View (The equivalent circuit of EIS fitting is shown in Figure 5.2. The fitting results are shown in Table 5.1).

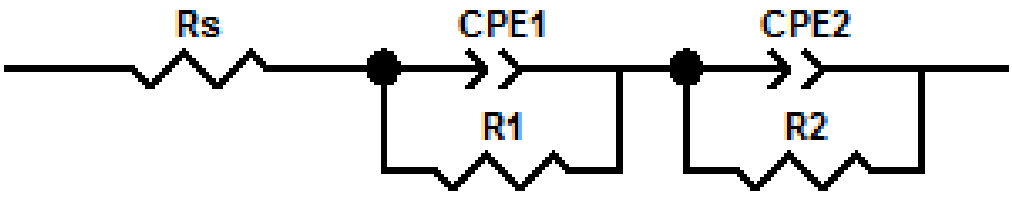

Figure 5.2. EIS equivalent circuit for the PSCs. R_s represents the series resistance, while R_1 and R_2 correspond to the charge transfer resistance at the Au/HTL and HTL/TiO_2 interfaces, respectively.

Table 5.1 EIS fitting results of the perovskite solar cell with > 450 nm illumination from 0 min to 60 min

	Rs (ohm)	R_1 (ohm)	R_2 (ohm)
0 min	34.81	13.69	312.1
10 min	33.87	7.01	357.2
30 min	34.56	4.59	363.6
60 min	34.29	4.42	365.1

Resistance of the hole conductor was tested by four-point probe (Jandel Four-Point Probe with RM3000 Test Unit) measurement with the devices mentioned before in dark condition. The curves on the devices, which were created by the 100 μm spacer, were set between the second and third probe during the test. Before testing, the devices were illuminated on solar simulator with full light, 380 nm longpass filter and 450 nm longpass filter for 0 min, 10 min, 20 min, 30 min, 40 min and 1 h, respectively.

5.2.5 UV-Vis Spectroscopy

UV−Vis spectra were carried out in an absorption mode on a Lambda 1050 UV−Vis spectrometer. Measurements of the solutions were taken in a 10 mm quartz cuvette placed in a cuvette holder was integrated within the setup. The concentration of Spiro-OMeTAD for the UV-Vis test was 8 μM in chlorobenzene.

5.3 Results and Discussion

The first aim of this study is to understand the function of photons on the generation of oxidized Spiro-OMeTAD. According to the literature, the major UV-Vis peak for Spiro-OMeTAD is a sharp peak at 395 nm, while oxidized Spiro-OMeTAD is a sharp peak at 400 nm and an additional broad peak around 500 nm.[104] However, as the signal of Spiro-OMeTAD around 395 nm often shields the oxidized Spiro-OMeTAD 400 nm peak, the broad peak around 500 nm is usually considered as the indicator for the generation of oxidized Spiro-OMeTAD.[100,101]

Figure 5.3(A) and (B) show the influence of illumination time on Spiro-OMeTAD with LiTFSI in ambient condition at AM1.5 illumination (100 mW cm^{-2}). The increasing absorption from 600-800 nm also implies the generation of oxidized Spiro-OMeTAD as well, for the broad peak can extend to 800 nm.[101] This illumination time-dependent signal illustrates that photons are participating in the generation of the oxidized Spiro-OMeTAD in ambient condition.

Figure 5.3(C) and (D) show the effect of the LiTFSI concentration on the generation of oxidized Spiro-OMeTAD with the same illumination time; the samples are exposed to AM1.5 illumination (100 mW cm^{-2}) for 1 h. According to Figure 5.3(D), even without adding lithium salt, after 1 h of illumination the broad 500 nm peak appears which means that LiTFSI is unnecessary for the generation of oxidized Spiro-OMeTAD. With only O_2 and light, Spiro-OMeTAD oxidation can occur. However, with an increasing amount of LiTFSI, the amount of oxidized Spiro-OMeTAD also increased. This phenomenon indicates that although LiTFSI does not function in the generation of oxidized Spiro-OMeTAD, it can facilitate the Spiro-OMeTAD oxidation reaction to move forward. Therefore, LiTFSI acts as a 'secondary reactant' to move forward the primary Spiro-OMeTAD oxidation reaction.

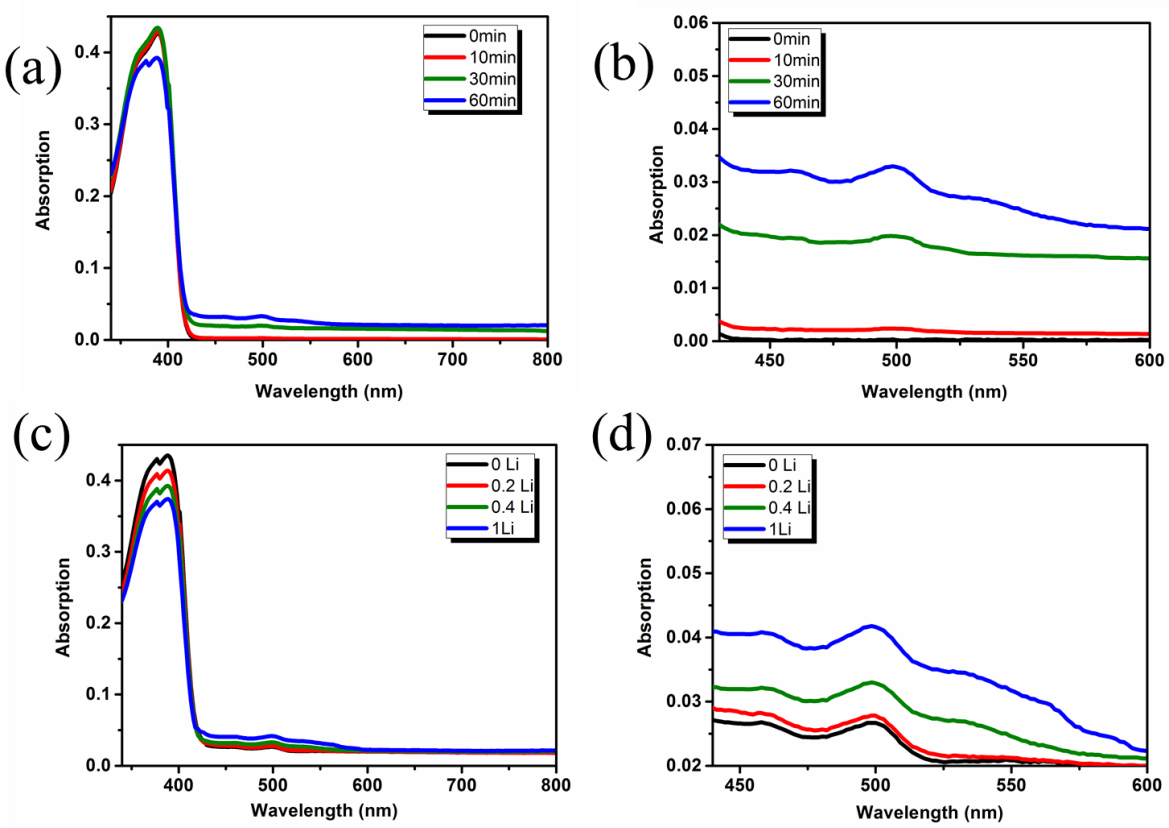

Figure 5.3 UV-Vis spectra of Spiro-OMeTAD: different illumination time with 0.4 LiTFSI/Spiro-OMeTAD molar ratio at: (A) full spectral range; (B) 450-600 nm range; and 1 h illumination with different LiTFSI amount (0 to 1 LiTFSI/Spiro-OMeTAD molar ratio) at: (C) full spectral range; (D) 450-600 nm range

We then investigated the effect of the incident light wavelength on the oxidation reaction. Two different types of longpass filters are separately equipped to the solar simulator to detect whether the reactions are spectrum-dependent. The function of the longpass filter is to control the spectral range. It only allows the photons which have longer wavelength to pass through and illuminate on sample. For instance, the 380 nm longpass filter only allows the light with wavelength longer than 380 nm to pass.

The Spiro-OMeTAD samples, as previously tested, are kept in ambient dark condition for 30 min as the reference sample. According to Figure 5.4, no peak appears around 500 nm after 30 min when the sample was kept in ambient dark condition. This supports our conclusion that Spiro-OMeTAD oxidization is optically activated.

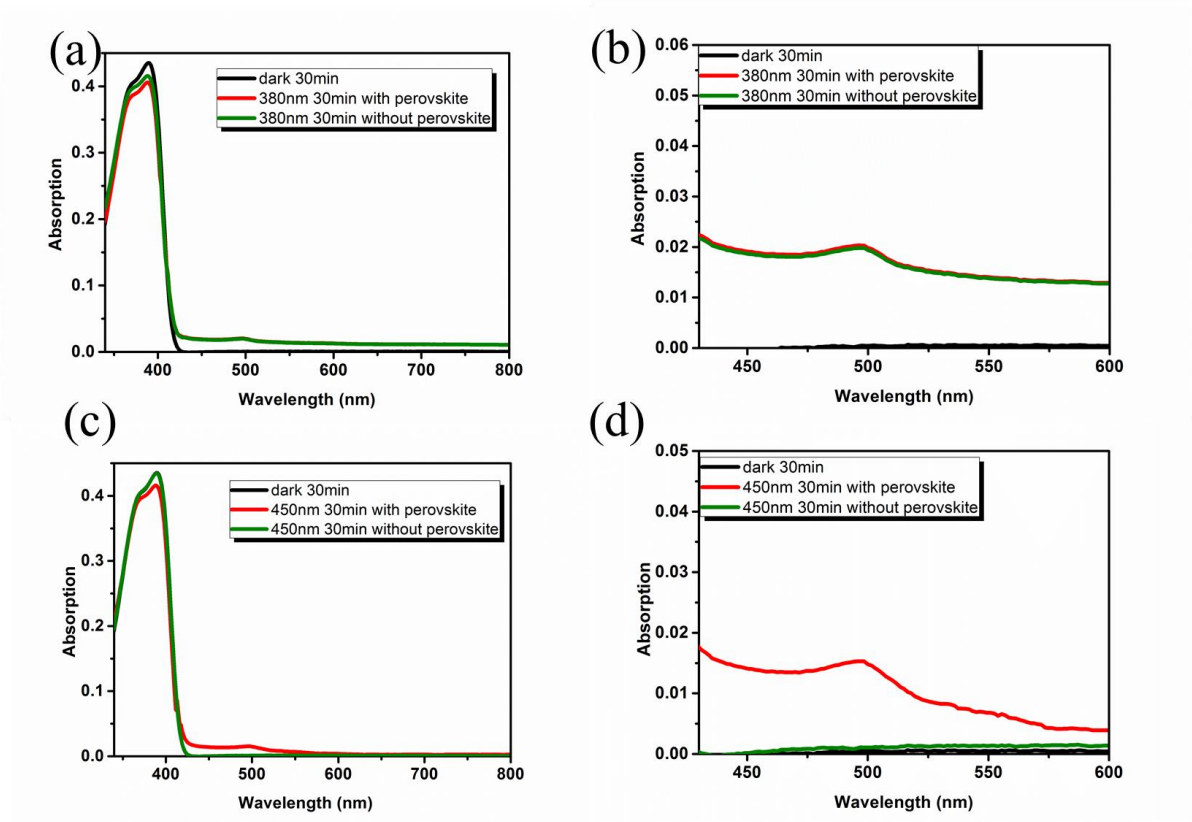

Figure 5.4 UV-Vis spectra of Spiro-OMeTAD/LiTFSI (0.4 molar ratio) with/without perovskite after 30 min illumination with 380 nm longpass filter at: (A) full spectral (b) 450 nm-600 nm; and 450 nm longpass filter at (C) full spectral (D) 450 -600 nm

As mentioned previously, the major absorption peak for Spiro-OMeTAD in UV-Vis spectrum is 395 nm, so it is possible that lower-wavelength light can trigger the following Spiro-OMeTAD oxidization. In contrast, at wavelength longer than 450 nm, no absorption peak

appears. The photons in this range (>450 nm) may not be energetic enough to overcome the activation energy for the oxidization reaction. Meanwhile, perovskite has a wide absorption range; the absorption spectrum for $CH_3NH_3PbI_3$ extends to 800 nm while $CH_3NH_3Sn_{0.5}Pb_{0.5}I_3$ extends up to 1050 nm.[105] The wide absorption range indicates that in a long wavelength range (> 450 nm), it is possible that Spiro-OMeTAD oxidization reaction can proceed with the assistance of perovskite. Based on these assumptions, the solar simulator was equipped with 380 nm and 450 nm longpass filters to investigate the spectrum-dependent roles of perovskite in the Spiro-OMeTAD oxidization.

As shown in Figure 5.4(A) and 5.4(B), when the wavelength is longer than 380 nm, after 30 min of illumination treatment, the oxidized Spiro-OMeTAD peak will appear regardless of the presence of a perovskite layer. This shows that in this spectrum range, it is unnecessary for perovskite to participate in the Spiro-OMeTAD oxidization. When using the 450 nm longpass filter to illuminate the sample for 30 min, as shown in Figure 5.4(C) and 5.4(D), the oxidized Spiro-OMeTAD peak (around 500 nm) only appears in the sample which has perovskite. This result proves that in long wavelength range, the perovskite sensitizer participates in oxidization. As a result, two mechanisms exist in the formation of the oxidized Spiro-OMeTAD: In 380 to 450 nm spectral range, perovskite is unnecessary for Spiro-OMeTAD oxidization. While in >450 nm spectral range, Spiro-OMeTAD needs the assistance of the perovskite to be oxidized.

We used liquid samples for UV-Vis because UV-Vis cannot rule out the spectral disturbance of the perovskite layer in the solid state. To further prove the spectrum-dependent hypothesis in solid state Spiro-OMeTAD, the conductivity of the hole transport layer was characterized by four-point probe measurement.

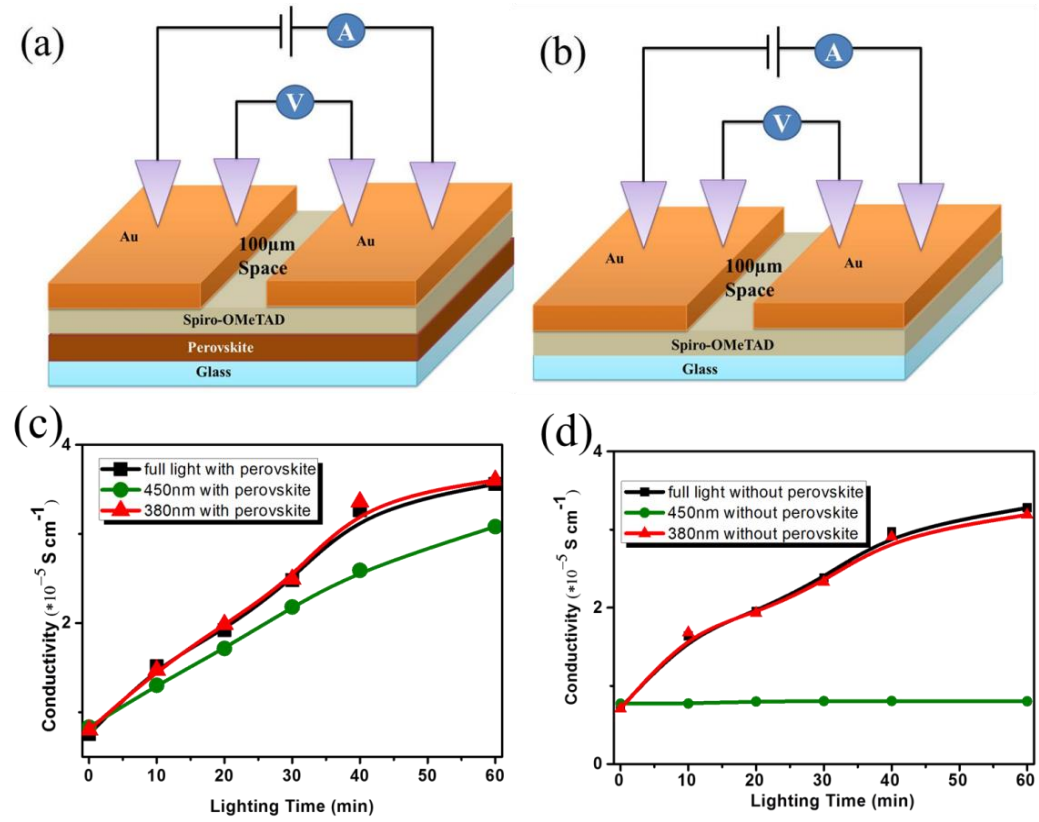

Figure 5.5 Effective conductivity of the HTL (0.4 LiTFSI/Spiro-OMeTAD molar ratio) at various illumination times/spectral ranges measured by a four-point probe, testing device structure (A) with/(B) without a perovskite layer, effective hole conductivity (C) with/(D) without a perovskite layer

The device structure for the four-point probe measurements is shown in Figure 5.5(A) and (B). A 100 μm space is set between the second and third probes on each device to ensure the measurement of the hole transport layer conductivity. After the devices were illuminated by the solar simulator equipped with longpass filters for a specific period of time (from 0 min to 60 min), the conductivity was tested by four-point probe in dark condition in case less current

flowed through the perovskite layer. If the Spiro-OMeTAD oxidization occurs, the total amount of ions in the hole transport increases, enhancing the conductivity of the devices.

As shown in Figure 5.5(C), when the perovskite layer exists, the conductivity of all devices increased. The only difference in Figure 5.5(C) is that the device which was illuminated with the 450 nm longpass filter light has a conductivity that improves slower than the other two. This can be attributed to the low illumination intensity compared to the full spectral illumination. It indicates that with the assistance of a perovskite layer, at a long wavelength range (>450 nm), Spiro-OMeTAD oxidization occurs. However, in the perovskite-free device, according to Figure 5.5(D), even after 60 min of illumination, the 450 nm longpass illumination treatment does not change the device conductivity, which means little or no oxidized Spiro-OMeTAD is generated. The results of the conductivity test are in excellent agreement with the UV-Vis characterization: oxidized Spiro-OMeTAD is generated in the short wavelength range without perovskite, while in the long wavelength range, the generation of oxidized Spiro-OMeTAD is only possible with the assistance of the perovskite.

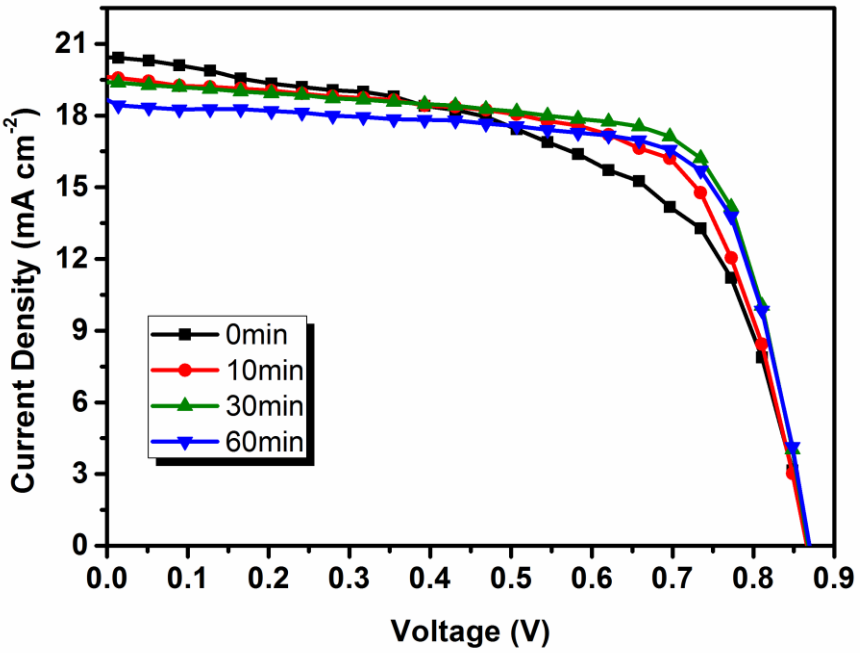

Figure 5.6 J-V curves of the perovskite solar cells after >450 nm illumination initial treatment

Table 5.2. Cell parameters of the perovskite solar cells after an initial treatment of > 450 nm illumination

	V_{OC} (V)	J_{SC} (mA/cm^2)	Fill Factor	Efficiency (%)
0min	0.867	20.52	0.56	10.0
10min	0.870	19.68	0.66	11.3
30min	0.862	19.51	0.71	11.9
60min	0.860	18.72	0.71	11.5

In order to understand the effect of long wavelength illumination on device performance, we fabricated perovskite solar cells and tested the efficiency after >450 nm illumination initial treatment. As we stated before, in long-wavelength range, photons cannot trigger the Spiro-OMeTAD oxidization without perovskite. If perovskite did not participate in the reaction, no J-V curve change should be observed as the exposure time increases. As shown in Figure 5.6 and Table 5.2 however, as the illumination time gets longer, the short circuit current density, fill factor, and cell efficiency improve within 30 min from 10% to 11.9%. This can be attributed to the increasing amount of oxidized Spiro-OMeTAD. The oxidized Spiro-OMeTAD is generated after the long wavelength illumination treatment, and with the assistance of perovskite, more photo-induced electrons can be captured by oxidized Spiro-OMeTAD. As a result, the charge recombination of the solar cell rises at the Spiro-OMeTAD/TiO_2 interface. At the same time, the oxidized Spiro-OMeTAD improves the conductivity and mobility of the hole transport layer. The balance of the negative effect (charge recombination) and positive effect (conductivity improvement) increases the solar cell efficiency in the first 30 min.

After 30 minutes of long wavelength initial illumination treatment, the efficiency of the solar cell slightly decreases. This phenomenon might be more attributed to charge recombination caused by the higher concentration of oxidized Spiro-OMeTAD. The short-term stability issues such as the migration/accumulation of LiTFSI in the hole transport layer,[93] the moisture sensitivity, or the degradation of the perovskite layer[106] may cause the slightly decrease of the efficiency as well. In general, the oxidized Spiro-OMeTAD will enhance the efficiency in a short term (< 30 minutes), with a minor decrease in the efficiency afterwards. As shown in Figure 5.7, all the PSCs we fabricated are displaying the same behavior after >450 nm illumination initial treatment.

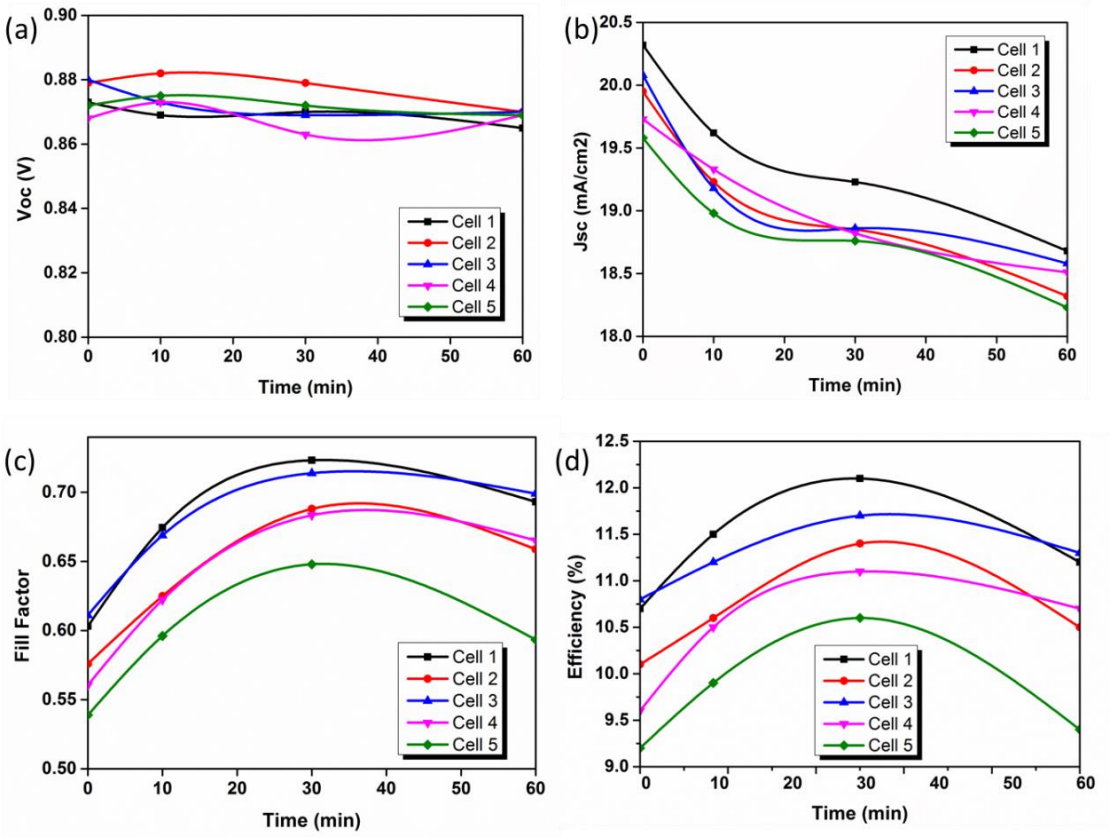

Figure 5.7 Solar cell parameters of the perovskite solar cells after >450 nm illumination initial treatment

We also tested the PSCs after full light illumination initial treatment (Figure 5.8 and Table 5.3). Quite similar behavior compared to the >450 nm illumination initial treatment was observed through the solar cell parameters. The only difference is that the full light treatment cell reaches the maximum fill factor and the efficiency within 10 minutes instead of 30 minutes. This phenomena can be attributed to the oxidized Spiro-OMeTAD can generate faster with the full light illumination treatment than with the >450 nm illumination treatment.

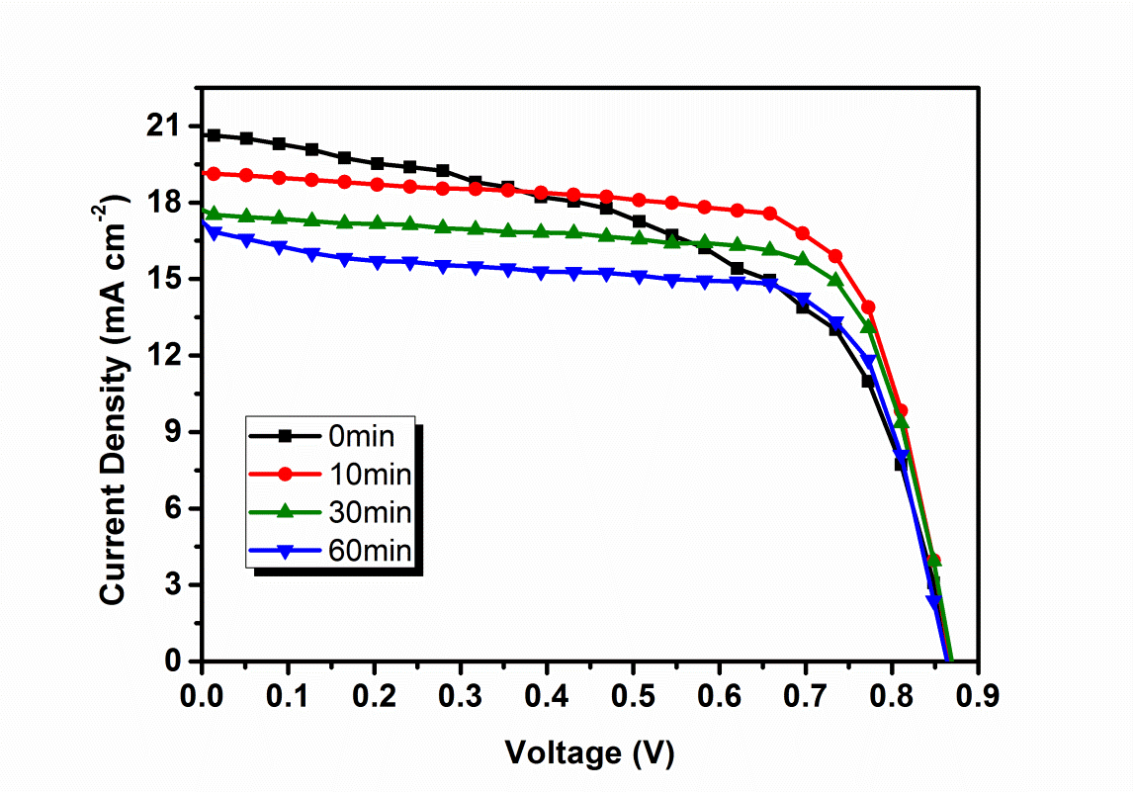

Figure 5.8 J-V curves of the perovskite solar cells after >450 nm illumination initial treatment

Table 5.3 Cell parameters of the perovskite solar cells after an initial treatment of full light illumination

	V_{OC} (V)	J_{SC} (mA/cm^2)	Fill Factor	Efficiency (%)
0min	0.870	20.63	0.54	9.75
10min	0.865	19.27	0.70	11.7
30min	0.868	17.7	0.71	11.1
60min	0.864	17.2	0.66	9.87

To further investigate the long wavelength light illumination influence on the PSC, electrochemical impedance spectroscopy (EIS) is applied to characterize the interfacial charge transfer and charge recombination of PSCs at various long wavelength illumination times.

The equivalent circuit of this model for PSC (Figure 5.2) has been reported.[107,108] R_s represents the series resistance, while R_1 and R_2 correspond to the charge transfer resistance at the Au/Spiro-OMeTAD and Spiro-OMeTAD/TiO_2 interfaces respectively. According to the Nyquist plot of Figure 5.9(A) and the fitting results (Table 5.1), in the first semi-cycle, which corresponds to R_1, R_1 will decrease with increasing illumination time. It is attributed to the increasing amount of the oxidized Spiro-OMeTAD that reduces the resistance at the Au/Spiro-OMeTAD interface. By reducing R_1, the oxidized Spiro-OMeTAD improves on cell performance. Electrons are easier to transfer from the Au to the hole transport layer with more oxidized Spiro-OMeTAD.

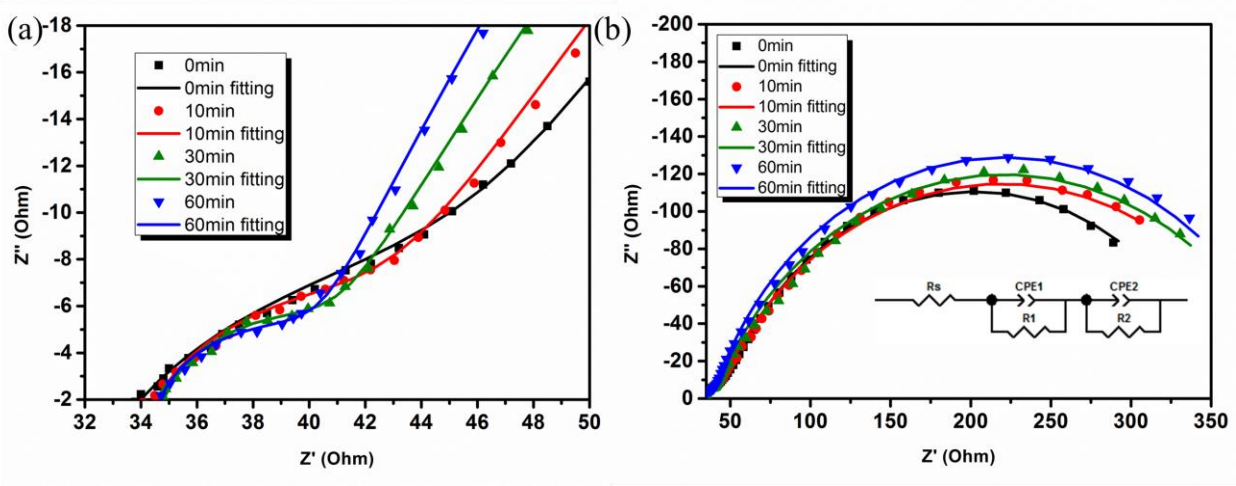

Figure 5.9 Nyquist plots of the perovskite solar cell with > 450 nm illumination from 0 min to 60 min at a (A) high frequency range and (B) full frequency range. Inset (B) is the equivalent circuit of the PSC

On the other hand, as Figure 5.9 (B) displays, the second semicircle corresponding to R_2 increases with longer illumination time. It is attributed to the higher amount of oxidized Spiro-OMeTAD which leads to more charge recombination at the Spiro-OMeTAD/TiO_2 interface. Some of the photo-generated electrons in the conduction band of TiO_2 can be trapped by the increasing amount of the oxidized Spiro-OMeTAD. The increasing R_2 means that the oxidized Spiro-OMeTAD also negatively affects the cell performance. Since both the positive and negative effects co-exist for the oxidized Spiro-OMeTAD in the interfaces, the solar cell performance might increase in the first 30 min followed by a minor decrease.

According to EIS, after the long wavelength light treatment, the Spiro-OMeTAD oxidization reaction proceeds with the presence of perovskite. With the results shown, we propose a spectrum-dependent mechanism for the generation of oxidized Spiro-OMeTAD. Both the three-step mechanism[54] and the two-step mechanism[100] are applicable at different spectral ranges for the perovskite solar cells. In a short wavelength range (380-450 nm), our proposed mechanism is similar to the two-step mechanism, and reactions can be written as:

$$\text{Spiro-OMeTAD}+O_2 \xrightarrow[(380\text{-}450\ \text{nm})]{h\nu} \text{Spiro-OMeTAD}^{\cdot+}O_2^{\cdot-}$$

$$\text{Spiro-OMeTAD}^{+}O_2^{\cdot-}+Li^{+}TFSI^{-} \longrightarrow \text{Spiro-OMeTAD}^{\cdot+}TFSI^{-}+Li_xO_y$$

While in a long wavelength range (> 450 nm), the three-step mechanism is more suitable with perovskite participating in the oxidization. The reaction is described as follows:

$$\text{Perovskite}+O_2 \xrightarrow[(>450\ \text{nm})]{h\nu} \text{Perovskite}^{+}O_2^{\cdot-}$$

$$\text{Perovskite}^{+}O_2^{\cdot-}+\text{Spiro-OMeTAD} \longrightarrow \text{Perovskite}+\text{Spiro-OMeTAD}^{\cdot+}O_2^{\cdot-}$$

$$\text{Spiro-OMeTAD}^{\cdot+}O_2^{\cdot-}+Li^{+}TFSI^{-} \longrightarrow \text{Spiro-OMeTAD}^{\cdot+}TFSI^{-}+Li_xO_y$$

It is important to point out that we have not ruled out the possibility that both of the mechanisms co-exist in a short wavelength range (380-450 nm), for perovskite is active in this range as well. Future work will focus on whether these mechanisms co-exist in a short wavelength range, and the percentage of Li_2O_2 and/or Li_2O in these reactions will be characterized. Whether or not the presence of the lithium oxide species has any effect on degradation of PSC is of also our interest.

5.4 Conclusion

We demonstrated a spectrum-dependent mechanism for the generation of oxidized Spiro-OMeTAD in a perovskite solar cell and observed its influence on the solar cell performance. Photons are participating in the reaction. In a short wavelength range (from 380 to 450 nm), perovskite is unnecessary for the Spiro-OMeTAD oxidization while in a long wavelength range (> 450 nm), the oxidization reaction can only proceed with the assistance of perovskite. The product, oxidized Spiro-OMeTAD, can improve the conductivity of the hole transport layer, and enhance the charge transfer at the Au/Spiro-OMeTAD interface. However, it also increases charge recombination at the TiO_2/Spiro-OMeTAD interface. As a result, the initial illumination of a perovskite solar cell can enhance the efficiency, however longer illumination times can reduce the efficiency of PSC. A better interfacial engineering method to hinder charge recombination at the TiO_2/Spiro-OMeTAD interface, while allowing increased generation of oxidized Spiro-OMeTAD would ensure better perovskite solar cell performance.

This work, in full, is a reprint of the material “Spectrum-dependent Spiro-OMeTAD Oxidization Mechanism in Perovskite Solar Cells” as it appears in the ACS Applied Materials & Interfaces, Wang, S., Yuan, W., Meng, Y. S., 2015, 7(44), 24791. The dissertation author was

the primary investigator and first author of this paper. All of the tests were performed and analyzed by the author.

Chapter 6. Role of 4-tert-Butylpyridine as a Hole Transport Layer Morphological Controller in Perovskite Solar Cells

6.1 Introduction

As an emerging photovoltaic technology with significant potential for commercialization, hybrid organic-inorganic perovskite solar cells (PSCs) have developed rapidly in recent years.[11,17,18,74] With a certified 22.1% power conversion efficiency,[10] compatibility with flexible substrates,[109,110] and low fabrication energy consumption,[63,71,111] PSCs are attracting enormous interest in both the academic and industrial field. As a p-i-n junction solar cell, a typical PSC has multiple layers and interfaces.[25,112] Understanding the function of these components in PSCs can facilitate improvements in device efficiency and stability.[101] Currently, a large number of researchers are focused on understanding the working mechanisms of the perovskite intrinsic layer and electron transport layer. [82,108,112,113] However, investigations into the role of additives in the hole transport layer (HTL) remain relatively limited.[68,114,115]

Traditionally, the HTL for PSCs consists of 2,2′,7,7′-tetrakis(N,N-di-p-methoxyphenylamine)-9,9′-spirobifluorene (Spiro-OMeTAD), bis(trifluoromethane)sulfonimide lithium salt (LiTFSI) and 4-tert-Butylpyridine (tBP) (For molecular structures of the HTL components see Figure 5.1).[2] This combination was first applied in solid state dye-sensitized solar cells (ss-DSSC).[96,116] In ss-DSSC, Spiro-OMeTAD is the hole transport material, LiTFSI is the p-dopant, and tBP is the additive that acts as a recombination blocking agent.[117] The function of tBP in ss-DSSC is the same as in liquid-based DSSC: tBP can adsorb on the surface of mesoporous TiO_2, which is the photoanode for DSSC. The adsorption of tBP on TiO_2: (1) suppresses direct contact between TiO_2 and electrolytes/hole transport materials to reduce charge recombination; and (2) negatively shifts the TiO_2 conduction band to increase the V_{oc} of

DSSC.[118,119] Due to the similarity in the device architecture for ss-DSSC and PSC, tBP is assumed to fulfill the same role in PSCs as in liquid based DSSC or ss-DSSC.[120]

However, in DSSC, dyes are discrete organic molecules which are difficult to organize into a continuous layer, whereas in PSCs, the intrinsic perovskite layer penetrates into the pores of the TiO_2 layer and also tops it as a capping layer. This suppresses the possibility of direct contact between tBP and TiO_2. Moreover, in ss-DSSC, LiTFSI triggers the oxidation of Spiro-OMeTAD.[54,55] In PSCs, despite the LiTFSI trigger, the oxidation reaction can only proceed if the perovskite layer also contributes to this process in a certain spectral range (>450nm).[56] The combined effect of the perovskite capping layer and the spectral dependence of the oxidation reaction, would allow new interactions among the components in HTL (specifically tBP) and between the HTL and intrinsic perovskite layer. This calls for a re-evaluation of the role of tBP as a charge recombination inhibitor and investigations into new interactions between the perovskite capping layer and tBP. Such detailed studies will ultimately help researchers clearly understand how PSCs works, and provide effective solutions to the stability issue ensuring better success of this technology towards commercialization.

Recent reports have observed pin-holes in the HTL of PSCs.[93] These are considered to contribute to the poor stability of PSCs; oxygen and moisture in ambient environment can permeate through these pin-holes and cause degradation of the perovskite intrinsic layer, but the reason for the generation of pin-holes in HTL is still unclear.[121]

In this work, tBP is found to function as a morphology controller in the HTL of PSCs. Our observations suggest that, tBP reduces phase separation in the stock solution prior to spin-coating. This effect improves the film quality of the HTL by decreasing inhomogeneous regions. Using Scanning Electron Microscopy (SEM) we prove that the presence of tBP significantly

influences the HTL surface, by reducing the number of 'pits' (also reported as pinholes [30,31]). On the other hand, high resolution cross-section Transmission Electron Microscopy (TEM) images show that the HTL undergoes morphological changes after long term (>1000 hours) storage of PSC. With the help of Atom Probe Tomography (APT), 3D visualization of the water distribution at HTL/perovskite interface is possible. By combining the phenomena we observe in TEM and APT, a PSC failure process mechanism is proposed, along with the morphological change of the HTL due to the evaporation of tBP. Our results indicate that tBP not only fulfills its function as previously reported for ss-DSSC, but also acts as a morphology controller directly affecting device stability.

6.2 Experimental Methods

All reagents, unless otherwise stated, were purchased from Sigma-Aldrich.

6.2.1 Methylammonium iodide (MAI) synthesis

15 mL of 33 wt% methylamine solution in anhydrous methanol was reacted with 15 mL of 57 wt% hydroiodic acid in a flask for 1 hour. After evaporating all solvents, the mixture was dissolved in anhydrous ethanol. Ethyl ether was used to precipitate MAI from the solution. The MAI was dried overnight in a vacuum oven, and a white crystalline powder was obtained as the final product.

6.2.2 Perovskite solar cells (PSCs) fabrication

PSC fabrication was based on the sequential deposition method.[18] A TiO_2 compact layer was spin-coated on cleaned FTO glass. After sintering, a mesoporous TiO_2 layer was spin-coated onto the TiO_2 compact layer and sintered again. PbI_2 (Alfa Aesar) was dissolved in dimethyl formamide and spin-coated onto mesoporous TiO_2. Then the films were dipped in MAI solution (isopropanol as the solvent). After thermal annealing, the films were spin-coated with a solution

containing Spiro-OMeTAD (Merck), tBP, and LiTFSI which were dissolved in chlorobenzene. Finally 80 nm of gold was evaporated onto the films. For more detailed information (spin-coating speed/time, solution concentration, and annealing condition) see reference.[96]

6.2.3 Characterization:

Scanning Electronic Microscopy (SEM) images were taken with a FEI SFEG UHR SEM operated at 10kV. Samples were coated with iridium before taking SEM images to avoid beam drift for semiconducting and insulating materials.

Transmission electron microscopy (TEM) images were taken with a FEI 200kV Sphera Microscope. Samples for TEM were prepared by focused ion beam (FEI Scios DualBeam FIB/SEM). Regions of interest were deposited with 2 um thick Pt for protection during ion etching. After etching from the substrate, the samples were lifted by a tungsten needle (FEI EasyLift LT NanoManipulator). Before disconnecting the sample from the needle, samples were attached onto the FIB lift-out grid (Copper PELCO FIB Lift-Out Grid). Subsequently samples attached onto the lift-out grid were thinned to within 100 nm by a Ga^{2+} ion beam. In addition, the EFTEM images and EELS spectra were acquired using a Gatan Enfina spectrometer with a collection angle of 52 mrad and convergence angle of 30 mrad.

Samples for atom probe tomography (APT) were prepared and analyzed at the Environmental and Molecular Sciences Laboratory at PNNL.

In brief samples were prepared from fabricated PSC devices, in the form of tips, using FEI Helios dual-beam focused ion beam/scanning electron microscope (FIB/SEM) equipped with an Omniprobe. A wedge shaped lift-out section was prepared by milling at 22 degrees. The liftout section was controlled using an in-situ micromanipulator (Omniprobe) and 2 μm sections were cut and affixed on a Si microtip array followed by Pt deposition on either side to hold the wedge in place. An annular milling pattern with progressively smaller diameter was used to get

the shape of a tip. A final low beam energy (~ 2kV) exposure was used to give the tip its final shape as well as remove surface regions, which are prone to maximum Ga damage. The end radius at the tip was less than 100 nm.

As prepared sample tips were then analyzed using a LEAP (local electrode atom probe) 4000XHR with a detector efficiency of ~40%. A temperature of 60 K and laser energy (~ 100 pJ) was used to ensure field evaporation of ions in a regular manner. The laser energy, detection rate and temperature were optimized for our samples. The reconstruction to obtain the 3-D maps and the analysis were done using the IVAS® software.

Fourier transform infrared spectroscopy (FTIR) with attenuated total reflectance (ATR) attachment (Nicolet 6700 with Smart-iTR) was applied for the FTIR test. Samples for FTIR were spin-coated on CaF_2 substrates at 2000 r.p.m. and 30 s as thin films.

6.3 Results and Discussion

6.3.1 HTL Infiltration Behavior in PSCs

Majority of our samples in this study, are prepared by focused ion beam (FIB) which were utilized for high quality Scanning Electron Microscopy (SEM) and TEM imaging[122–125]: The FIB milling/polishing process ensured that the sample had a smooth surface. Furthermore, using a FIB-based milling process allowed the sample to be thinned to 100 nm required for TEM characterization. As shown in Figure 6.1(A), the morphological contrast for every layer in PSC is distinguishable in BF-TEM. Based on FIB-prepared PSC samples for cross-section TEM imaging, we progress towards understanding the infiltration extent of HTL in PSCs. In ss-DSSC, the pore filling percentage of the HTL in a mesoporous TiO_2 photoanode is around 60% - 85% (the thickness of mesoporous TiO_2 is ~2.8um).[126,127] These reports also demonstrate that reducing mesoporous TiO_2 layer thickness can increase the pore filling percentage. In

mesoporous TiO_2-based PSCs, the optimized thickness of mesoporous TiO_2 is around 300 - 400 nm. If the HTL infiltrates into mesoporous TiO_2 to the same extent as it does in ss-DSSCs, the pore filling percentage in PSCs should be higher than 60 - 85% because of the thinner TiO_2. However, our observations show that the pore filling percentage of the HTL in TiO_2 is much lower than 60% due to the presence of the perovskite layer that has infiltrated the mesoporous TiO_2 layer.

In PSC, the majority of the TiO_2 surface is covered with a perovskite capping layer, although some regions have poor coverage. Here, three components cross-section Energy Filtered TEM (EF-TEM) mapping is applied to display the infiltration behavior of HTL under the competing effect of the perovskite infiltration in mesoporous TiO_2. Two PSC samples were prepared by FIB for EF-TEM, one with poor perovskite capping layer coverage on top of the mesoporous TiO_2, the other one with rich perovskite capping layer coverage. As shown in Figure 6.1(B), even in perovskite poor coverage regions, the infiltration of the HTL into mesoporous TiO_2 is limited. Most of the pores within the TiO_2 layer are filled with perovskite instead of HTL (Figure 6.1 (B) green regions). In TiO_2 with pores deeper than 150 nm from the surface, no HTL is observed. However, when the perovskite coverage is better, as shown in Figure 6.1(C), the area of TiO_2 infiltrated by the HTL is even smaller. The EF-TEM mapping indicated that under the competition of the perovskite, the infiltration of the HTL to mesoporous TiO_2 is limited. The more perovskite capping layer cover on top of TiO_2 the less the HTL can infiltrate into the mesoporous TiO_2.

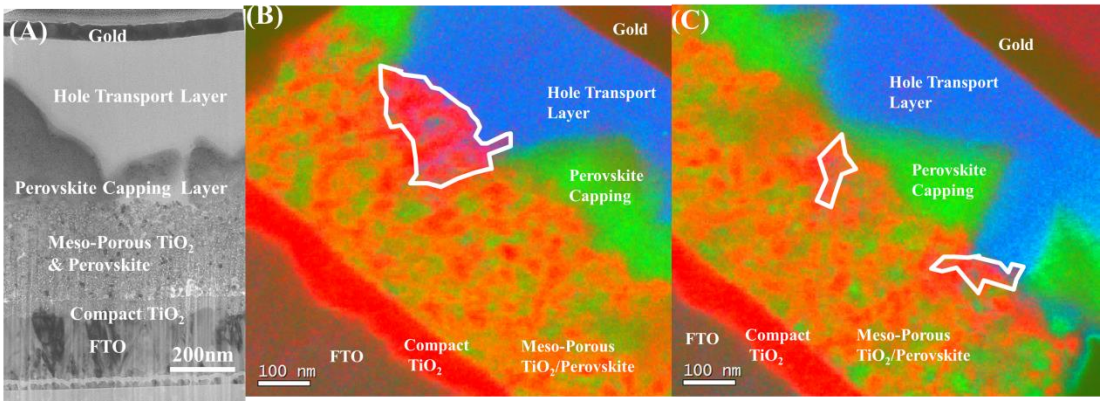

Figure 6.1 Correlation between perovskite coverage and HTL infiltration. (A) Bright Field TEM cross-section image of PSC prepared by focused ion beam (FIB). Energy Filtered-TEM mapping of a PSC cross-section with (B) poor / (C) Rich perovskite coverage.

In previous reports, a penetration depth of ~ 100 nm for the HTL is observed, which show strong agreement with our experimental observations.[124] Since then, several groups have adopted superior fabrication procedures. A denser perovskite capping layer can further limit the pore-filling of the HTL in TiO_2. Moreover, in planar heterojunction PSCs, which are devoid of mesoporous TiO_2, the TiO_2/HTL interface is further reduced. However, tBP is still used in majority of PSCs architectures and device configurations. Hence, it should function differently in PSCs than in DSSCs.

6.3.2 tBP HTL Morphology Control Effect

Due to the limited penetration depth and low pore filling percentage, the TiO_2/HTL interface in PSCs is much smaller than in ss-DSSCs. As a result, tBP acts only minimally to

prevent direct contact between Spiro-OMeTAD and TiO_2. However, as we observe, tBP does control the morphology of the HTL.

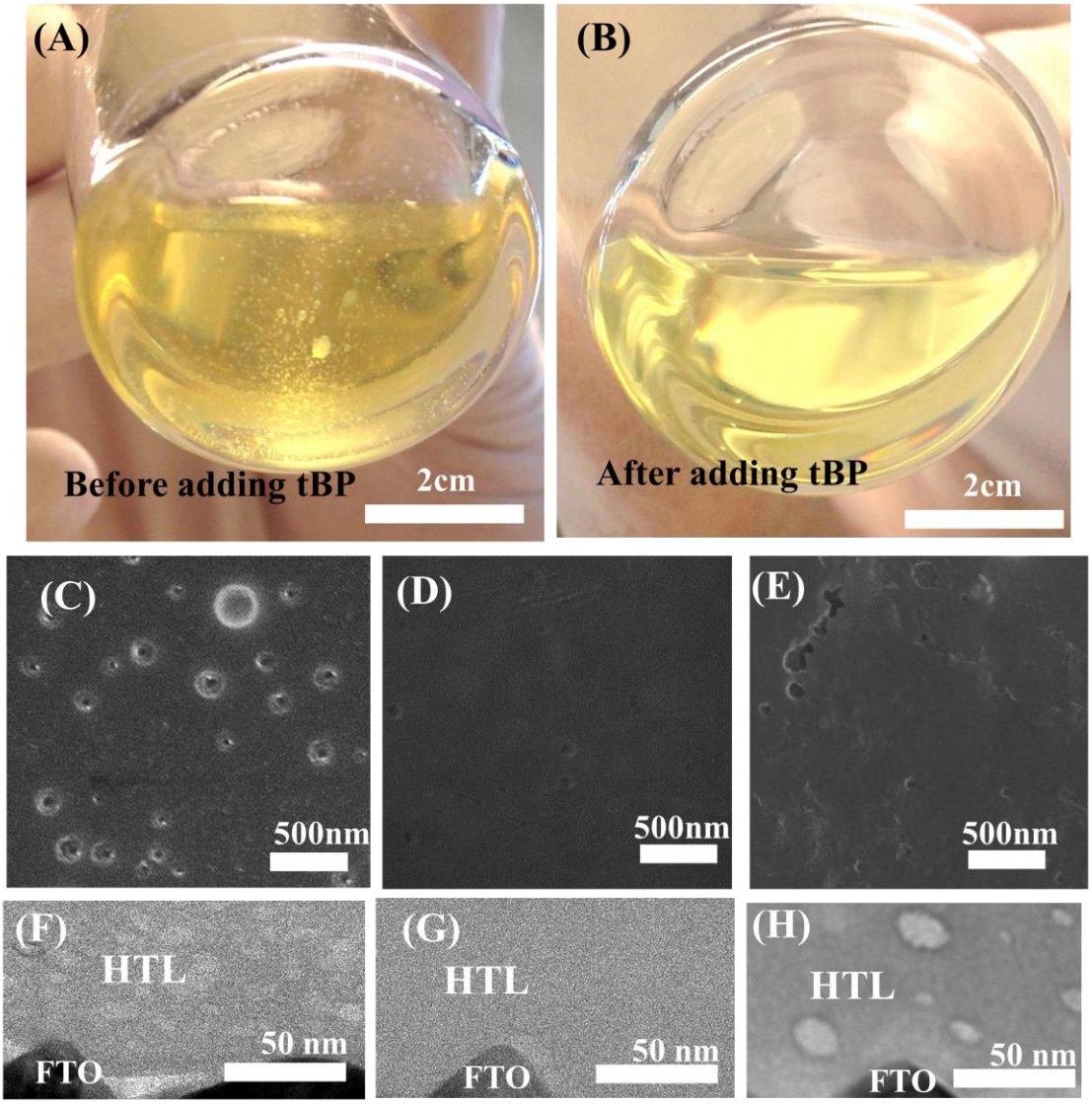

Figure 6.2 HTL solution used for spin coating (A) Before/ (B) After adding tBP. Top-view SEM of the HTL (C) without/(D) with tBP, and (E) with tBP after vacuum treatment (10^{-4} Pa). Cross-section BF-TEM images of the freshly prepared HTL (F) without/ (G) with tBP, and (H) with tBP after vacuum treatment (10^{-4} Pa).

Before adding tBP, as shown in Figure 6.2(A), the HTL solution used for spin-coating is phase separated: the LiTFSI/acetonitrile solution (acetonitrile is the solvent to dissolve LiTFSI before adding to Spiro-OMeTAD solution) is immiscible with the Spiro-OMeTAD/chlorobenzene solution (chlorobenzene is the solvent for spin-coating of HTL). Majority of the LiTFSI/acetonitrile solution tends to accumulate at the bottom of the Spiro-OMeTAD/chlorobenzene solution as small liquid droplets. After adding tBP, as shown in Figure 6.2 (B), all liquid droplets disappear, which indicates that tBP improves the solubility of LiTFSI in the Spiro-OMeTAD solution. It is possible that some complexes are formed by tBP and LiTFSI to reduce the phase separation in HTL solution and further influence the morphology of the HTL after spin-coating.

Because the existence of tBP guarantees the uniformity of HTL solution, as a result, it can affect the morphology of the spin-coated films. Several freshly prepared HTL samples were characterized by SEM/TEM as shown in Figure 6.2(C) to (H). In Figure 6.2(C), a top-view SEM image show that pits form on the surface of the HTL in the absence of tBP. After adding tBP, as Figure 6.2(D) displays, both the size and number of the pits are significantly reduced. The homogeneous nature of the solution facilitates formation of a uniform film with a limited number of pits.

In order to prove that these pits in the HTL are indeed formed due to a lack of tBP, overnight vacuum treatment (10^{-4} Pa) was applied to a HTL with tBP. It is reported that tBP evaporates under vacuum environment and no XPS signals are observed related to tBP elements.[93] As shown in Figure 6.2(E), the number and the size of the pits on the surface of the HTL increase after overnight vacuum treatment. The morphological change from Figure 6.2(D) to (E) can be attributed to the evaporation of tBP. Its disappearance/reduction causes the HTL

film to revert back to an inhomogeneous state, thereby resulting in the reappearance of more pits. Moreover, a few pits are located in the HTL even with tBP (Figure 6.2(D)), which we ascribe to the volatile nature of tBP on the surface. tBP can partially evaporate at the surface of the HTL, allowing a small portion of LiTFSI to regather and form pits.

To further study the morphological control of tBP on the HTL, FIB was used to prepare cross-section HTL samples with and without tBP. This enabled us to observe the morphology of the bulk of the film via BF-TEM at high resolution. Figures 6.2(F) to Figure 6.2(H) are BF-TEM images of the HTL cross-section without tBP, with tBP and with tBP after over night treatment, respectively. In Figure 6.2(F), without tBP, the HTL has an inhomogeneous morphology. Several bubble-like structures appear in the HTL. When the HTL contains tBP, as shown in Figure 6.2(G), the bulk of the film is homogeneous. After overnight vacuum treatment of the tBP-contained film, Figure 6.2(H), inhomogeneous regions appear again. For the various treatment histories, the morphology of the inhomogeneous regions in the tBP-free sample and that of the vacuum treatment tBP sample are slightly different, but the size and the distribution of the inhomogeneous regions for these two samples are in the same range.

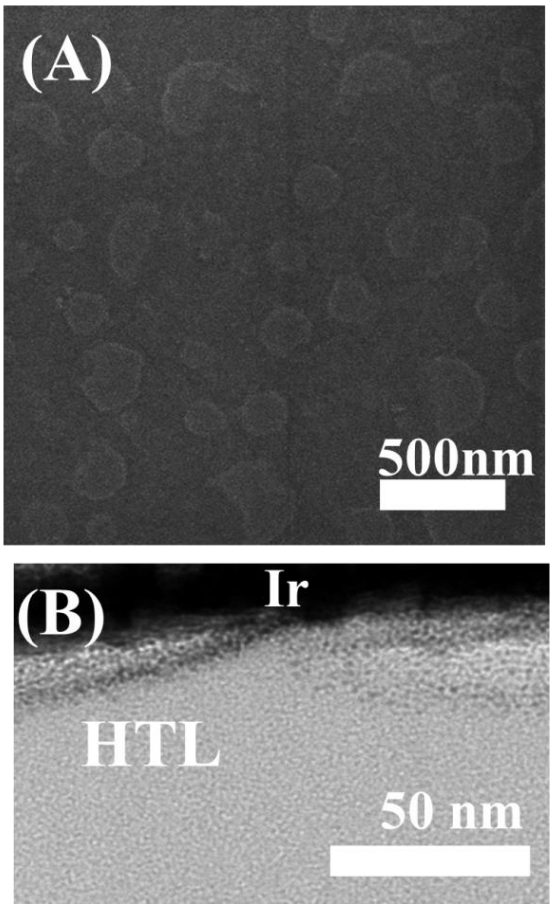

Figure 6.3 (A) Top-view SEM images of the freshly prepared HTL with tBP after thermal annealing treatment. (B) Cross-section BF-TEM images of the freshly prepared HTL with tBP after thermal annealing treatment.

In addition, we also characterized the tBP-contained film after thermal annealing. 200℃ was selected as the heat treatment temperature, as this temperature is above the boiling point of tBP and below the melting points for LiTFSI and Spiro-OMeTAD. The morphology of the top view (Figure 6.3 (A)) and the cross-section view (Figure 6.3 (B)) of the thermal annealing film is characterized. In Figure 6.3(A), the number and size of the pits on the surface of the HTL increase after heat treatment. However, the morphology and location of the inhomogeneous regions in cross-section image of the annealed tBP sample is different compare with the vacuum

treatment sample and the tBP-free sample. The inhomogeneous regions of the tBP-free and vacuum treatment samples show more small bubble-like regions that are mainly located at bulk of the film. These inhomogeneous regions show brighter contrast compared with the rest of the film. While in Figure 6.3 (B), the annealed sample's inhomogeneous regions are on top of the film, they show darker contrast compared with the rest of the film. These differences can be attributed to the melting of LiTFSI on 200 ℃ homogenizes bulk of the thermal annealing film, however, it still can not prevent the surface morphological change due to the evaporation of tBP. In conjunction with the top view SEM and cross-section TEM results (Figure 6.2 (C) to (H), 6.3(A) to (B)), it is obvious that tBP can affect both the surface and bulk morphology of HTL.

Previous reports described the non-uniform structure of the HTL as 'pinholes': the authors proposed that the pinholes pass through the entire HTL layer, which put moisture and air in direct contact with the surface of perovskite layer and trigger further degradation.[93,121] If pinholes did indeed exist in the HTL, a cross-section TEM image of a PSC would reveal this specific morphology. However, the cross-section TEM images (Figures 6.1 and 6.2) prove that the HTL is uniform (in presence of tBP). In Figure 6.4, a cross-section BF-TEM image of a PSC showing a larger region for the HTL also indicates that the bulk of the HTL is homogeneous and contains no pinholes.

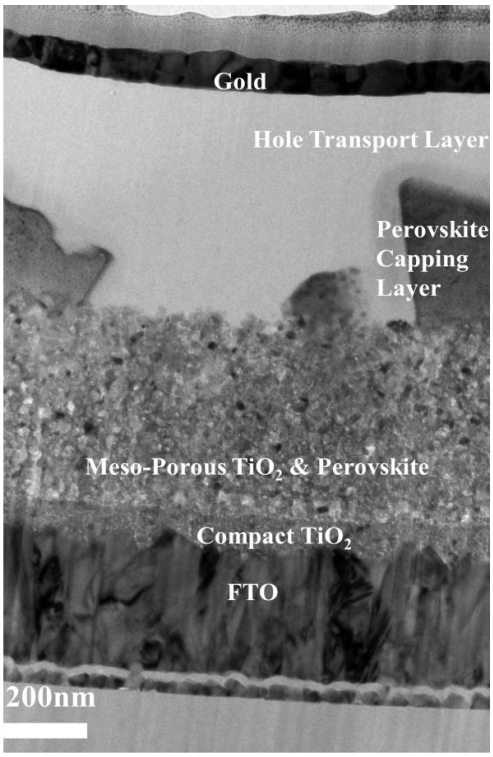

Figure 6.4 Cross-section BF-TEM image of a PSC, which indicates that the HTL has a homogeneous morphology. The sample was intentionally prepared with less perovskite coverage in order to display more HTL area.

On the other hand, the metal (top electrode)/HTL interface is not flat, which suggests that the surface morphology has shallow pits instead of pinholes (Figure 6.5).

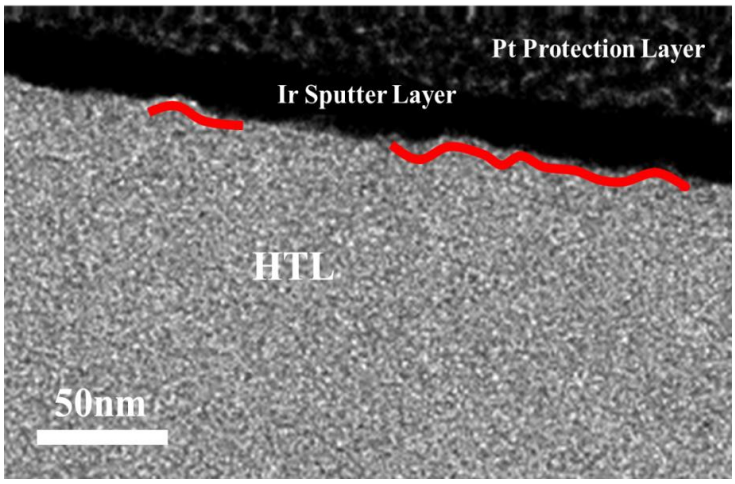

Figure 6.5 Cross-section BF-TEM image of the HTL with a metal capping layer. It reveals the curved structure of the HTL/metal interface. The red line marks the curved portions of the interface. The sample was prepared by FIB.

To demonstrate the difference between a 'pit' and 'pinhole' in the HTL, a picture is shown in Figure 6.6: although the morphology of the HTL looks similar from a top view, in the cross-section the 'pinholes' and 'pits' are easy to distinguish. To get the accurate morphological information of HTL and to prevent the FIB process from damaging the sample, two measures were taken into our experiment: (1) Before FIB process, all samples were pre-deposited with a metal protecting layer (Pt or Ir 200 nm and then 2um Pt), which can prevent the beam from damaging the top of the HTL. (2) During FIB thinning process, only 5kV voltage and 7pA current were applied to the sample when the sample thickness is smaller than 200 nm. This measure can minimize the beam-induced damage to only 10 nm. [128]

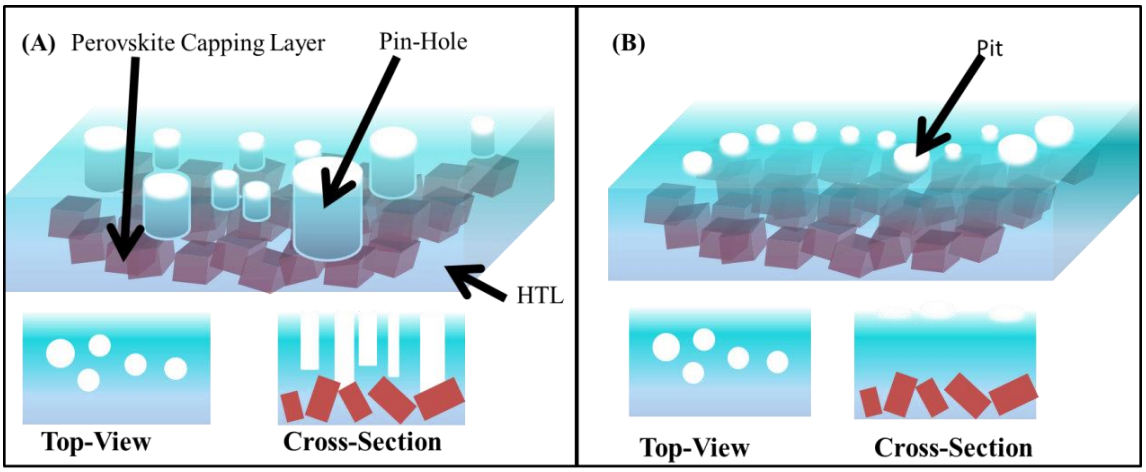

Figure 6.6 Schematic of the HTL with a perovskite capping layer (A) pin-hole model; (B) pit model. They have similar top-view morphology, but the cross-section morphology is clearly distinguishable.

6.3.3 HTL morphological change in PSCs

Apart from our observation of pits on the surface of the HTL (in the absence of tBP), its effect on the stability still needed further investigation. Since the evaporation of tBP can also lead to morphological change of the HTL as mentioned earlier, we suspect this effect exists in a real device and finally influences the device performance. To study this mechanism, we observe the long-term morphological change of the HTL in an unsealed full PSC. We store the PSC samples under ambient dark conditions with 10% moisture for 1000 hours. Four samples for BF-TEM were prepared by FIB on the same cell after different storage time (0, 200, 500, and 1000 hours).

As shown in Figure 6.1 (A), at the start, the HTL is homogeneous. As discussed before, that is because tBP promotes miscibility of LiTFSI and Spiro-OMeTAD. After 200 hours, as Figure 6.7(A) displays, inhomogeneous dark regions appear on the HTL. These regions are due

to the accumulation of Li salt which occurs due to the loss of tBP by evaporation. Figure 6.7(B) shows the morphology of the HTL after 500 hours. The majority of the dark regions disappear, even as bubble-like structures are generated. This likely occurs because of the hygroscopicity of LiTFSI: moisture can easily react with the accumulated LiTFSI seen in Figure 6.7(A). The hydration of LiTFSI therefore leads to the bubble structures in the HTL. Finally, in Figure 6.7(C), after 1000 hours, the perovskite has decomposed. These images display that the morphological change, in other words, the failure process of PSCs, is initiated from the HTL instead of the perovskite layer followed by eventual degradation of perovskite. The related photo current density-voltage curves (J-V curves) and device parameters for the stored cells are shown in Figure 6.7(D) and Table 6.1. Compare with the freshly prepared PSCs (12.6%), the performance decay of the 250 hours (10.9%) and 500 hours (7.51%) PSCs are not as obviously as the 1000 hours PSCs. It is consistent with the TEM results since the decomposition of the perovskite layer at the first 500 hours is limited while at 1000 hours, perovskite layer has decomposed.

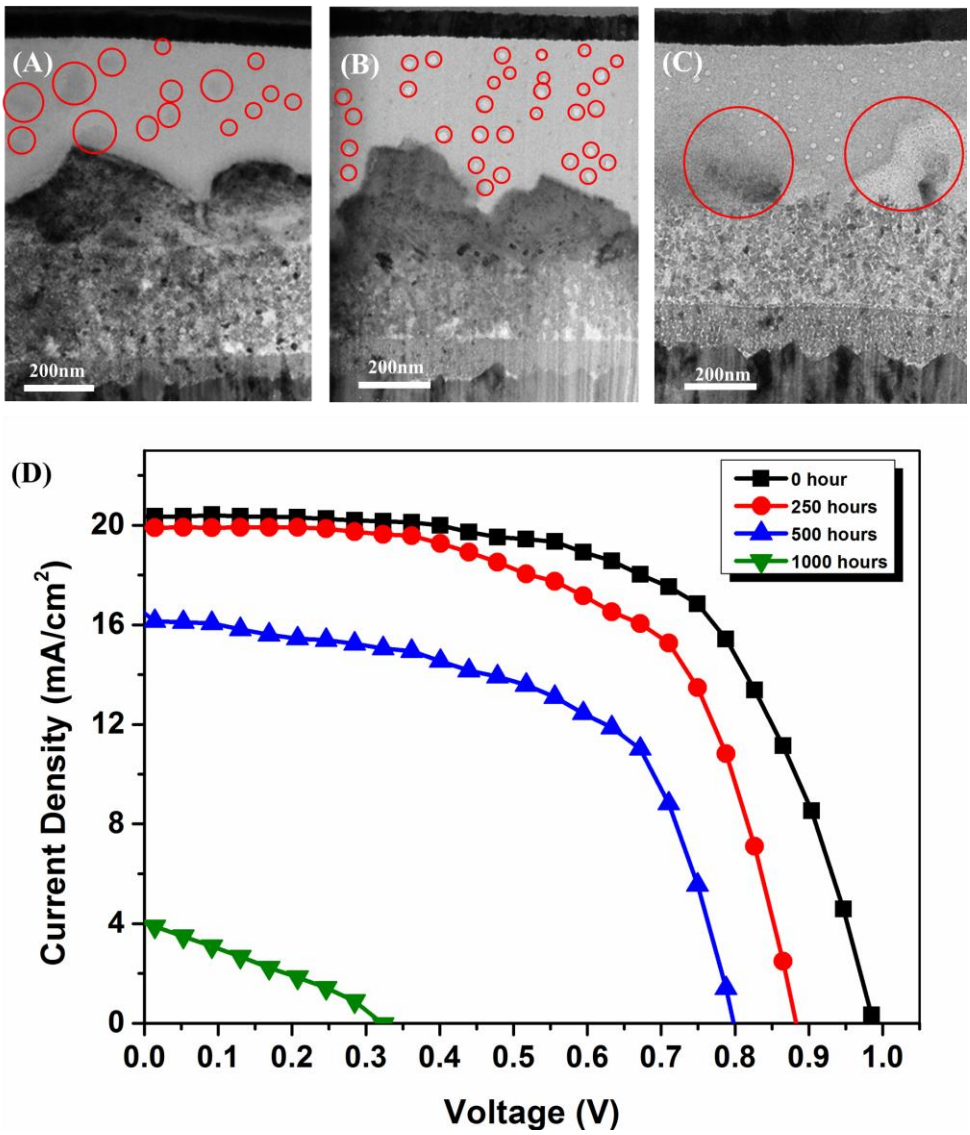

Figure 6.7 BF-TEM cross-section images of the long-term stored PSC after (A) 200 hours, (B) 500 hours, and (C) 1000 hours. (D) J-V curves of the stored perovskite solar cells. Each curve is the average of 10 cells prepared at the same batch of the TEM sample.

Table 6.1 Cell parameters of the perovskite solar cells stored for 1000 hours at 10% humidity ambient dark condition

	V_{OC} (V)	J_{SC} (mA/cm^2)	Fill Factor	Efficiency (%)
0 hour	0.987	20.38	0.63	12.6
250 hour	0.886	19.97	0.62	10.9
500 hour	0.799	16.16	0.58	7.51
1000 hour	0.331	3.90	0.29	0.38

Based on the morphology control effect of tBP on HTL and the failure process of the PSCs, a mechanism regarding the long-term morphological change in a perovskite solar cell is presented now. As displayed in Figure 6.8, at the start (right after device fabrication), the existence of tBP guarantees a uniform HTL, with minimal shallow pits located on the surface the of the HTL. After tBP evaporates, the Li salt accumulates, shown as dark circular regions. These regions are further hydrated to create void structures in the HTL which finally lead to decomposition of the perovskite layer. It should be noted that these events may not strictly proceed one after the other, but may instead occur at the same time. During the LiTFSI hydration process, for instance, the decomposition of the perovskite may have already begun since water is already in the HTL.

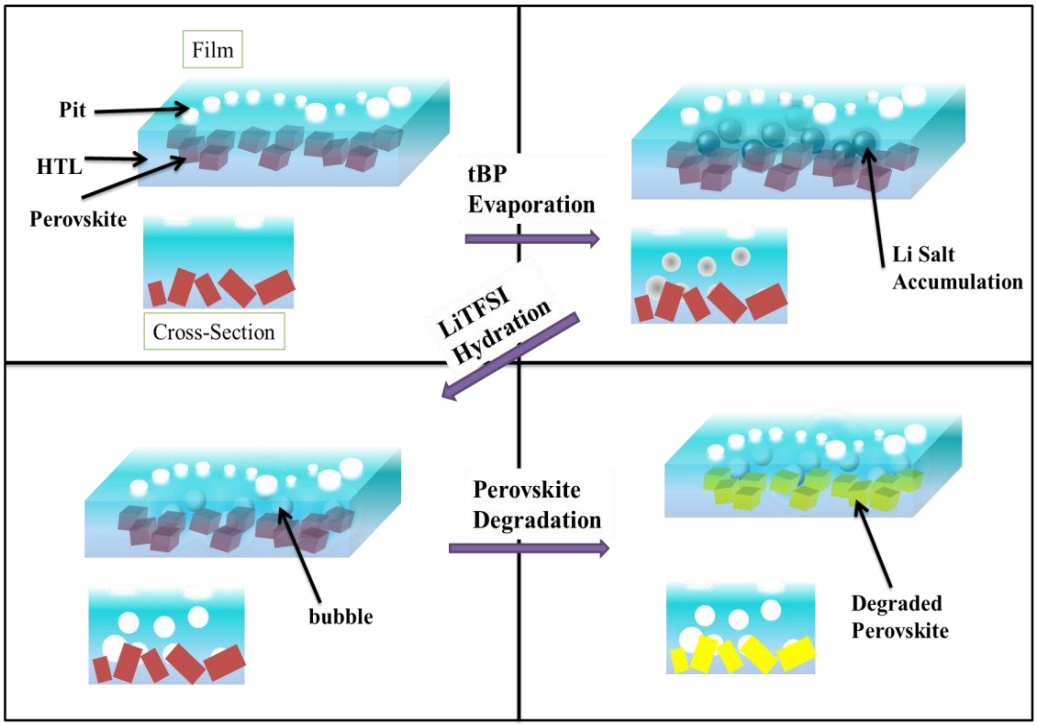

Figure 6.8 Schematic of the morphological change of the HTL/perovskite layers as they are stored in dark conditions.

6.3.3 Humidity Accumulation Characterizations in PSCs

To further confirm that the lack of tBP can lead to the increasing amount of water in HTL, four fresh-prepared Spiro-OMeTAD films with various components combinations were characterized by Fourier transform infrared spectroscopy (FTIR). As shown in Figure 6.9, films of pure Spiro-OMeTAD (black line), Spiro-OMeTAD/tBP (red line), and Spiro-OMeTAD/tBP/LiTFSI (dark green line) all display similar peaks. That is because the primary component of the HTL film is Spiro-OMeTAD (in accordance with the weight percentage of the HTL spin-coating solution). However, a water peak is observed in the Spiro-OMeTAD/LiTFSI sample (blue line). This broad peak at ~3600 cm^{-1} corresponds to the O-H stretching mode of water in FTIR. In contrast, no water peak appears in the Spiro-OMeTAD/ tBP/LiTFSI sample

(dark green line). This indicates that tBP prevents the accumulation of LiTFSI in Spiro-OMeTAD films, thereby reducing the possibility of LiTFSI hydration since the material is well dispersed throughout the Spiro-OMeTAD and shielded by tBP. The mechanism of how tBP prevents LiTFSI hydration at a chemical level will be the scope of our future work.

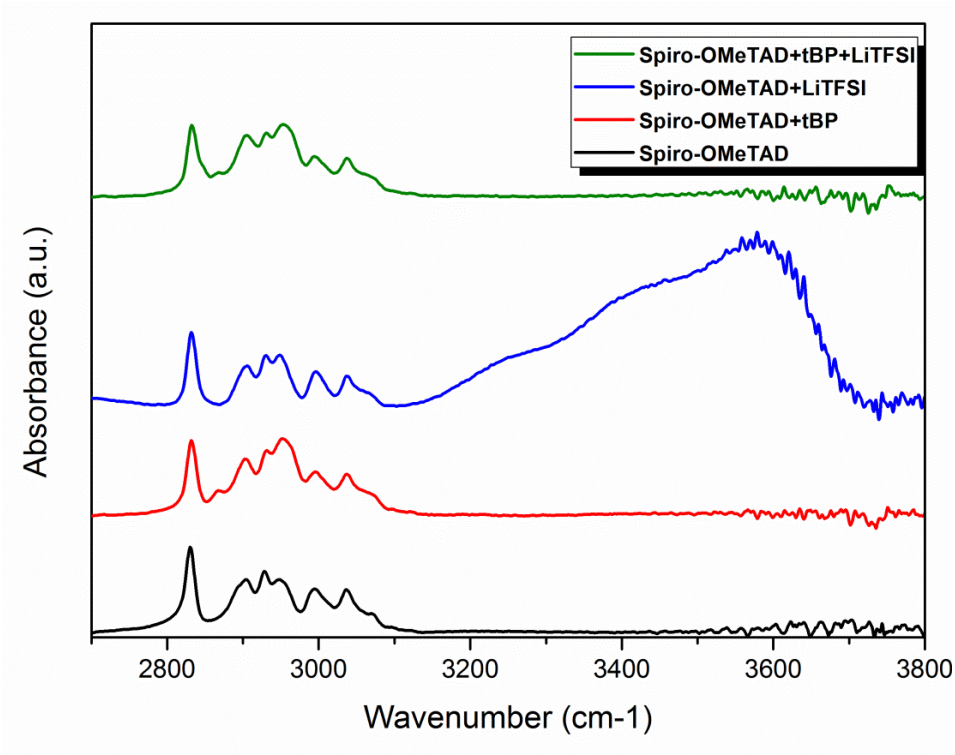

Figure 6.9 FTIR spectra of Spiro-OMeTAD films with various component combinations

The FTIR study confirmed the presence of moisture in films without tBP, but in order to visualize that moisture truly exists in the HTL for a full cell device structure, we utilized laser-assisted atom probe tomography (APT). With the unique ability of APT to obtain three dimensional (3D) position information and compositional mapping of energy materials,[129,130] we constructed a map of the water accumulated in PSCs at the HTL/ perovskite interface. The PSC devices were stored for over 500 hours prior to sample preparation for APT analysis. This

corresponds to the morphology of Figure 6.7 (B). In this state, as mentioned before, tBP would evaporate allowing the accumulation of LiTFSI and its possible hydration.

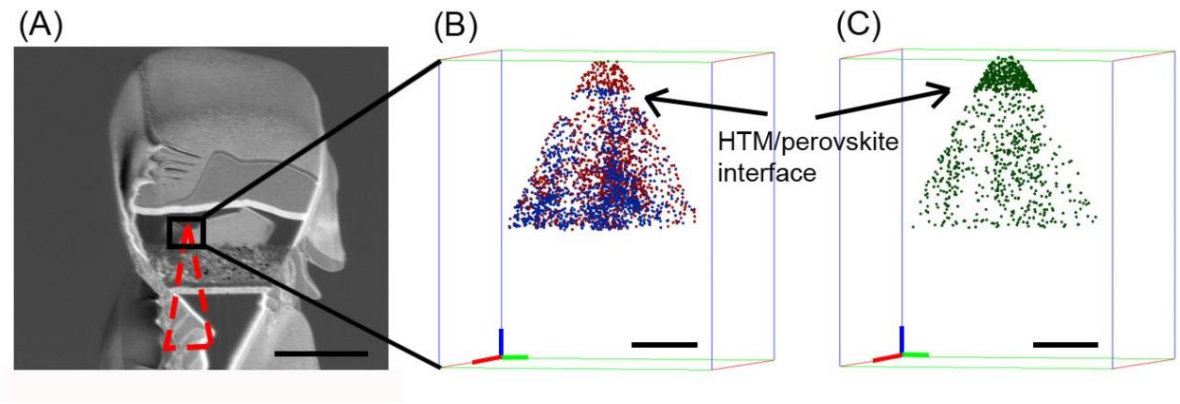

Figure 6.10 3D APT maps of HTL/perovskite layers after > 500 hours storage (A) SEM of an APT sample section (Scale bar is 1 um). (B) 3D elemental maps of Pb (blue dots) and F (red dots). (C) APT map of H_2O showing its distribution in 3D. (Scale bar in (B) and (C) are 10 nm.)

Figure 6.10(A) displays a perovskite solar cell cross section wedge lifted out for preparing an atom probe needle specimen. Various layers in the device architecture are clearly visible. The annular milling process during final stages of the needle specimen preparation was controlled to retain the HTL layer on the specimen apex and then proceed to the perovskite layer below, with the interface in between. In Figure 6.10 (B), the APT maps show the clear boundary between F (red) and Pb (blue), corresponding to the perovskite/HTL interface. Pb and F maps are used since they are the sole indicators for perovskite and LiTFSI respectively, not present in any other layers. Although fluorine signatures can be obtained from the FTO (fluorine doped tin oxide) layer, atomic positions of F above the Pb region do not conform to the position of the FTO layer. Another caveat is the low analysis temperature used for APT analysis (60 K) which is

below the phase transition temperature for the intrinsic perovskite layer. We do not expect that the phase transition would affect the ordering of the layers and the interfaces.

As shown in Figure 6.10 (C), the chemical map for water indicates a strong concentration at the specimen apex region as opposed to the entire region of analysis. To the best of our knowledge, such a strong concentration could not possibly occur from a background signal (see Figure 6.11 for a more quantitative analysis). This region of water accumulation is concurrent with regions of high F concentration. Thus we conclude that water accumulates in the HTL rather than the perovskite layer.

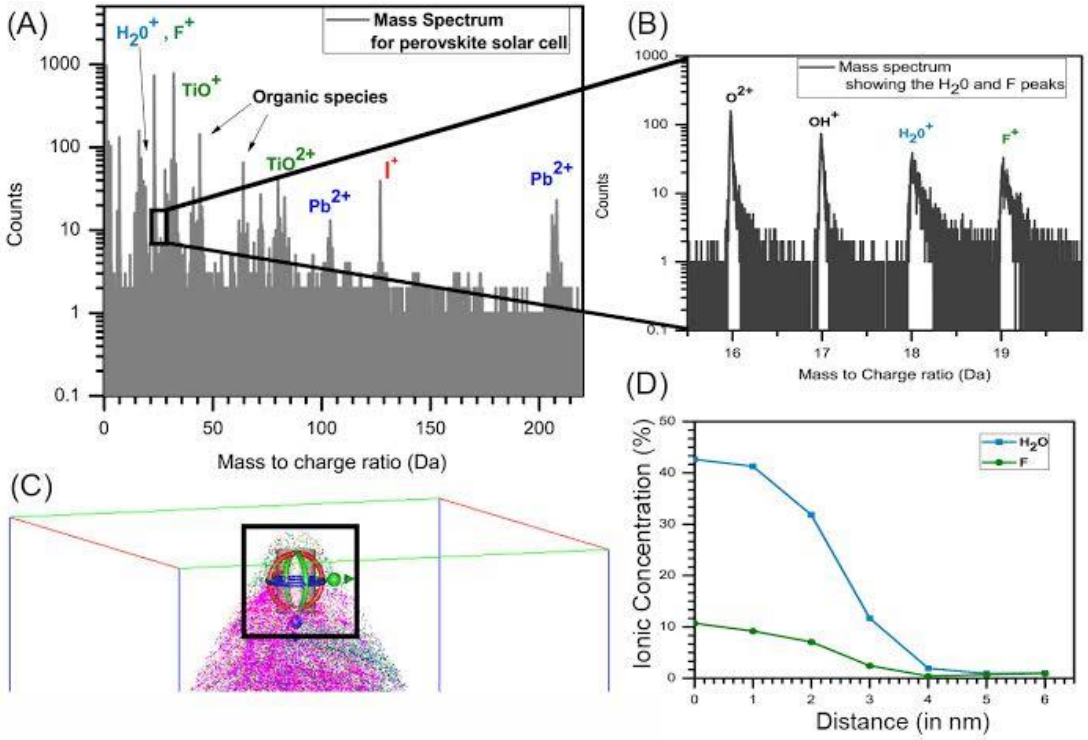

Figure 6.11 Additional analysis for atom probe tomography performed on perovskite solar cells.

In comparison to similar chemical maps for F and H_2O, using freshly prepared samples (see Figure 6.12 for more details) with no ageing, the total counts for H_2O and F ions are 5 times higher. These observations are also consistent with our TEM results and FT-IR data. In PSCs

samples stored in ambient under dark conditions, the amount of tBP in the HTL is reduced due to its relatively low boiling point and volatile nature. As a result, the HTL prefers to adsorb water due to the hygroscopicity of LiTFSI.

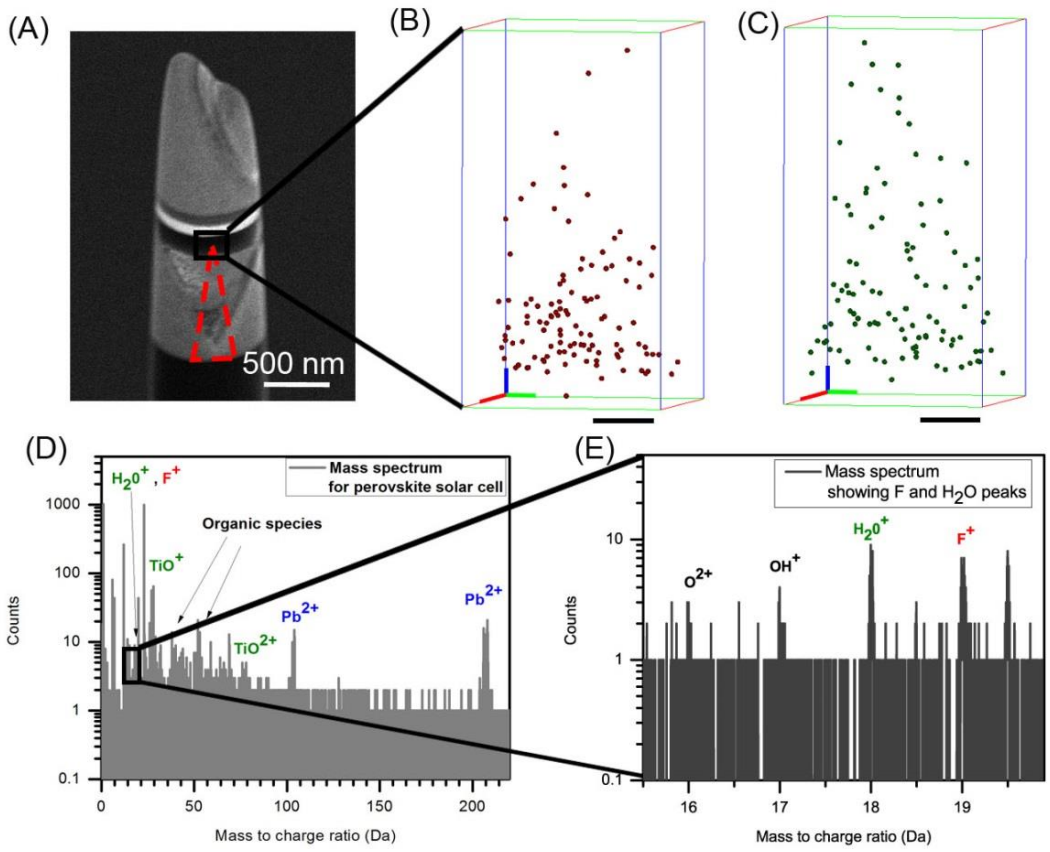

Figure 6.12 Analysis for APT on freshly prepared PSC (A) the SEM image for the perovskite layer. (B) APT map of F (fluorine) (C) APT map of H_2O. (Scale bar in (B) and (C) are 8 nm) (D) the mass spectrum for the analysis region shown in (A). (E) Zoom in of the mass spectrum

6.4 Conclusion

In Conclusion, the function of tBP in PSCs was re-evaluated to understand its influence on device stability. Due to the limited penetration depth of HTL into mesoporous TiO_2, it is unlikely that the additive serves only to prevent contact between the Spiro-OMeTAD and TiO_2

layers as traditionally assumed. Based on our observations, tBP functions as a morphological controller for the HTL. It prevents phase separation of LiTFSI and Spiro-OMeTAD during spin-coating of the solution, resulting in a uniform HTL film. The absence of tBP leads to inhomogeneous films and also causes the appearance of large pits on the surface of the HTL. tBP-free HTL easily absorbs water due to the hygroscopicity of accumulated LiTFSI and further lowers the stability of PSCs. In PSCs stored in ambient dark conditions for 1000 hours, the slow evaporation of tBP (as it is the only liquid component in PSCs), leads to all of the above discussed phenomena. Li salt accumulates and generates 'dark regions' in the HTL. These dark regions then turn into void bubble structures due to the hydration of Li salt. Finally, the water contained in the HTL contributes to perovskite degradation. Since the evaporation of tBP is a primary contributor to the poor stability of PSCs, we suggest that the performance of PSCs can be enhanced by utilizing other pyridine derivatives that can fulfill the same functions as tBP but have much higher boiling points.

This Chapter, in full, is a reprint of the material "Role of 4-tert-Butylpyridine as a Hole Transport Layer Morphological Controller in Perovskite Solar Cells", Nano Letters, Wang, S., Sina, M., Parikh, P., Uekert, T., Shahbazian, B., Devaraj, A., Meng, Y. S., 2016, 16(9), 5594. The dissertation author was the primary investigator and co-first author of this paper. All of the experiment parts were performed and analyzed by the author except for the energy-filtered transmission electron microscope and atom probe tomography.

Chapter 7. tBP-LiTFSI Complexes in Perovskite Solar Cells

7.1. Introduction

Lead halide based perovskite materials have been widely applied as core components for different types of energy conversion devices such as next-generation solar cells, X-ray detectors, light-emitting diodes, and laser generators.[11,131–133] For the next-generation solar cells, power conversion efficiency (PCE) of 22.7% has been achieved using single-junction perovskite solar cells (PSCs).[10] This can be attributed to the tunable bandgap, long carrier diffusion length, and low exciton binding energy of various perovskite materials.[6-8] A PSC is a p-i-n junction device, which consists of electron-transport layer (ETL), intrinsic layer, and hole transport layer (HTL). The lead halide perovskite materials function as an intrinsic layer that can absorb photons and generate free electron-hole pairs. The electrons are transferred to the ETL while the holes are extracted by the HTL to finish regenerating the perovskite layer. [13]

For the HTLs, organic molecules,[101,115,135–137] polymers,[42,138] and inorganic semiconductors[68,76,139,140] have all been applied for PSCs. Though some recent publications show that inorganic HTLs can achieve over 20% efficiency with better device stability,[76] the highest device performance is still based on the doped organic/polymeric HTL.[46]

The most commonly used organic and polymeric hole-transport materials in PSCs are 2,2′,7,7′-tetrakis(N,N-di-p-methoxyphenylamine)-9,9′-spirobifluorene (Spiro-OMeTAD) or Poly[bis(4-phenyl)(2,4,6-trimethylphenyl)amine] (PTAA).[18,46,74] Bis(trifluoromethane)sulfonimide lithium salt (LiTFSI) and 4-tert-Butylpyridine (tBP) are added to Spiro-OMeTAD or PTAA in the HTL as additives. Though LiTFSI and tBP were termed as

'additives' indicating that they are not the major components, on a molecular level, tBP and LiTFSI are the dominant components in HTL. Despite in Spiro-OMeTAD based HTL, Spiro-OMeTAD accounts for ~70% (weight percentage), the molar ratio of Spiro-OMeTAD:LiTFSI:tBP is ~1:0.5:3. It means that the composition of HTL is dominated by LiTFSI and tBP while these additives could play a significant role in the chemical environment of HTL. This evaluation is based on the commonly reported concentration condition of Spiro-OMeTAD based HTL solution that is made up of 80 mg Spiro-OMeTAD, 17.7μL LiTFSI-acetonitrile solution (520mg/mL LiTFSI in acetonitrile) and 28.8uL tBP in 1mL chlorobenzene.[18] In HTL, LiTFSI normally functions as the p-dopant, which improves the hole conductivity of this layer;[56,96] whereas tBP enhances the hole extraction on perovskite/HTL interface.[60,141,142]

Though PSCs have high energy conversion efficiency and low manufacture cost, the low device stability limits its further application and commercialization. Firstly, the perovskite intrinsic layer is moisture sensitive. The perovskite materials can degrade their precursors under exposure to moisture.[50,57,143] On the other hand, the ETL and HTL in PSCs reduce the device stability: In ETL, TiO_2 may cause the perovskite to decompose in exposure to UV light and oxygen.[122,144] Other organic electron-transport materials such as Phenyl-C61-Butyric-Acid-Methyl Ester (PCBM) are also oxygen sensitive.[64] As shown in our previous work, in HTL, the negative effects for the device stability are mainly from the additives LiTFSI and tBP. The LiTFSI is hygroscopic which can adsorb water and turns into liquid in seconds. tBP, as the only liquid components in PSCs, can gradually evaporate at room-temperature though its boiling point is 197 ℃.[60] Moreover, tBP is corrosive to the intrinsic layer by dissolving perovskite materials.[145] These additives in HTL further reduce the stability of PSCs. Several alternative additives with

improved stability in PSCs had been reported.[146,147] However, either with the lower power conversion efficiency or higher price, these additives are not suitable to substitute LiTFSI and tBP.

On the other hand, when LiTFSI and tBP co-exist in PSCs, their individual negative effects on PSCs are limited. Previous studies show that the hygroscopicity of HTL induced by LiTFSI decreases when tBP exists.[60] Also, tBP controls the morphology of HTL by assisting in uniform distribution of LiTFSI in the bulk HTL solution.[56,142] Both positive and negative effects among the HTL components and perovskite are shown in Figure 7.1 (A). The mechanism on why tBP improves the LiTFSI distribution in HTL has not been clarified yet. The most commonly applied tBP:LiTFSI molar ratio in PSCs HTL is around 6:1 (More detailed information see Table 7.1). To our knowledge, the 6:1 tBP:LiTFSI ratio in Spiro-OMeTAD HTL was first utilized in solid-state dye-sensitized solar cells (ss-DSSCs) since 2011.[89] Since then, this combination of HTL from ss-DSSCs with fixed molar ratio and components was introduced to PSCs in 2012, the year when PSCs started to develop as a new type of solar cells.[16,18] These first several PSCs works greatly influenced the following studies. As a result, the 6:1 tBP:LiTFSI was applied as the default ratio in PSCs field.

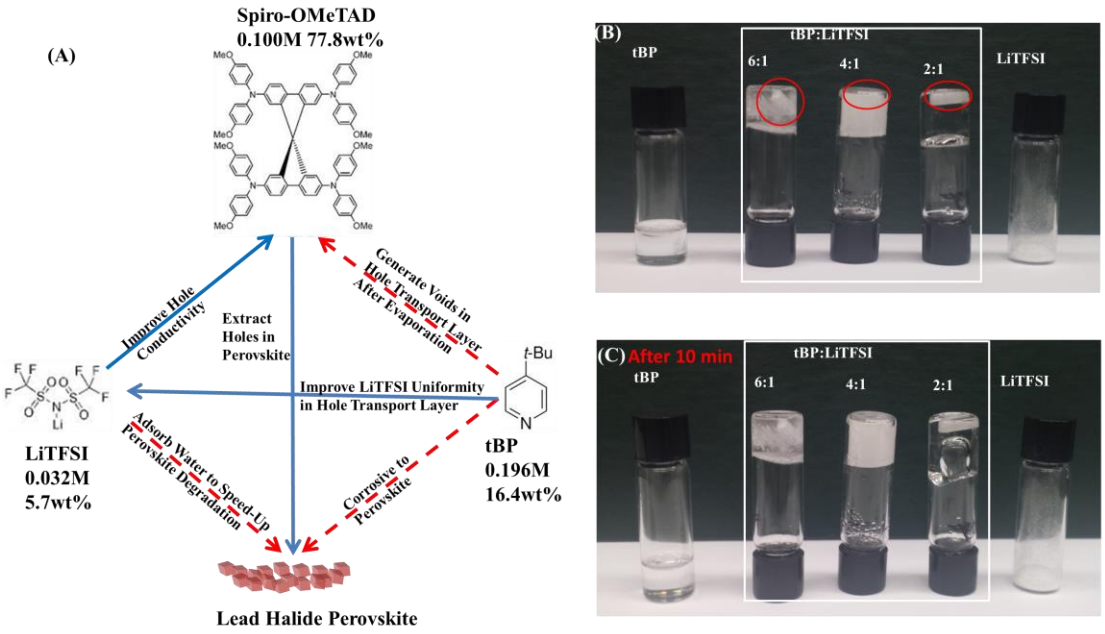

Figure 7.1 HTL components and optical images of tBP-LiTFSI mixtures at different molar ratios. (A) HTL components interactions between the components and perovskite (B) tBP-LiTFSI mixtures in vials placed upside down (stir bars in the vials were marked), and (C) after 10min.

Table 7.1 Summary on the tBP:LiTFSI ratio for perovskite solar cells in some reports

Perovskite Solar Cell Efficiency (%)	HTL Components	Molar ratio of tBP to LiTFSI	Reference
19.2%	Polytriarylamine (PTAA)/LiTFSI/tBP	6.15	*Science*. 2015. 348, 6240, 1234-1237.
19.7%	Spiro-OMeTAD/LiTFSI/tBP	6.20	*J. Am. Chem. Soc.* 2015. 137, 27, 8696-8699.
20.4%	Spiro-OMeTAD/LiTFSI/tBP	6.20	*Nature Energy*. 2016. 1, 16081.

Table 7.1 Summary on the tBP:LiTFSI ratio for perovskite solar cells in some reports (continued)

21.6%	Spiro-OMeTAD/LiTFSI/tBP	6.67	*Nature Energy*. 2016. 1, 16142.
21.6%	Spiro-OMeTAD/LiTFSI/tBP/ FK209	6.60	*Science*. 2016. 354, 6309, 206-209.
18.1%	Spiro-OMeTAD/LiTFSI/tBP/ FK209	6.60	*Adv. Mat*. 2017. 29, 15, 1606258.
18.15%	Spiro-OMeTAD/LiTFSI/tBP/ FK209	6.20	*Nano Energy*. 2017. 32, 414-421.
18.7%	Spiro-OMeTAD/LiTFSI/tBP	6.47	*ACS Energy Lett.* 2017. 2, 3, 622-628.
19%	Spiro-OMeTAD/LiTFSI/tBP/ FK209/acetic acid	6.74	*Adv. Energy Mat*. 2017. 7, 4, 1601451.
20.5%	Spiro-OMeTAD/LiTFSI/tBP/ FK209	6.60	*Science*. 2017. eaam5655
21.4%	Spiro-OMeTAD/LiTFSI/tBP	3.29	*Science*. 2017. 355, 6326, 722-726.
22.1%	PTAA/LiTFSI/tBP	6.15	*Science*. 2017. 356, 6345, 1376-1379.
18.5%	Spiro-OMeTAD/LiTFSI/tBP	6.05	*J. Phys. Chem. B.* 2018. 122, 2, 511-520.
19.12%	Spiro-OMeTAD/LiTFSI/tBP/ FK209	6.20	*Journ. of Power Sources*. 2018. 378, 483-490.
20.3%	Spiro-OMeTAD/LiTFSI/tBP/ FK209	6.60	*Energy Environ. Sci.* 2018. 11, 78-86.

Despite the prevalence of the 6:1 tBP:LiTFSI, it is unclear of whether or why this ratio is ideal in PSCs. Thus, understanding the reason that the negative effects of additives in HTL are

reduced when LiTFSI and tBP co-exist, can lead to an optimized tBP:LiTFSI ratio to improve the PSCs performance.

In this study, the formation of tBP-LiTFSI complexes at different molar ratios have been identified and characterized for the first time. On molecular level, the formation of tBP-LiTFSI complexes is based on the pyridine ring in tBP coordinates with lithium ion in LiTFSI. These complexes are more stable than individual LiTFSI and tBP in HTL. In these complexes, the evaporation speed of tBP has been slowed down and the corrosive effect of tBP on perovskite has been restricted. The hygroscopicity of LiTFSI in these complexes is limited compared to the individual LiTFSI. Moreover, the degradation speed of perovskite to its precursors and other products is hindered as well. Based on this study, in PSCs, the optimized tBP-LiTFSI molar ratio is 4:1, which shows better device stability, less hysteresis, and less variation in power conversion efficiency. The understanding of interactions between tBP and LiTFSI shows pathways to further enhance the PSCs performances.

7.2 Experimental Methods

All reagents, unless otherwise specified, were purchased from Sigma-Aldrich.

7.2.1 Synthesis of tBP-LiTFSI Complexes

The LiTFSI and tBP were mixed and sealed in vials at different molar ratios under inert gas condition. The tBP:LiTFSI molar ratios were 6:1, 4:1, and 2:1, respectively. All sealed samples were heated at 100 ℃ until they were homogenized and then cooled down to room temperature.

7.2.2 Preparation of Perovskite/tBP-LiTFSI Complex Films

Glass slides (1 cm^2) were cleaned by ultra-sonication in detergent water, deionized water, acetone, and isopropanol, sequentially for 15 min. Then the slides were treated with air plasma

for 10 min. The $CH_3NH_3PbI_3$ precursor was composed of equimolar (1.5 M) of CH_3NH_3I and PbI_2 in DMSO-DMF (1:9 volume ratio) solvent. Then the 1:30 volume ratio of CH_3NH_2-EtOH solution was added to the $CH_3NH_3PbI_3$ precursor solution. The solution was heated at 70 ℃ overnight before spin-coating. The films were spun with the precursor solutions on glass slides at 2000 r.p.m. for 25 s followed by 1 mL of ethyl ether drop-casted as the anti-solvent within 7s at 3000 r.p.m.[65] The films were annealed at 100 ℃ for 10 min. 0.032 M tBP-LiTFSI complexes in chlorobenzene at different molar ratios were spun on perovskite film at 3000 rpm for 30 s separately. This step was repeated three times on each sample to guarantee enough sample loading.

7.2.3 Perovskite Solar Cells (PSCs) Fabrication

The configuration of PSC was ITO Glass/SnO_2 compact layer/ perovskite layer/ Spiro-based HTL/Au. The perovskite precursor solution is the same as mentioned in the previous section which includes excessive about of methyl amine (1:30 volume ratio to DMF). More detailed information for other layers can be found in the reference. [65] The devices were fabricated in fume hood at ambient condition.

7.2.4 Characterization

Fourier transform infrared spectroscopy (FTIR) with attenuated total reflectance (ATR) attachment (Nicolet 6700 with Smart-iTR) was applied for the FTIR test. Samples for FTIR were tested at ambient condition.

Environmental Scanning Electronic Microscopy (ESEM) images were taken with a FEI/Philips XL30 ESEM operated at 15 kV. Water vapor (with a pressure of 1.1 Torr) was purged in the chamber to characterize the morphological evolutions of the samples *in-situ*. To

minimize the beam-induced effect, the beam was only turned on while the images were taken. Images were taken every 10 min.

Optical Micrographs were taken with a VHX-1000 microscope at ambient condition every 5 min.

X-ray photoelectron spectroscopy (XPS) was performed using a Kratos AXIS Supra with Al Kα anode source operated at 15 kV and 10^{-8} Torr chamber pressure. Spectra data were calibrated with the hydrocarbon C1s peak (284.8 eV) and processed by CasaXPS.

Transmission electron microscopy (TEM) images were taken with a JEOL 2100 200 kV Microscope. Samples for TEM were prepared by focused ion beam (FEI Scios DualBeam FIB/SEM). The FIB-TEM sample preparation procedure is the same as the reference.[60]

The performances of PSCs were tested with a solar simulator with a 150 W xenon lamp (Solar Light SL07265, equipped with an AM1.5G filter, calibrated with a standard Si solar cell to simulate AM1.5 illumination (100 mW cm^{-2})) and a Keithley 2400 source meter.

7.3 Results and Discussion

7.3.1 Formation of tPB-LiTFSI Complexes

To identify the formation of tBP-LiTFSI complexes, tBP and LiTFSI at various molar ratios were mixed together (For the molecular structures of tBP and LiTFSI, see Figure 7.1(A)). At room temperature, tBP is liquid while LiTFSI is solid state. It was observed that 2:1 is the lowest tBP to LiTFSI molar ratio at which a homogenized mixture can be obtained. In 1:1 tBP-LiTFSI mixture, LiTFSI cannot be fully dissolved in tBP. Most publications that used tBP-LiTFSI as the HTL additives, 6:1 was adopted as the tBP: LiTFSI ratio. Thus, the molar ratio for

tBP: LiTFSI in this work focuses on the range from 6:1 to 2:1. As shown below, the 6:1, 4:1 and 2:1 mixtures have some distinguishable physical properties.

The three tBP-LiTFSI mixtures have distinguishable appearances: the 6:1 mixture forms a gel (with extra liquid), the 4:1 mixture is wax-like (without excess amount of "free" liquid) while the 2:1 mixture forms a viscous liquid. Figure 7.1(B) displays these tBP-LiTFSI mixtures synthesized in black-lid glass vials with stir bars. All of the mixtures can be placed upside down to hold the stir bars. After 10 min, in Figure 7.1(C), no change had been observed for the 6:1 and 4:1 mixtures. However, the shape of 2:1 mixture changed which indicated a viscous flow-like behavior of tBP-LiTFSI mixture at the molar ratio of 2:1. Intuitively, if the solid salt and liquid organics can be homogenously mixed with little intermolecular interactions, it would either form a solution or quasi-solid state gel. However, only the 6:1 mixture meets this expectation. By decreasing the tBP-LiTFSI ratio to 4:1, the wax-like material was obtained. This sample can be placed on weighing paper without wetting the paper as shown in Figure 7.2 (A). A further decrease in the tBP content to 2:1 (tBP-LiTFSI mixture) displayed a flow-like behavior, which was confirmed in Figure 7.2 (B). The mixture was loaded on a metal tip and a continuous stream is seen between the tip and stage. Among these mixtures, the 2:1 sample has the highest LiTFSI content which inherits its solid-state like behavior. However, unlike the 6:1 and 4:1 samples, it appears to be transparent liquid. This abnormal phenomenon was observed in urea-LiTFSI mixtures as well,[148] which can be attributed to the molar ratio of 2:1 is the eutectic ratio of the tBP-LiTFSI mixtures at room temperature.

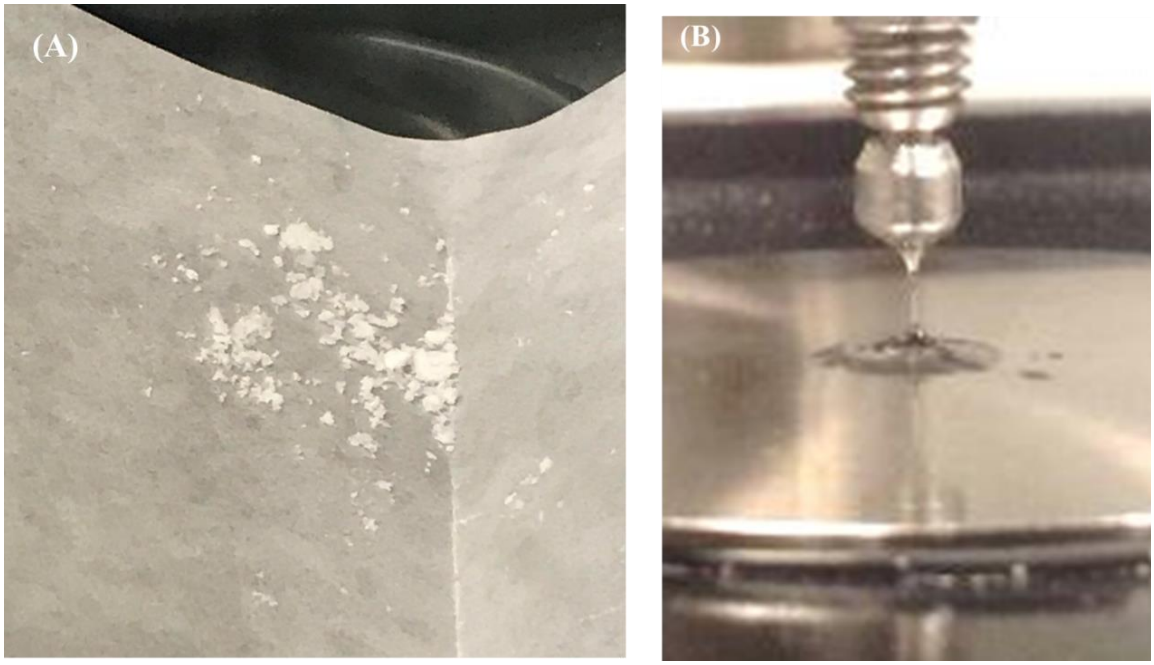

Figure7.2 Optical Images of tBP-LiTFSI mixtures at different molar ratios. (A) Wax-like 4:1 molar ratio tBP-LiTFSI mixtures on weighing paper. (B) Viscous liquid-like 2:1 molar ratio tBP-LiTFSI mixture flows between the tip and stage.

Fourier-transform infrared spectroscopy (FTIR) was also applied to characterize the formation of tBP-LiTFSI complexes since all of the mixtures are amorphous organics. Figure 7.3 (A) is the full-range tBP FTIR. The pyridine ring stretching mode peak at ~1596 cm^{-1} in Figure 7.3 (A) was labelled and selected to conduct the further data analysis. The reason for focusing on this ring mode peak was that it is very sensitive to changes of conjugated π electronic orbitals of tBP upon formation of different complexes.

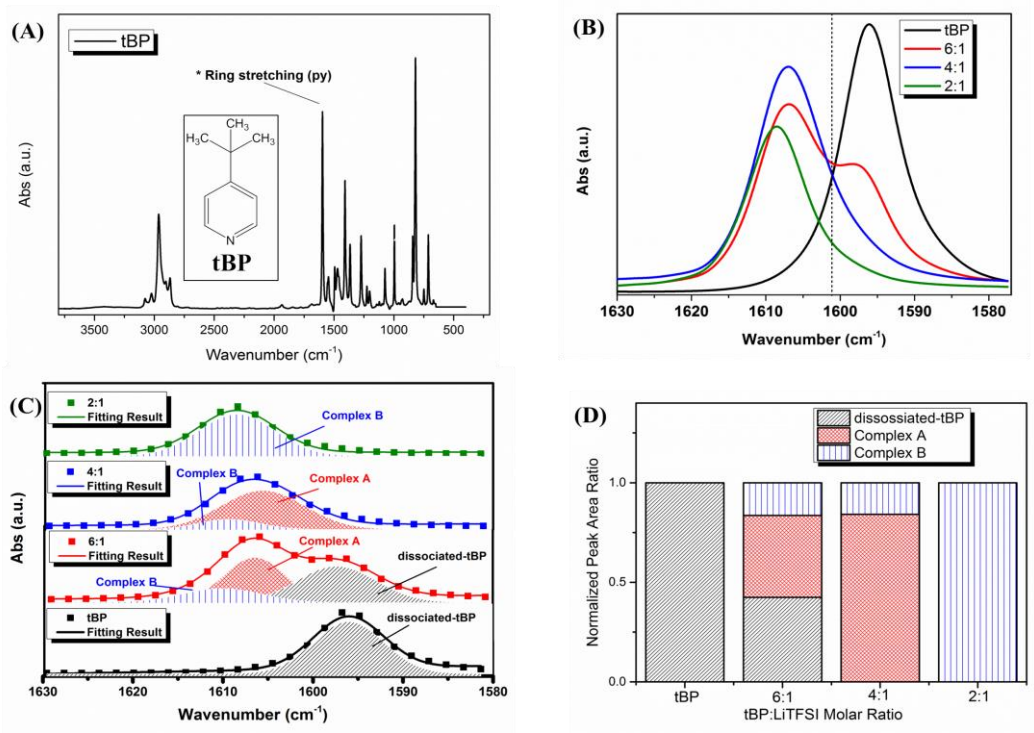

Figure 7.3 FTIR of (A) tBP with ring stretching mode peak at 1596 cm^{-1} labelled in the figure, (B) the ring stretching mode peaks for tBP and tBP-LiTFSI mixtures at different molar ratios, (C) the fitting for the FTIR peaks of (B), and (D) the normalized peak area ratio derived from (C).

Furthermore, the ring mode is strong and far away from vibrational modes of LiTFSI and other modes of tBP, which provides the best observation window for this study (for the tBP FTIR with all labelled peaks see Figure 7.4).

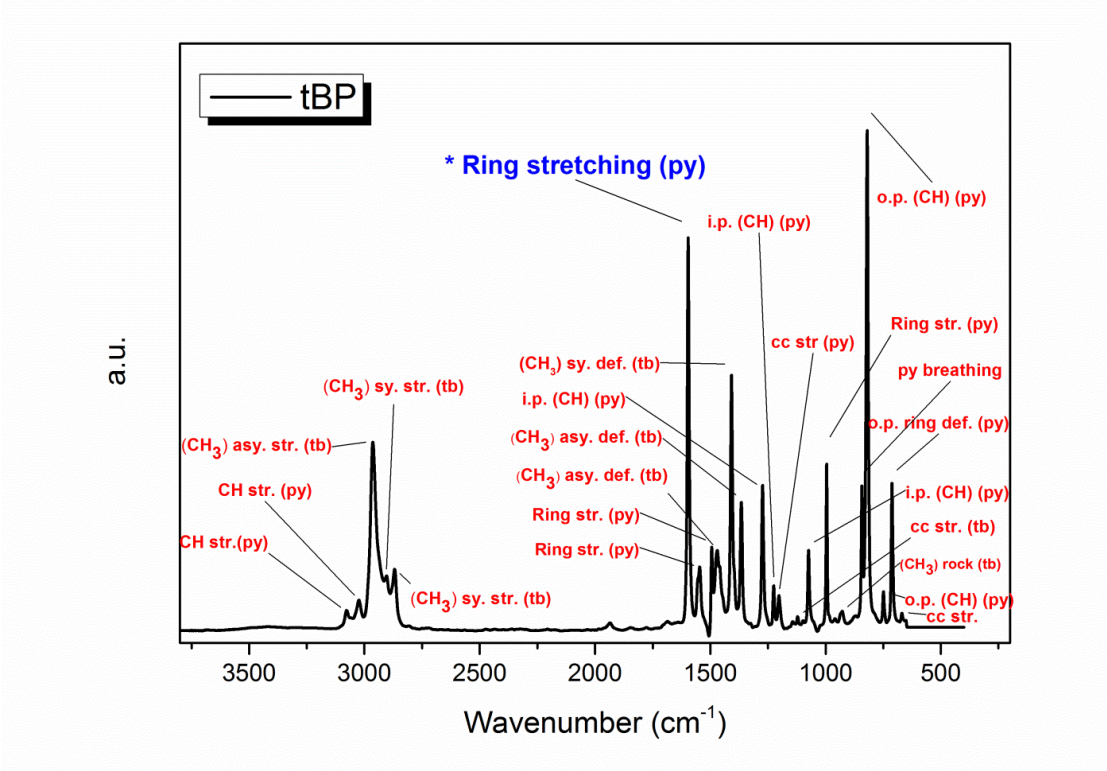

Figure 7.4 Fourier-transform infrared spectroscopy (FTIR) of tBP with all labelled peaks, the peaks labelling is according to reference[149]

As shown in Figure 7.3(B), the ring stretching mode peaks for tBP and tBP-LiTFSI mixtures at different molar ratios displayed different peak shapes and positions. Pure tBP only has a single peak in this region so does the 4:1 and 2:1 tBP-LiTFSI mixtures. However, both of the 4:1 and 2:1 peaks have a blue shift. On the other hand, the spectrum of the 6:1 tBP-LiTFSI mixture shows two peaks, one close to the blue-shifted peak observed in the 4:1 and 2:1 ratio mixtures, whereas a shoulder peak appears near the peak of pure tBP liquid. (More FTIR results were collected for the tBP-LiTFSI mixtures which molar ratios are between 1:1 and 1:10, see Figure 7.5.)

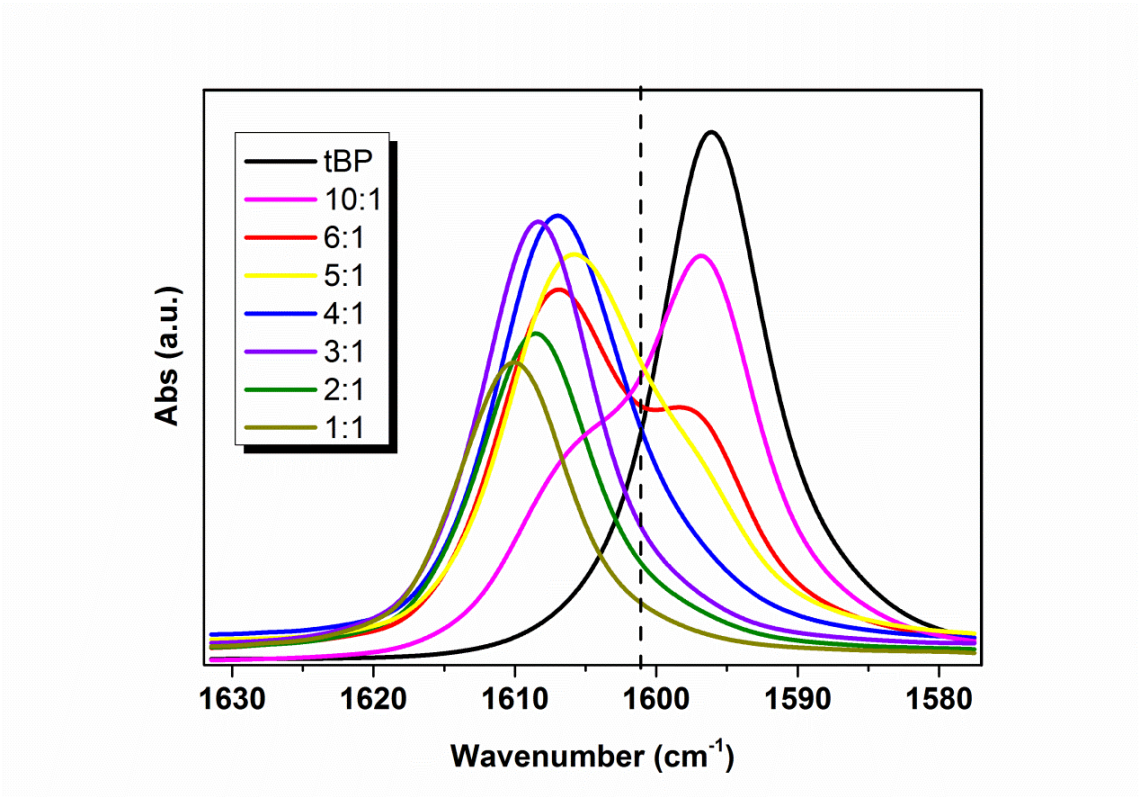

Figure 7.5 FTIR of the pyridine ring stretching peaks for tBP and tBP-LiTFSI mixtures at different molar ratios (with more mixtures besides the tBP:LiTFSI at 6:1, 4:1 and 2:1 mole ratio).

Compared with pure tBP, a clear trend was observed: With more LiTFSI added into tBP, the peak at 1596 cm^{-1} was reduced. At the same time, the peak on blue-shift region gradually converted into a single peak without any shoulder signal.

Previous literature shows that the nitrogen of pyridine ring can coordinate with metal ions. After donating the lone electron pair, the electronegativity of nitrogen in the pyridine ring is impaired and the aromatic property of pyridine ring is enhanced. As a result, the bond strength of pyridine ring is enhanced and thus the blue-shift in FTIR is observed.[149] Since tBP has a pyridine ring, which can coordinate with Li ion of LiTFSI, the blue-shift of the mixtures in Figure 7.3(B) can be explained by the formation of tBP-LiTFSI complex.

In Figure 7.3(B), the position of the shoulder of the 6:1 mixture matches to the peak position of pure tBP while the major peak position of the 6:1 mixture is close to the peak of the 4:1 mixture. This result explains why in Figure 7.1(B) and (C) the 6:1 mixture has a gel-like appearance: The extra liquid component is the tBP that does not form complex while the solid component forms the tBP-LiTFSI complex. In this case, a dash line was drawn to separate Figure 7.3 (B) into two parts: The right side of the dash line is the un-complexed tBP region and the left side is the complexed tBP region.

To further identify which complexes exist in these mixtures, the FTIR in Figure 7.3(B) was fitted as displayed in Figure 7.3(C). Three Gaussian peaks (1596 cm^{-1}, 1606 cm^{-1} and 1610 cm^{-1}) were applied for fitting. The fitting results are corroborated by the experimental data. The ratio of the mixtures in the fitting peaks area is shown in Figure 7.3(D). The 1596 cm^{-1} peak corresponds to the un-complexed tBP since it coincides with the pure tBP peak. The 1606 cm^{-1} and 1610 cm^{-1} peaks reflect two tBP-LiTFSI complexes. The 1606cm^{-1} peak is termed as Complex A and the 1610 cm^{-1} peak is termed as Complex B and their compositions are discussed in the following paragraph. In Figure 7.3(C), Complex A, Complex B and un-complexed tBP co-exist in the 6:1 mixture. There is only complexed tBP in the 4:1 mixture. Complex A is the dominant part in this mixture with small amount of Complex B. For the 2:1 mixture, only complex B was observed.

The tBP:LiTFSI mole ratios in complex A and B were calculated based on the peak area ratio as shown in Figure 7.3(D). It was found that in complex A, the molar ratio of tBP:LiTFSI is close to 4:1 (the calculated result is 3.7:1) while in complex B is 2:1. However, pure complex A cannot be obtained in the 4:1 mixture, although it is the dominant part in the sample. This can be attributed to chemical equilibrium exists within a series of tBP-LiTFSI intermediate complex in

the 4:1 mixture. Thus, spectroscopic study suggests that tBP and LiTFSI form different chemical complex at different mixing ratio. The next question is how complexation is related to alleviating the negative effect of tBP-LiTFSI in PSCs.

7.3.2 Evaporation and Hygroscopicity of tPB-LiTFSI Complexes

Our previous research demonstrated that the tBP evaporation and LiTFSI hygroscopicity further reduces the stability of PSCs[60]: Several bubble-like voids were seen across the HTL due to the tBP evaporation, which enables new sites to accumulate moisture. Meanwhile, the hygroscopicity of LiTFSI also increases the moisture level in HTL. The accumulated water in HTL due to the combined effects of tBP evaporation and LiTFSI hygroscopicity causes the perovskite intrinsic layer degradation.

The weight changes of tBP-LiTFSI mixtures were measured to evaluate their evaporation behavior and hygroscopicity. Each sample was weighed at intervals of 10 min for 180 min in a glovebox (argon gas environment) and an ambient fume hood separately. The results are shown in Figure 7.6(A) and (B).

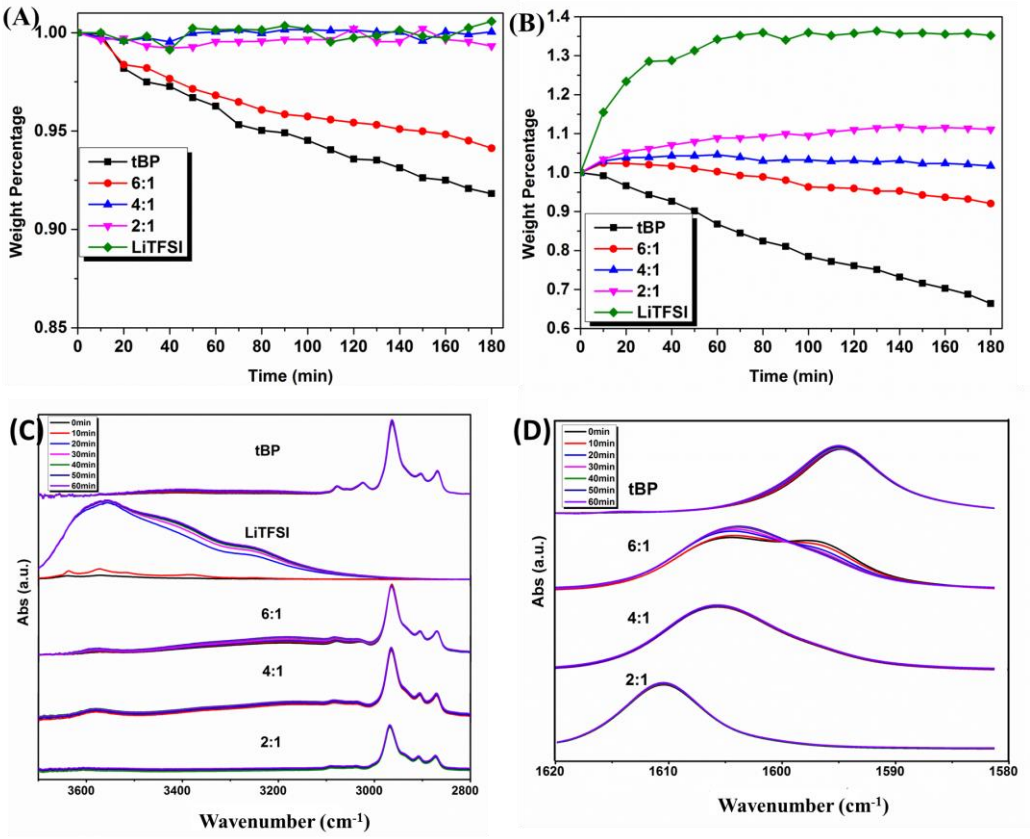

Figure 7.6 Evaporation and hygroscopicity of tBP, LiTFSI, and tBP-LiTFSI mixtures: Normalized Weight percentage change within 180 min in (A) glove box (argon gas environment) and (B) ambient fume hood. FTIR of samples in an ambient condition within 60 min at: (C) –OH association peak region; (D) pyridine ring stretching region.

The hygroscopicity from LiTFSI can increase the average weight while the tBP evaporation can decrease it. Figure 7.6 (A) displays the normalized weight percentage change of the samples in the glove box. In the inert gas environment, the water level is low enough (<0.1ppm) to limit the hygroscopicity effect. Since no obvious weight change was observed for the LiTFSI sample for three hours according to Figure 7.6(A), the tBP evaporation should be the dominant reason to cause the sample weights to change in the glove box. A significant weight

loss is seen in the tBP sample (black curve Figure 7.6(A)). In the meantime, there is no weight loss for the 4:1 and 2:1 mixtures, which indicates that the formation of tBP-LiTFSI complex (A and B) can prevent tBP from evaporating. On the contrary, a weight loss in the 6:1 mixture was observed, albeit lower than tBP itself. This agrees with the FITR result that the 6:1 mixture has un-complexed tBP, which can evaporate.

As shown in Figure 7.6(B), both of the pure tBP evaporation (weight loss) and LiTFSI hygroscopicity (weight gain) co-exist in an ambient condition. It is noted that the pure tBP evaporates faster in ambient condition than in glove box, which could be attributed to the higher gas flow rate in a fume hood. The weight percentage of pure LiTFSI increased over 35% for 3 hours due to its hygroscopicity. The weight gain of the tBP-LiTFSI mixtures did not increase as much as pure LiTFSI.

It could be the tBP components that decreased the molar percentage of un-complexed LiTFSI. However, even after considering this factor as shown in Table 7.2, the hygroscopicity of LiTFSI in these mixtures are still limited. Hence we propose that the formation of tBP-LiTFSI complexes reduced the hygroscopicity of LiTFSI.

Table 7.2 Weight Percentage Changes of tBP, LiTFSI and tBP-LiTFSI Mixtures after 3 Hours

tBP-LiTFSI Molar Ratio	LiTFSI Weight Percentage	Weight Percentage after 3hours	Weight Percentage Difference	LiTFSI Component Hygroscopicity **
6 to 1	26.14%	92.05%	-7.95%	0%
4 to 1	34.67%	101.73%	1.73%	4.99%
2 to 1	51.49%	111.10%	11.10%	21.56%
LiTFSI	100.00%	135.20%	35.20%	35.20%

* Weight Percentage Difference: The difference between the weight after 3 hours and the weight of the very beginning.

** LiTFSI Component Hygroscopicity = [(Weight Percentage Difference) / (LiTFSI Weight Percentage)] * 100%

To investigate the evaporation and hygroscopicity of tBP-LiTFSI mixtures, FTIR was measured for all mixtures at various exposure times (within 1 hour) in an ambient condition as shown in Figure 7.6(C) and (D). Figure 7.6 (C) displays the -OH stretch peak region (~3000 cm^{-1} to 3700 cm^{-1}), which indicates that the samples absorbed water. There is a huge difference for LiTFSI in this region before and after the exposure for 1 hour in an ambient condition. It shows that LiTFSI has strong hygroscopicity as discussed before. Two –OH stretching peaks appear at the first 10 min LiTFSI FTIR in Figure 7.6(C): 3678cm^{-1} is corresponding to LiOH while 3574cm^{-1} is $LiOH \cdot H_2O$.[150] Then these two peaks were covered by a broaden peak from water later. Previous literature[151] shows that HTFSI, the conjugate acid of LiTFSI has super hygroscopicity and deliquescence. It means that the hydration of LiTFSI involves two steps: The Li^+ reacts with water to form LiOH first and then the formation of HTFSI leads to more water adsorption. In contrast, for tBP and all three tBP-LiTFSI mixtures in Figure 7.6(C), there is no obvious OH stretch peak here. This proves that the tBP-LiTFSI complexes mitigate the hygroscopicity of LiTFSI. According to Figure 7.3 and Figure 7.6, in molecular level, it is clear to conclude that the coordination of pyridine ring (tBP) with lithium ion (LiTFSI) prohibits the formation of LiOH and HTFSI which mitigates the LiTFSI hygroscopicity.

Unlike the transmission mode FTIR where samples need to be dispersed in KBr, no pre-treatment was done for the Attenuated Total Reflectance FTIR sample. As a result, the concentration of tBP is 100% no matter how much it evaporates. There is no obvious change of the FTIR for the 4:1 and 2:1 samples in this range either. The unchanged peaks for the 4:1 and 2:1 mixtures agree with the weight loss measurements that LiTFSI prevents the tBP from evaporating, because there is no un-complexed tBP in these two samples. The limited tBP evaporation in tBP-LiTFSI can also be attributed to the coordination of pyridine ring with lithium ion. Thus, a synergistic effect occurs when LiTFSI and tBP are mixed and allow each other to mitigate the negative effect.

This conclusion is supported by the FTIR ring modes of the 6:1 mixture in which a peak change was observed. The 'shoulder' of the 6:1 mixture FTIR peak at 1596 cm^{-1} wavenumber gradually decreased. In an hour, this peak changed from a shoulder peak to a single peak. As discussed in Figure 7.3, the 'shoulder' for this peak is attributed to the un-complexed tBP. Therefore, the disappearance of the 'shoulder' in the 6:1 mixture pyridine ring stretching peak reflects the evaporation of un-complexed tBP. Interestingly, an increase of the peak intensity at ~1606 cm^{-1} wavenumber was observed. This is because after the tBP evaporated, the concentration of tBP-LiTFSI complex in the 6:1 mixture improved. The coordination of pyridine ring with lithium ion shows huge impacts on the properties of the tBP-LiTFSI mixtures. As a result, the formation of tBP-LiTFSI complexes limits the tBP evaporation and LiTFSI hygroscopicity. It is important to characterize whether this phenomenon can enhance the stability of perovskite layer.

7.3.3 Interaction of tBP-LiTFSI Complexes to Perovskite

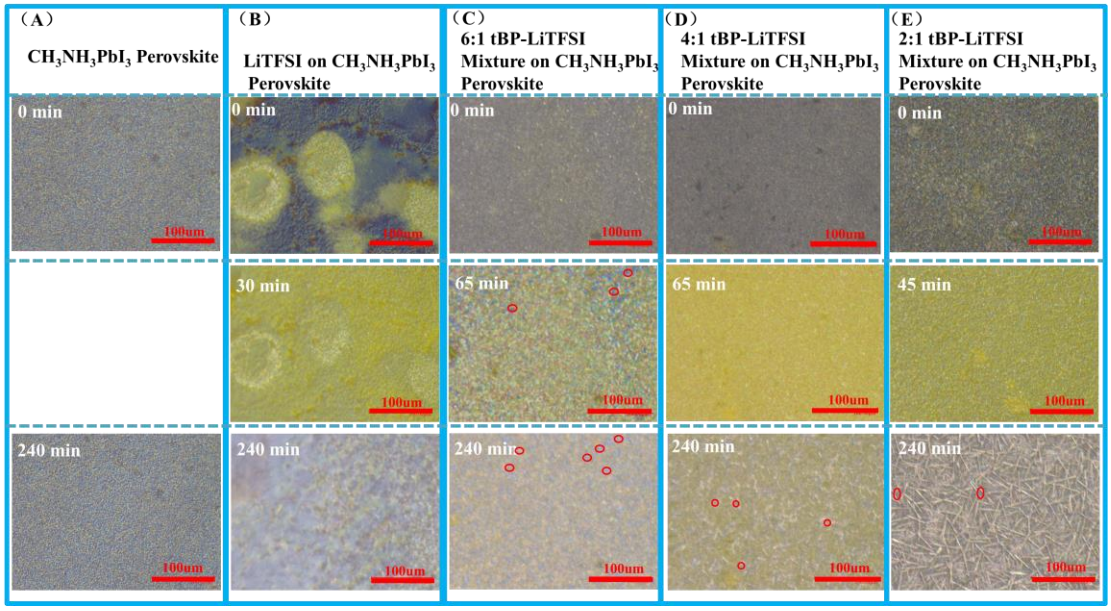

Figure 7.7 Optical micrographs of perovskite films exposed for 4 h in an ambient condition, which were spun with (A) Nothing, (B) LiTFSI, (C) 6:1 tBP-LiTFSI, (D) 4:1 tBP-LiTFSI, and (E) 2:1 tBP-LiTFSI. Some of the blue-colored regions were marked with red circles.

To investigate the influences of tBP-LiTFSI complexes on a perovskite layer, LiTFSI and the tBP-LiTFSI mixtures at different molar ratios were spun on perovskite films separately. Each sample was observed by optical microscope in an ambient condition for 240 min. Figure 7.7 displays the optical micrographs for $CH_3NH_3PbI_3$ films with/without HTL additives. Three representative rows are shown in Figure 7.7. Row 1 was the starting time for all freshly prepared samples. Row 2 was the time when all the dark brown regions (indicative of perovskite) disappear from the samples. It can be considered as the complete degradation from perovskite to PbI_2.[75] Row 3 was the images for all the samples at 240 min.

As shown in Figure 7.7(A), no obvious morphological change was observed within 240 min for the perovskite sample without any HTL additives. However, in Figure 7.7(B), after

depositing LiTFSI, the perovskite started to degrade right after finishing spin-coating (0 min) as shown in Figure 7.7(B). After 30 min, the perovskite film was degraded completely. Moreover, further degradation was observed which was colorless and dendrite morphology after 240 min. The dendrite morphology for Figure 7.7(B) was observed when zoomed at a larger scale. (See Figure 7.8.)

Figure 7.8 Large scale optical micrograph of $CH_3NH_3PbI_3$ perovskite film exposure for 4 hours in ambient condition spun with LiTFSI

According to Row 2 in Figure 7.7(C) to (E), when the perovskite layer is coated with tBP-LiTFSI mixtures, its degradation slowed down compared with the layer that was coated with only LiTFSI. The perovskite degradation time window for samples coated with the 6:1 and 4:1 tBP-LiTFSI mixtures were 65 min. The same time window for the 2:1 tBP-LiTFSI mixture sample was 45 min. Compared with the LiTFSI coated sample where the time window was 30

min, introduction of tBP improved the stability of perovskite. Moreover, samples which were coated with the 6:1 and 4:1 mixtures have longer time window than the 2:1 sample. This indicates that the hygroscopicity of Complex A is less than Complex B. The hygroscopicity difference between Complex A and B was not observed in spectroscopy measurement (Figure 7.6), but was elucidated from optical micrographs (Figure 7.7). This can be attributed to the fact that perovskite can react to a little amount of water and lead to degrade.

It is also seen that further degradation existed in Row 3 of Figure 7.7 (C) to (E). After the perovskite film (dark brown) has converted to PbI_2 (yellow), colorless dendrites were formed. According to Figure 7.7(B) (perovskite with LiTFSI), the dendrite is too large for the existing magnification of the electron microscope, hence a lower magnification is used. The size of dendrites in this sample is over 100 um (Figure 7.8). In Figure 4(E), with the 2:1 mixture, the dendrites were reduced to ~30 um. With the 6:1 and 4:1 mixtures, as shown in Figure 7.7(C) and (D), the dendrite size was more reduced to 10 um. This trend indicates that the formation of tBP-LiTFSI complexes not only slows down the degradation from perovskite to PbI_2, but also restricts the formation of degradation product(s).

Moreover, from Figure 7.7 (C) to (E), some blue-colored regions showed up which were from the substrate (marked by red circles in Figure 7.7 (C) to (E)). The samples with less coverage on the substrate showed clear evidence that the blue regions were from the substrate (see Figure 7.9).

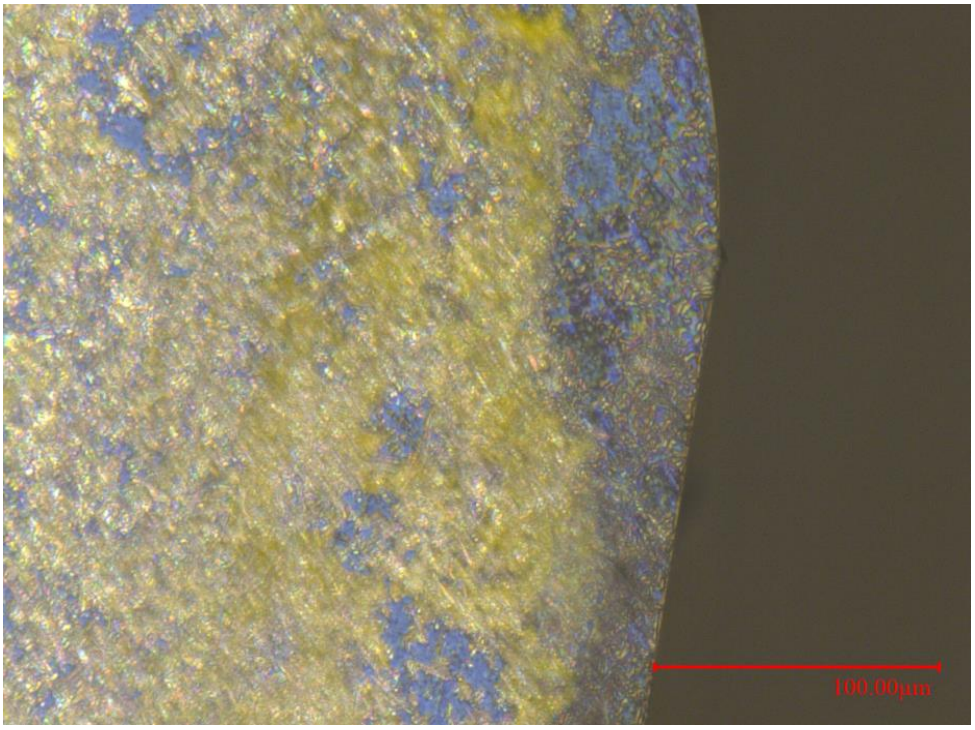

Figure 7.9 Optical micrograph of degraded perovskite film with less sample coverage shows more substrate area

This can be attributed to the corrosive effect of tBP to perovskite and the degradation products.[145] In Figure 7.7 Row 3, more blue regions were observed in Figure 7.7(C) than (D) and (E), which supports that the existence of un-complexed tBP in the 6:1 mixture has a more corrosive effect compared with the pure tBP-LiTFSI complexes. The optical micrograph results indicate that the 4:1 mixture maintains an optimal complex composition. This ratio prevents tBP from evaporating to induce corrosive effect, and on the other hand, such ratio mixture reduces water uptake because Li^+ has been tightly surrounded by tBP to limit the formation of HTFSI to adsorb water.

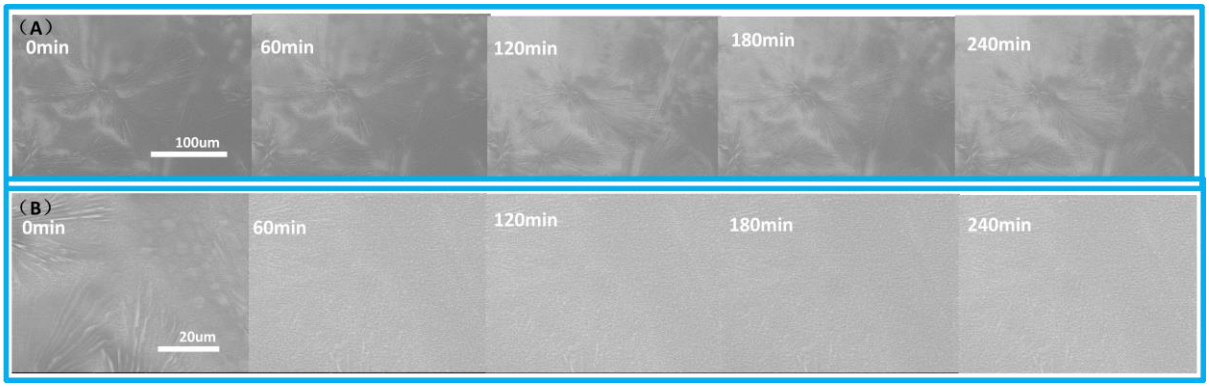

Figure 7.10 Environmental Scanning Electron Microscope (ESEM) Image of $CH_3NH_3PbI_3$ perovskite films with LiTFSI under 1.1Torr water vapor pressure for 240 min at (A) large scale and (B) small scale

Light, moisture or oxygen can be the possible factor(s) to cause the dendrite structures to form in an ambient condition. To understand which one was the main factor for the dendrite formation, Environmental Scanning Electron Microscope (ESEM) was applied. In ESEM, sample was placed in a high vacuum chamber in the dark condition, thus the influences of oxygen and light were ruled out. As shown in Figure 7.10(A), the dendrite formation still can be observed in the perovskite film with LiTFSI for 240 min. It means that the moisture can be the primary reason to cause the degradation of the perovskite. It is also possible that electron beam in ESEM may cause the dendrite formation. However, at a higher magnification as shown in Figure 7.10(B), the dendrites start to disappear. This means that the electron beam could not have caused the dendrite formation, but the beam actually hindered the dendrite from growing. Based on these phenomena, moisture could be the only reason to cause the perovskite to degrade more.

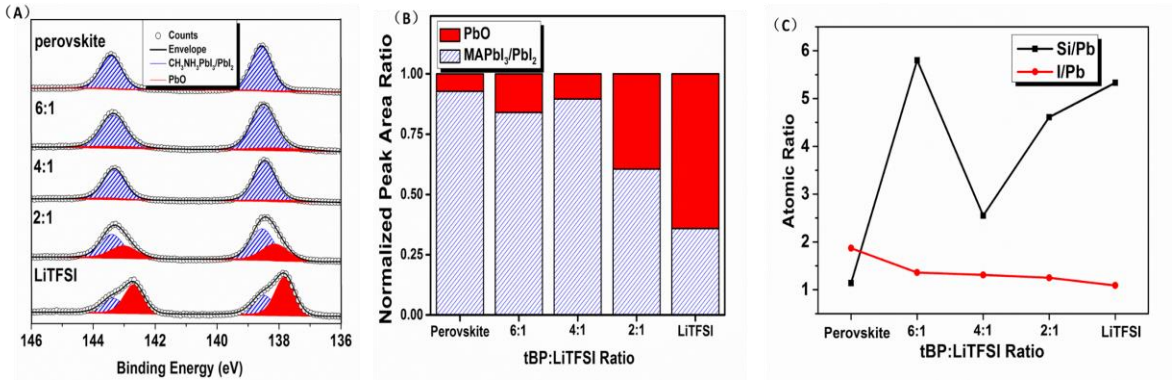

Figure 7.11 XPS of perovskite in an ambient condition over night which was spun with nothing, LiTFSI, 6:1, 4:1 and 2:1 molar ratio tBP-LiTFSI mixtures, separately. (A)Pb 4f; (B) the peak area ratio for PbO to $MAPbI_3/PbI_2$; and (C) Atomic ratio of Si to Pb and I to Pb derived from XPS (For full XPS, see Figure 7.12).

X-Ray Photoelectron Spectroscopy (XPS) was applied to investigate the degradation product(s) (For full XPS spectra, see Figure 7.12). The chemical analysis from XPS could further support the dual-effect of tBP-LiTFSI on reducing both water uptake and corrosion. Figure 7.11(A) displays the Pb 4f peaks for the perovskite samples spun with HTL additives, which are kept in an ambient condition overnight. Previous study shows that the Pb 4f peaks for PbI_2 and $CH_3NH_3PbI_3$ are too close to distinguish. [51] There are two pairs of peaks which are considered to get the good fitting results: 138.5 eV and 143.4 eV; corresponding to the $4f_{7/2}$ and $4f_{5/2}$ peaks of $CH_3NH_3PbI_3/PbI_2$, respectively. Another pair is the 137.8eV and 142.7 eV peaks, which are the $4f_{7/2}$ and $4f_{5/2}$ peaks for PbO, respectively.[51]

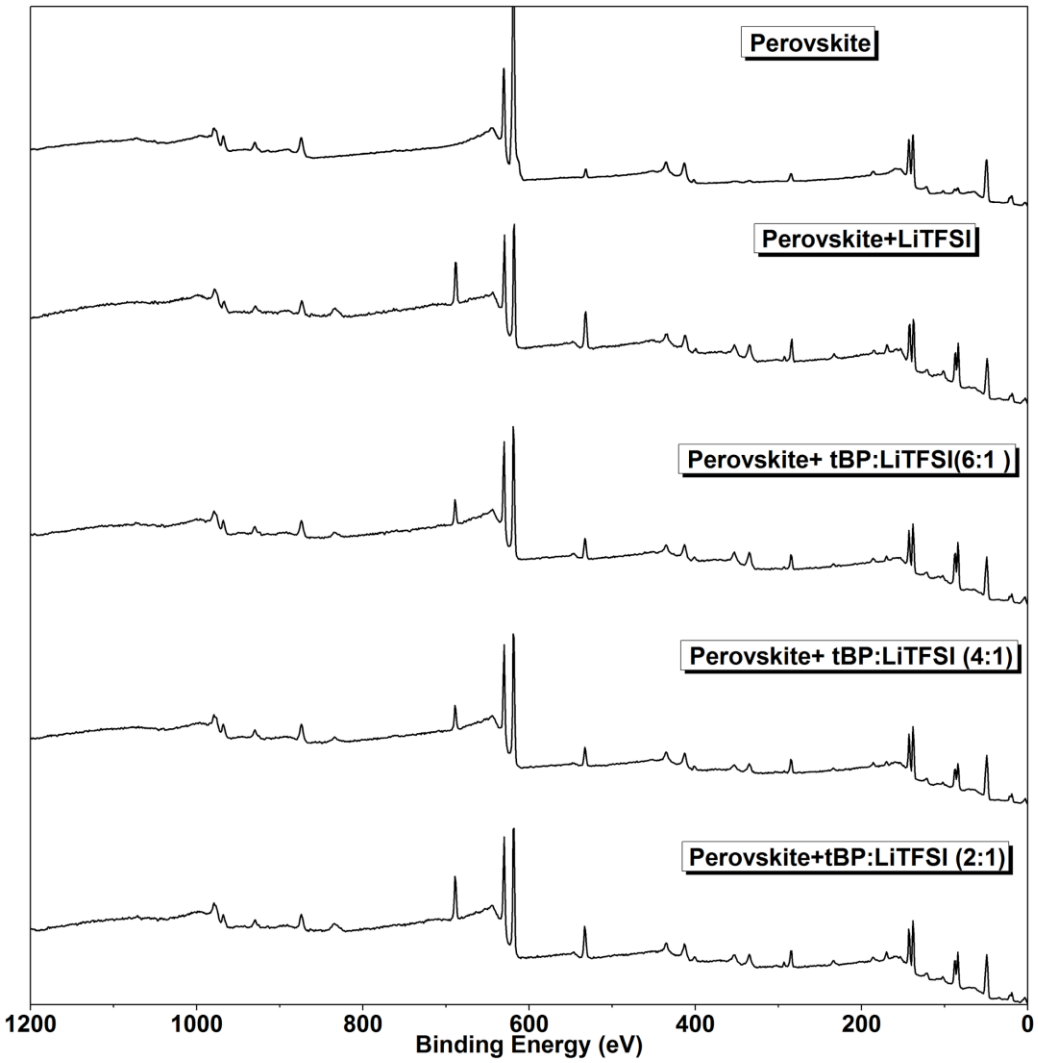

Figure 7.12 X-Ray Photoelectron Spectra (XPS) of $CH_3NH_3PbI_3$ perovskite films in ambient condition over night which were spun with nothing, LiTFSI, 6:1, 4:1 and 2:1 molar ratio tBP-LiTFSI mixtures, separately.

It is likely that the dendrites in Figure 7.7 and 7.10 were from PbO. Figure 7.11(B) shows the ratio of PbO to $CH_3NH_3PbI_3/PbI_2$ according to Figure 7.11(A). In this Figure, the perovskite film with LiTFSI has the highest amount of PbO. By introducing tBP, the amount of PbO reduced. The film with LiTFSI has 64% PbO, which reduced to 39% for the sample with the 2:1

tBP-LiTFSI mixture. It was further reduced to 10% and 16% for the 4:1 and 6:1 tBP-LiTFSI samples, respectively. Interestingly, the sample with the 6:1 tBP-LiTFSI mixture has higher PbO than the one with the 4:1 mixture even though the 6:1 has more tBP. This can be attributed to the un-complexed tBP in 6:1 sample, which dissolves $CH_3NH_3PbI_3/PbI_2$ that reduces the ratio of this component. These subsequent degradation products can make the recycling of perovskite materials more difficult: Both PbI_2 and $CH_3NH_3PbI_3$ can be recycled by polar aprotic solvents such as DMF[52] while PbO cannot be recycled as easily. The formation of tBP-LiTFSI complexes can slow down the formation of PbO, which makes the recycling of perovskite easier. According to XPS spectra, as shown in Figure 7.11(C), the samples' atomic ratio of Si:Pb and I:Pb can be obtained. The ratio of I:Pb is considered as the index for the perovskite degradation, because for perovskite, this ratio is 3, 2 for PbI_2 while for PbO its 0. It shows that with the increased amount of tBP, the samples have higher I:Pb ratio than the perovskite film coated with pure LiTFSI. On the other hand, a silicon signal occurs in the substrate, therefore the Si:Pb ratio can be considered as the index for corrosive effects. It is either attributed to the tBP dissolving perovskite/PbI_2 or degradation. In this case, among the perovskite samples, which were spun with different ratio of HTL additives, the 4:1 tBP-LiTFSI sample shows the lowest Si:Pb ratio. It is because this ratio does not contain the un-complexed tBP compared with the 6:1 tBP-LiTFSI mixture. At the same time, it has less hygroscopicity compared with the 2:1 tBP-LiTFSI mixture.

7.3.4 Influences of tBP-LiTFSI Complexes on Perovskite Solar Cell Performance

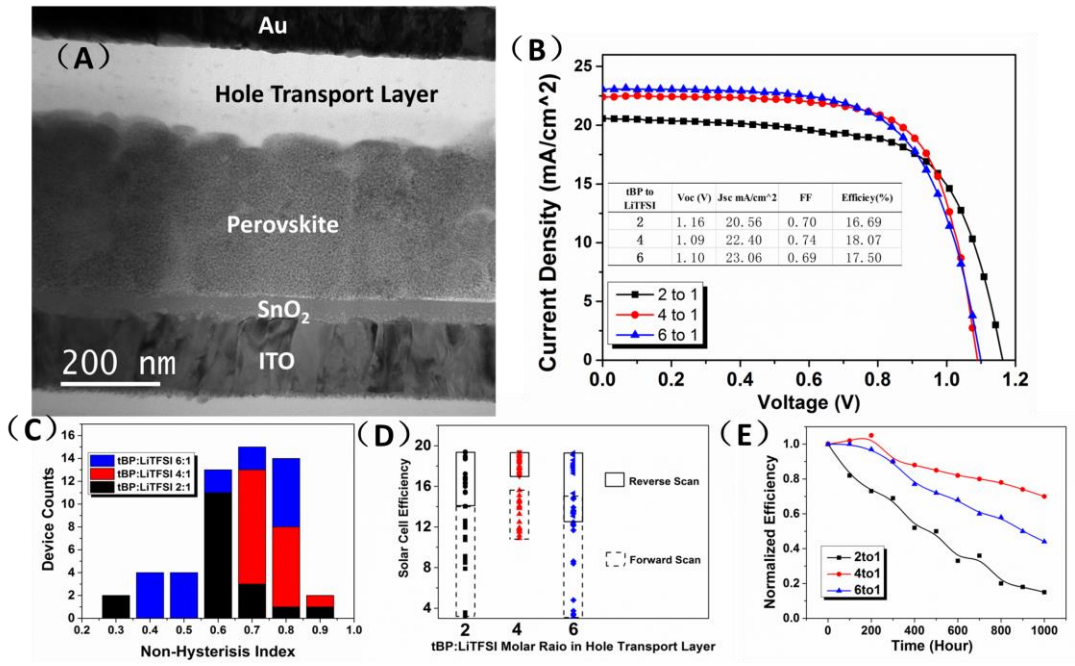

Figure 7.13 PSC Performance Results for 54 devices (18 devices for each condition) fabricated with different tBP:LiTFSI ratio: (A) BF-TEM Cross-Section Image of the PSC; (B) Reverse scan J-V curves (C) Non-Hysteresis Index distribution; (D) Distribution of individual device performance; (E) Aging curves of the devices for 1000 hours in ambient condition

All physical and chemical analyses suggest the complex formation improves PSCs stability. The planar PSCs[65] were fabricated to test and understand the impact of these complexes on devices. In Figure 7.13(A), the Bright-Field Transmission Electron Microscopy (BF-TEM) image displays the device we fabricated. The PSCs consist of amorphous SnO_2 as a compact electron transport layer, the planer $CH_3NH_3PbI_3$ intrinsic layer, Spiro-OMeTAD, tBP and LiTFSI HTL, and gold back contact. Over 54 solar cells were fabricated in order to get statistically significant results. As shown in Figure 7.13(B), the devices fabricated with the 4:1 tBP-LiTFSI mixture shows a slightly higher performance based on the average J-V curve. On the other hand,

the 4:1 tBP-LiTFSI displayed less hysteresis from Figure 7.13(C). The devices' hysteresis was evaluated according to the Non-Hysteresis Index, which is the ratio of area under the J-V curve for forward scan versus reverse scan. The closer the index is to 1, the less hysteresis exists in the device. Moreover, the devices which were fabricated with the 4:1 tBP-LiTFSI mixture have less performance variation than the other two conditions. All device efficiency is shown in Figure 7.13 (D). Although in Figure 7.13 (B), the 4:1 tBP-LiTFSI mixture devices show a slightly higher average performance, champion cells for all three conditions reach over 19.5% efficiency in Figure 7.13 (D). It means that all the best devices have the capability to reach the same level no matter which tBP:LiTFSI ratio is applied. However, their variations in the performance are completely different: The 4:1 tBP-LiTFSI PSCs shows much less efficiency variation than the other two devices in both forward and reverse scans. Together with the less variation of hysteresis in Figure 7.13(C), the 4:1 tBP-LiTFSI PSCs have much higher reproducibility than the other two conditions. It can be attributed to the fact that the 4:1 ratio reaches the condition for reducing both corrosive and hyperactivity effect: it has less corrosivity to perovskite compared with the 6:1 samples since it does not contain un-complexed tBP and it has lower hygroscopicity compared with the 2:1 samples for the less LiTFSI component.

To evaluate the impact of devices stability for the tBP:LiTFSI complexes, all devices which had over 16% efficiency at the initial test were stored in a light ambient condition and tested over 1000 hours. The devices, which were fabricated with the 4:1 tBP-LiTFSI mixtures, displayed the highest stability. For the 4:1 tBP-LiTFSI devices, the final efficiency dropped to 70% compared with the initial test, while the 2:1 tBP-LiTFSI devices dropped to 15% and the 6:1 tBP-LiTFSI devices dropped to 44%. This result agrees with physical and chemical properties of the 4:1 mixture: In a device, the 4:1 tBP-LiTFSI mixture minimized the corrossivity to

perovskite and has less hygroscopicity than the other two conditions. It indicates that the 6:1 tBP-LiTFSI, which is always applied in PSCs may not be the optimized ratio, instead, the 4:1 tBP-LiTFSI shows better results with less hysteresis, higher stability, and more consistent device performances. All the differences in device performance can be correlated to how the pyridine ring coordinates with lithium ion in molecular level.

7.4 Conclusion

Three tBP-LiTFSI mixtures (tBP: LiTFSI molar ratio is 2:1, 4:1, and 6:1, respectively) were synthesized, which displayed different physical, chemical, and spectroscopic properties. The formation of tBP-LiTFSI complexes can be attributed to pyridine ring (tBP) coordinated with lithium ion (LiTFSI). Upon formation of tBP-LiTFSI complex (A and B), both LiTFSI hygroscopicity and tBP evaporation are alleviated, which result in less water uptake, corrosion, and formation of PbO in perovskite solar cells. Our observation explains why each of the two components makes PSCs unstable, but when they are mixed at the certain ratio, the negative effects are mitigated. FTIR indicates the 4:1 tBP-LiTFSI mixture only contains complexed tBP, without un-complexed tBP. In principle, it is a better ratio than the empirical 6:1 ratio, which is prevalent in PSC device fabrication. In practice, the 4:1 tBP-LiTFSI devices show higher stability, less hysteresis, and less performance variations. Therefore, the 4:1 tBP-LiTFSI mixture is suggested as the “golden ratio” for PSCs: It forms a correct chemical complex to limit the negative effects of tBP and LiTFSI while maintaining the positive aspects of these materials in PSCs. It is surprising that the intermolecular behavior between pyridine ring (tBP) and lithium ion (LiTFSI) can result in such a significant difference in perovskite/HTL interface, finally reflected in device performance. Understanding the formation of tBP-LiTFSI complexes and

their influences in perovskite solar cells can help the rational design of suitable HTL additives, which will further improve the PSCs performance.

This Chapter, in full, is a reprint of the material “tBP-LiTFSI Complexes in Perovskite Solar Cells”, Wang, S., Huang, Z., Wang, X., Li, Y., Günther, M., Valenzuela, S., Parikh, P., Xiong, W., Meng, Y. S., 2018 (in prepration). The dissertation author was the primary investigator and first author of this paper. All of the experiment parts were performed by the author except for the XPS.

Chapter 8. Summary and Outlook

With the dramatic increase of energy conversion efficiency over 22%, PSCs have been one of the most promising new-generation photovoltaic devices. Current issue for the commercialization of PSCs is the device stability instead of efficiency. According to our research, it is the hole transport layer instead of the perovskite intrinsic layer that is the bottleneck to limit the device stability: The hole transport layer is on top of the perovskite layer in a regular configuration and interacts with the moisture and oxygen first. If the stability of this layer is enhanced, the potential unstable factors can be prevented before they contact/interact with the perovskite layer. That is why it is crucial to understand the functions and working mechanisms of the hole transport layer components in PSCs which can help with the development of stable PSCs without sacrificing the efficiency.

In Chapter 5, we mainly focused on the interactions between LiTFSI, Spiro-OMeTAD and perovskite layer. We demonstrated a spectrum-dependent mechanism for the generation of oxidized Spiro-OMeTAD in a perovskite solar cell and observed its influence on the solar cell performance. Photons are participating in the reaction. In a short wavelength range (from 380 to 450 nm), perovskite is unnecessary for the Spiro-OMeTAD oxidation while in a long wavelength range (> 450 nm), the oxidation reaction can only proceed with the assistance of perovskite. The product, oxidized Spiro-OMeTAD, can improve the conductivity of the hole transport layer, and enhance the charge transfer at the Au/Spiro-OMeTAD interface. On the other hand, it also increases the charge recombination at TiO_2/Spiro-OMeTAD interface. As a result, the initial illumination of a perovskite solar cell can enhance the efficiency; however the longer illumination times can reduce the efficiency of PSC. A better interfacial engineering method to

hinder the charge recombination at TiO_2/Spiro-OMeTAD interface, while allowing increased generation of oxidized Spiro-OMeTAD would ensure higher perovskite solar cell efficiency.

In Chapter 6, we discussed the influence of tBP on Spiro-OMeTAD and LiTFSI in PSCs. The function of tBP in PSCs was re-evaluated compared to DSSCs to understand its influence on device stability. Due to the limited penetration depth of HTL into mesoporous TiO_2, it is unlikely that the additive serves only to prevent contact between the Spiro-OMeTAD and TiO_2 layers as traditionally assumed. Based on our observations, tBP functions as a morphological controller for the HTL. It prevents phase separation of LiTFSI and Spiro-OMeTAD during spin-coating of the solution, resulting in a uniform HTL film. The absence of tBP leads to inhomogeneous films and also causes the appearance of large pits on the surface of the HTL. tBP-free HTL easily absorbs water due to the hygroscopicity of accumulated LiTFSI and further lowers the stability of PSCs. In PSCs stored in ambient dark conditions for 1000 hours, the slow evaporation of tBP (as it is the only liquid component in PSCs), leads to all of the above discussed phenomena. Li salt accumulates and generates 'dark regions' in the HTL. These dark regions then turn into void bubble structures due to the hydration of Li salt. Finally, the water contained in the HTL contributes to perovskite degradation. Since the evaporation of tBP is a primary contributor to the poor stability of PSCs, we suggest that the performance of PSCs can be enhanced by utilizing new additives that can fulfill the same functions as tBP but have much higher boiling points.

In Chapter 7, we are mainly focusing on the combined effect of tBP-LiTFSI complexes in PSCs. Three tBP-LiTFSI mixtures (tBP: LiTFSI molar ratio is 2:1, 4:1, and 6:1, respectively) were synthesized, which displayed different physical, chemical, and spectroscopic properties. The formation of tBP-LiTFSI complexes can be attributed to pyridine ring (tBP) coordinated with lithium ion (LiTFSI). Upon formation of tBP-LiTFSI complex (A and B), both LiTFSI

hygroscopicity and tBP evaporation are alleviated, which result in less water uptake, corrosion, and formation of PbO in perovskite solar cells. Our observation explains why each of the two components makes PSCs unstable, but when they are mixed at the certain ratio, the negative effects are mitigated. FTIR indicates the 4:1 tBP-LiTFSI mixture only contains complexed tBP, without uncomplexed tBP. In principle, it is a better ratio than the empirical 6:1 ratio, which is prevalent in PSC device fabrication. In practice, the 4:1 tBP-LiTFSI devices show higher stability, less hysteresis, and less performance variations. Therefore, the 4:1 tBP-LiTFSI mixture is suggested as the "golden ratio" for PSCs: It forms the correct chemical complex to limit the negative effects of tBP and LiTFSI while maintaining the positive aspects of these materials in PSCs. It is surprising that the intermolecular behavior between pyridine ring (tBP) and lithium ion (LiTFSI) can result in such a significant difference in perovskite/HTL interface, finally reflected in device performance. Understanding the formation of tBP-LiTFSI complexes and their influences in perovskite solar cells can help the rational design of suitable HTL additives, which will further improve the PSCs performance.

According to the above mentioned researches, it is clear to state that the PSCs stability is much relevant to the components in HTL. By understanding the functions for these components in HTL, the future study to enhancing the stability of PSCs by tuning the HTL components can be focused on several different aspects:

For the hole transport materials, inorganic materials generally have better stability than organic materials. By substitute the organic materials to inorganics, the higher stability PSCs is achievable. Recently, inorganic materials such as CuSCN, NiO_x, and CuI have been applied as the HTL show better stability and comparable efficiency to the organic HTL-based PSCs. How to further improve the interfacial contact between the inorganic HTL/perovskite interface is

crucial to get the PSCs with higher efficiency. On the other hand, some of the inorganic HTL such as NiOx requires high annealing temperature (600 ℃), to seek low temperature synthesis for these type of HTL is significant. It can extend the application of these type of materials in different PSCs configurations.

For organic-based HTL, there are two different procedures to improve the stability. The first procedure is to develop the dopant-free organic based HTL. It requires the rational design of new organic molecules to meet all requirements. Cost could be one of the major issues for this procedure due to the multiple synthesis and purification steps. Several new doppant-free organic HTL PSCs have shown high efficiency, but still, have a long way to go to reduce the cost of the materials. Another procedure for the organic-based HTL is to seek new HTL additives to substitute tBP and LiTFSI. This can be considered as the relative simple procedure. Pyridine-based polymers could be the perfect candidates to substitute tBP for the similar functional group. With higher boiling point and non-corrosive effect to perovskite, polymer pyridine materials could help with the enhancement of the stability of PSCs. On LiTFSI part, it is rational to design some organic ligands to coordinate with Li ion in order to prevent the hydration of LiTFSI. The new Lewis acid-base pairs to substitute tBP and LiTFSI will maintain the devices performance while increasing the performance.

Generally, higher stability of PSCs is achievable by introducing rationally designed HTL components. The high stability HTL can be considered as both the HTL to conduct holes from perovskite and the encapsulation layer to protect the contact of oxygen/moisture from the ambient to perovskite layer. With the improved device stability, high performance，and cheap manufacturing cost, the PSCs have a bright future to go to market to finally substitute fossil fuel and change the world, and our life.

References

(1) Daly, H. *Appl. Energy* **1994**, *47* (2–3), 101–121.

(2) US Department of Energy. Greenhouse gas emissions https://www.eia.gov/energyexplained/index.cfm?page=environment_how_ghg_affect_climate (accessed May 10, 2018).

(3) Morton, O. *Nature* **2006**, *443*, 19–22.

(4) IEA. World Energy Outlook 2017 https://www.iea.org/weo2017/ (accessed Apr 10, 2018).

(5) APS. Bell Labs Demonstrates the First Practical Silicon Solar Cell https://www.aps.org/publications/apsnews/200904/physicshistory.cfm (accessed Apr 10, 2018).

(6) Green, M. a. *1996 Conf. Optoelectron. Microelectron. Mater. Devices. Proc.* **1996**, *3894* (October 1999), 65–75.

(7) Chopra, K. L.; Paulson, P. D.; Dutta, V. *Prog. Photovoltaics Res. Appl.* **2004**, *12* (23), 69–92.

(8) Bagnall, D. M.; Boreland, M. *Energy Policy* **2008**, *36* (12), 4390–4396.

(9) Conibeer, G. In *Solar Cell Materials: Developing Technologies*; 2014; pp 283–314.

(10) NREL Efficiency Chart. http://www.nrel.gov/ncpv/images/efficiency_chart.jpg (accessed May 2, 2018).

(11) Kojima, A.; Teshima, K.; Shirai, Y.; Miyasaka, T. *J. Am. Chem. Soc.* **2009**, *131*, 6050–6051.

(12) Wang, D.; Wright, M.; Elumalai, N. K.; Uddin, A. *Sol. Energy Mater. Sol. Cells* **2016**, *147*, 255–275.

(13) Ono, L. K.; Juarez-Perez, E. J.; Qi, Y. *ACS Appl. Mater. Interfaces* **2017**, *9* (36), 30197–30246.

(14) O'Regan, B.; Grätzel, M. *Nature* **1991**, *353* (6346), 737–740.

(15) Chung, I.; Lee, B.; He, J.; Chang, R. P. H.; Kanatzidis, M. G. *Nature* **2012**, *485* (7399), 486–489.

(16) Lee, M. M.; Teuscher, J.; Miyasaka, T.; Murakami, T. N.; Snaith, H. J. *Science.* **2012**, *338* (6107), 643–647.

(17) Liu, M.; Johnston, M. B.; Snaith, H. J. *Nature* **2013**, *501*, 395–398.

(18) Burschka, J.; Pellet, N.; Moon, S.-J.; Humphry-Baker, R.; Gao, P.; Nazeeruddin, M. K.; Grätzel, M. *Nature* **2013**, *499*, 316–320.

(19) Docampo, P.; Ball, J. M.; Darwich, M.; Eperon, G. E.; Snaith, H. J. *Nat. Commun.* **2013**, *4*, 2761–2766.

(20) Nie, W.; Tsai, H.; Asadpour, R.; Blancon, J. C.; Neukirch, A. J.; Gupta, G.; Crochet, J. J.; Chhowalla, M.; Tretiak, S.; Alam, M. A.; Wang, H. L.; Mohite, A. D. *Science.* **2015**, *347* (6221), 522–525.

(21) Laban, W. A.; Etgar, L. *Energy Environ. Sci.* **2013**, *6* (11), 3249–3253.

(22) Jiang, X.; Xiong, Y.; Mei, A.; Rong, Y.; Hu, Y.; Hong, L.; Jin, Y.; Liu, Q.; Han, H. *J. Phys. Chem. Lett.* **2016**, *7* (20), 4142–4146.

(23) McMeekin, D. P.; Sadoughi, G.; Rehman, W.; Eperon, G. E.; Saliba, M.; Hörantner, M. T.; Haghighirad, A.; Sakai, N.; Korte, L.; Rech, B.; Johnston, M. B.; Herz, L. M.; Snaith, H. J. *Science.* **2016**, *351* (6269), 151–155.

(24) Yang, G.; Tao, H.; Qin, P.; Ke, W.; Fang, G. *J. Mater. Chem. A* **2016**, *4* (11), 3970–3990.

(25) Marchioro, A.; Teuscher, J.; Friedrich, D.; Kunst, M.; van de Krol, R.; Moehl, T.; Grätzel, M.; Moser, J.-E. *Nat Phot.* **2014**, *8(3)*, 250–255.

(26) Snaith, H. J.; Abate, A.; Ball, J. M.; Eperon, G. E.; Leijtens, T.; Noel, N. K.; Stranks, S. D.; Wang, J. T. W.; Wojciechowski, K.; Zhang, W. *J. Phys. Chem. Lett.* **2014**, *5* (9), 1511–1515.

(27) Zhang, T.; Chen, H.; Bai, Y.; Xiao, S.; Zhu, L.; Hu, C.; Xue, Q.; Yang, S. *Nano Energy* **2016**, *26*, 620–630.

(28) Wei, J.; Zhao, Y.; Li, H.; Li, G.; Pan, J.; Xu, D.; Zhao, Q.; Yu, D. *J. Phys. Chem. Lett.* **2014**, *5* (21), 3937–3945.

(29) Li, Z.; Xiao, C.; Yang, Y.; Harvey, S. P.; Kim, D. H.; Christians, J. A.; Yang, M.; Schulz, P.; Nanayakkara, S. U.; Jiang, C.-S.; Luther, J. M.; Berry, J. J.; Beard, M. C.; Al-Jassim, M. M.; Zhu, K. *Energy Environ. Sci.* **2017**, *10* (5), 1234–1242.

(30) Wang, Q.; Shao, Y.; Xie, H.; Lyu, L.; Liu, X.; Gao, Y.; Huang, J. *Appl. Phys. Lett.* **2014**, *105* (16), 163508.

(31) Eames, C.; Frost, J. M.; Barnes, P. R. F.; O'Regan, B. C.; Walsh, A.; Islam, M. S. *Nat. Commun.* **2015**, *6*, 7497.

(32) Jung, H. S.; Park, N.-G. *Small* **2014**, *11(1)*, 10–25.

(33) Xiao, Z.; Zhou, Y.; Hosono, H.; Kamiya, T.; Padture, N. P. *Chem. - A Eur. J.* **2018**, *24* (10), 2305–2316.

(34) Huang, J.; Yuan, Y.; Shao, Y.; Yan, Y. *Nat. Rev. Mater.* **2017**, *2* (7), 17042.

(35) Quarti, C.; Mosconi, E.; Ball, J. M.; D'Innocenzo, V.; Tao, C.; Pathak, S.; Snaith, H. J.; Petrozza, A.; De Angelis, F. *Energy Environ. Sci.* **2016**, *9* (1), 155–163.

(36) Luo, Y.; Khoram, P.; Brittman, S.; Zhu, Z.; Lai, B.; Ong, S. P.; Garnett, E. C.; Fenning, D. P. *Adv. Mater.* **2017**, *29* (43), 1703451.

(37) Kato, Y.; Ono, L. K.; Lee, M. V.; Wang, S.; Raga, S. R.; Qi, Y. *Adv. Mater. Interfaces* **2015**, *2* (13), 1500195.

(38) Tang, S.; Deng, Y.; Zheng, X.; Bai, Y.; Fang, Y.; Dong, Q.; Wei, H.; Huang, J. *Adv. Energy Mater.* **2017**, *7* (18), 1700302.

(39) Moore, D. T.; Sai, H.; Tan, K. W.; Smilgies, D. M.; Zhang, W.; Snaith, H. J.; Wiesner, U.; Estroff, L. A. *J. Am. Chem. Soc.* **2015**, *137* (6), 2350–2358.

(40) Song, T.; Chen, Q.; Zhou, H. H.-P.; Jiang, C.; Wang, H.-H.; (Michael) Yang, Y.; Liu, Y.; You, J.; Yang, Y.; Liu, Y.; You, J.; (Michael) Yang, Y.; Liu, Y.; You, J.; Yang, Y. *J. Mater. Chem. A* **2015**, *3* (17), 9032–9050.

(41) Zhou, Y.; Yang, M.; Wu, W.; Vasiliev, A. L.; Zhu, K.; Padture, N. P. *J. Mater. Chem. A* **2015**, *3* (15), 8178–8184.

(42) Jeon, N. J.; Noh, J. H.; Kim, Y. C.; Yang, W. S.; Ryu, S.; Seok, S. Il. *Nat. Mater.* **2014**, *13* (9), 897–903.

(43) Lee, J. W.; Kim, H. S.; Park, N. G. *Acc. Chem. Res.* **2016**, *49* (2), 311–319.

(44) Liu, Z.; Hu, J.; Jiao, H.; Li, L.; Zheng, G.; Chen, Y.; Huang, Y.; Zhang, Q.; Shen, C.; Chen, Q.; Zhou, H. *Adv. Mater.* **2017**, *29* (23), 1606774.

(45) Zhou, Z.; Wang, Z.; Zhou, Y.; Pang, S.; Wang, D.; Xu, H.; Liu, Z.; Padture, N. P.; Cui, G. *Angew. Chemie Int. Ed.* **2015**, *54* (33), 9705–9709.

(46) Yang, W. S.; Park, B. W.; Jung, E. H.; Jeon, N. J.; Kim, Y. C.; Lee, D. U.; Shin, S. S.; Seo, J.; Kim, E. K.; Noh, J. H.; Seok, S. Il. *Science.* **2017**, *356* (6345), 1376–1379.

(47) Zhao, Y.; Wei, J.; Li, H.; Yan, Y.; Zhou, W.; Yu, D.; Zhao, Q. *Nat. Commun.* **2016**, *7*, 10228.

(48) Zuo, L.; Guo, H.; DeQuilettes, D. W.; Jariwala, S.; De Marco, N.; Dong, S.; DeBlock, R.; Ginger, D. S.; Dunn, B.; Wang, M.; Yang, Y. *Sci. Adv.* **2017**, *3* (8), 1700106.

(49) Chen, Q.; Zhou, H.; Song, T. Bin; Luo, S.; Hong, Z.; Duan, H. S.; Dou, L.; Liu, Y.; Yang, Y. *Nano Lett.* **2014**, *14* (7), 4158–4163.

(50) Wang, Q.; Chen, B.; Liu, Y.; Deng, Y.; Bai, Y.; Dong, Q.; Huang, J. *Energy Environ. Sci.* **2017**, *10* (2), 516–522.

(51) Huang, W.; Manser, J. S.; Kamat, P. V.; Ptasinska, S. *Chem. Mater.* **2016**, *28* (1), 303–311.

(52) Kim, B. J.; Kim, D. H.; Kwon, S. L.; Park, S. Y.; Li, Z.; Zhu, K.; Jung, H. S. *Nat. Commun.* **2016**, *7*, 11735–11743.

(53) Bryant, D.; Aristidou, N.; Pont, S.; Sanchez-Molina, I.; Chotchunangatchaval, T.; Wheeler, S.; Durrant, J. R.; Haque, S. A. *Energy Environ. Sci.* **2016**, *9* (5), 1655–1660.

(54) Cappel, U. B.; Daeneke, T.; Bach, U. *Nano Lett.* **2012**, *12*, 4925–4931.

(55) Abate, A.; Leijtens, T.; Pathak, S.; Teuscher, J.; Avolio, R.; Errico, M. E.; Kirkpatrik, J.; Ball, J. M.; Docampo, P.; McPherson, I.; Snaith, H. J. *Phys. Chem. Chem. Phys.* **2013**, *15* (7), 2572–2579.

(56) Wang, S.; Yuan, W.; Meng, Y. S. *ACS Appl. Mater. Interfaces* **2015**, *7*, 24791–24798.

(57) Wang, S.; Jiang, Y.; Juarez-Perez, E. J.; Ono, L. K.; Qi, Y. *Nat. Energy* **2016**, *2* (1), 16195–16202.

(58) Qin, C.; Matsushima, T.; Fujihara, T.; Potscavage, W. J.; Adachi, C. *Adv. Mater.* **2016**, *28* (3), 466–471.

(59) Tsai, H.; Asadpour, R.; Blancon, J. C.; Stoumpos, C. C.; Durand, O.; Strzalka, J. W.; Chen, B.; Verduzco, R.; Ajayan, P. M.; Tretiak, S.; Even, J.; Alam, M. A.; Kanatzidis, M. G.; Nie, W.; Mohite, A. D. *Science.* **2018**, *360* (6384), 67–70.

(60) Wang, S.; Sina, M.; Parikh, P.; Uekert, T.; Shahbazian, B.; Devaraj, A.; Meng, Y. S. *Nano Lett.* **2016**, *16* (9), 5594–5600.

(61) Qin, P.; Paulose, M.; Dar, M. I.; Moehl, T.; Arora, N.; Gao, P.; Varghese, O. K.; Grätzel, M.; Nazeeruddin, M. K. *Small* **2015**, *11* (41), 5533–5539.

(62) Salado, M.; Oliva-Ramirez, M.; Kazim, S.; González-Elipe, A. R.; Ahmad, S. *Nano Energy* **2017**, *35*, 215–222.

(63) Fu, F.; Feurer, T.; Jäger, T.; Avancini, E.; Bissig, B.; Yoon, S.; Buecheler, S.; Tiwari, A. N. *Nat. Commun.* **2015**, *6*, 8932.

(64) Bao, Q.; Liu, X.; Braun, S.; Fahlman, M. *Adv. Energy Mater.* **2014**, *4* (6), 1301272–1301278.

(65) Zhang, D.; Cui, B.-B.; Zhou, C.; Li, L.; Chen, Y.; Zhou, N.; Xu, Z.; Li, Y.; Zhou, H.; Chen, Q. *Chem. Commun.* **2017**, *53*, 10548–10551.

(66) Mahmood, K.; Sarwar, S.; Mehran, M. T. *RSC Adv.* **2017**, *7* (28), 17044–17062.

(67) Giordano, F.; Abate, A.; Correa Baena, J. P.; Saliba, M.; Matsui, T.; Im, S. H.; Zakeeruddin, S. M.; Nazeeruddin, M. K.; Hagfeldt, A.; Graetzel, M. *Nat. Commun.* **2016**, *7*, 10379.

(68) You, J.; Meng, L.; Song, T.-B.; Guo, T.-F.; Yang, Y. (Michael); Chang, W.-H.; Hong, Z.; Chen, H.; Zhou, H.; Chen, Q.; Liu, Y.; De Marco, N.; Yang, Y. *Nat. Nanotechnol.* **2015**, *11*, 1–8.

(69) Ke, W.; Fang, G.; Liu, Q.; Xiong, L.; Qin, P.; Tao, H.; Wang, J.; Lei, H.; Li, B.; Wan, J.; Yang, G.; Yan, Y. *J. Am. Chem. Soc.* **2015**, *137* (21), 6730–6733.

(70) Yang, X.; Wang, H.; Cai, B.; Yu, Z.; Sun, L. *J. Energy Chem.* **2018**, *27* (3), 650–672.

(71) Ball, J. M.; Lee, M. M.; Hey, A.; Snaith, H. J. *Energy Environ. Sci.* **2013**, *6*, 1739–1743.

(72) Bakr, Z. H.; Wali, Q.; Fakharuddin, A.; Schmidt-Mende, L.; Brown, T. M.; Jose, R. *Nano Energy* **2017**, *34*, 271–305.

(73) Christians, J. A.; Schulz, P.; Tinkham, J. S.; Schloemer, T. H.; Harvey, S. P.; Tremolet de Villers, B. J.; Sellinger, A.; Berry, J. J.; Luther, J. M. *Nat. Energy* **2018**, *3* (1), 68–74.

(74) Yang, W. S.; Noh, J. H.; Jeon, N. J.; Kim, Y. C.; Ryu, S.; Seo, J.; Seok, S. Il. *Science.* **2015**, *348*, 1234–1237.

(75) Habisreutinger, S. N.; Leijtens, T.; Eperon, G. E.; Stranks, S. D.; Nicholas, R. J.; Snaith, H. J. *Nano Lett.* **2014**, *14* (10), 5561–5568.

(76) Arora, N.; Dar, M. I.; Hinderhofer, A.; Pellet, N.; Schreiber, F.; Zakeeruddin, S. M.; Grätzel, M. *Science.* **2017**, *358* (6364), 768–771.

(77) Reyntjens, S.; Puers, R. *J. Micromechanics Microengineering* **2001**, *11* (4), 287–300.

(78) Gierak, J. *Semicond. Sci. Technol.* **2009**, *24* (4), 43001.

(79) Alvarado, J.; Ma, C.; Wang, S.; Nguyen, K.; Kodur, M.; Meng, Y. S. *ACS Appl. Mater. Interfaces* **2017**, *9* (31), 26518–26530.

(80) Ying, D. Fundamental Theory of Transmission Electronic Microscopy http://www.nanoscience.gatech.edu/zlwang/research/tem.html (accessed Apr 30, 2018).

(81) Wang, Z.; Santhanagopalan, D.; Zhang, W.; Wang, F.; Xin, H. L.; He, K.; Li, J.; Dudney, N.; Meng, Y. S. *Nano Lett.* **2016**, *16* (6), 3760–3767.

(82) Xu, X.; Chen, Q.; Hong, Z.; Zhou, H.; Liu, Z.; Chang, W. H.; Sun, P.; Chen, H.; Marco, N. De; Wang, M.; Yang, Y. *Nano Lett.* **2015**, *15*, 6514–6520.

(83) Zhou, H.; Chen, Q.; Li, G.; Luo, S.; Song, T. -b.; Duan, H.-S.; Hong, Z.; You, J.; Liu, Y.; Yang, Y. *Science.* **2014**, *345* (6196), 542–546.

(84) Mei, A.; Li, X.; Liu, L.; Ku, Z.; Liu, T.; Rong, Y.; Xu, M.; Hu, M.; Chen, J.; Yang, Y.; Grätzel, M.; Han, H. *Science.* **2014**, *345* (6194), 295–298.

(85) Park, N. G. *Mater. Today* **2015**, *18* (2), 65–72.

(86) Abate, A.; Planells, M.; Hollman, D. J.; Barthi, V.; Chand, S.; Snaith, H. J.; Robertson, N. *Phys. Chem. Chem. Phys.* **2015**, *17* (4), 2335–2338.

(87) Kim, H. S.; Lee, C. R.; Im, J. H.; Lee, K. B.; Moehl, T.; Marchioro, A.; Moon, S. J.; Humphry-Baker, R.; Yum, J. H.; Moser, J. E.; Grätzel, M.; Park, N. G. *Sci. Rep.* **2012**, *2*, 591.

(88) Kwon, Y. S.; Lim, J.; Song, I.; Song, I. Y.; Shin, W. S.; Moon, S.-J.; Park, T. *J. Mater. Chem.* **2012**, *22* (17), 8641–8648.

(89) Burschka, J.; Dualeh, A.; Kessler, F.; Baranoff, E.; Cevey-Ha, N. L.; Yi, C.; Nazeeruddin, M. K.; Grätzel, M. *J. Am. Chem. Soc.* **2011**, *133* (45), 18042–18045.

(90) Yang, L.; Cappel, U. B.; Unger, E. L.; Karlsson, M.; Karlsson, K. M.; Gabrielsson, E.; Sun, L.; Boschloo, G.; Hagfeldt, A.; Johansson, E. M. J. *Phys. Chem. Chem. Phys.* **2012**, *14* (2), 779–789.

(91) Cells, S. D. S.; Leijtens, T.; Ding, I.-K.; Giovenzana, T.; Bloking, J. T.; McGehee, M. D.; Sellinger, A. *ACS Nano* **2012**, *6* (2), 1455–1462.

(92) Marinova, N.; Tress, W.; Humphry-Baker, R.; Dar, M. I.; Bojinov, V.; Zakeeruddin, S. M.; Nazeeruddin, M. K.; Grätzel, M. *ACS Nano* **2015**, *9* (4), 4200–4209.

(93) Hawash, Z.; Ono, L. K.; Raga, S. R.; Lee, M. V.; Qi, Y. *Chem. Mater.* **2015**, *27*, 562–569.

(94) Yang, L.; Xu, B.; Bi, D.; Tian, H.; Boschloo, G.; Sun, L.; Hagfeldt, A.; Johansson, E. M. J. *J. Am. Chem. Soc.* **2013**, *135* (19), 7378–7385.

(95) Kazim, S.; Nazeeruddin, M. K.; Grätzel, M.; Ahmad, S. *Angew. Chemie - Int. Ed.* **2014**, *53* (11), 2812–2824.

(96) Yuan, W.; Zhao, H.; Hu, H.; Wang, S.; Baker, G. L. *ACS Appl. Mater. Interfaces* **2013**, *5*, 4155–4161.

(97) Kopidakis, N.; Benkstein, K. D.; van de Lagemaat, J.; Frank, A. J. *J. Phys. Chem. B* **2003**, *107* (41), 11307–11315.

(98) Yu, Q.; Wang, Y.; Yi, Z.; Zu, N.; Zhang, J.; Zhang, M.; Wang, P. *ACS Nano* **2010**, *4* (10), 6032–6038.

(99) Jennings, J. R.; Wang, Q. *J. Phys. Chem. C* **2010**, *114* (3), 1715–1724.

(100) Abate, A.; Leijtens, T.; Pathak, S.; Teuscher, J.; Avolio, R.; Errico, M. E.; Kirkpatrik, J.; Ball, J. M.; Docampo, P.; McPherson, I.; Snaith, H. J. *Phys. Chem. Chem. Phys.* **2013**, *15* (7), 2572–2579.

(101) Nguyen, W. H.; Bailie, C. D.; Unger, E. L.; McGehee, M. D. *J. Am. Chem. Soc.* **2014**, *136*, 10996–11001.

(102) Tiwana, P.; Docampo, P.; Johnston, M. B.; Herz, L. M.; Snaith, H. J. *Energy Environ. Sci.* **2012**, *5* (11), 9566–9573.

(103) Im, J.-H.; Lee, C.-R.; Lee, J.-W.; Park, S.-W.; Park, N.-G. *Nanoscale* **2011**, *3* (10), 4088–4093.

(104) Fantacci, S.; De Angelis, F.; Nazeeruddin, M. K.; Grätzel, M. *J. Phys. Chem. C* **2011**, *115* (46), 23126–23133.

(105) Hao, F.; Stoumpos, C. C.; Chang, R. P. H.; Kanatzidis, M. G. *J. Am. Chem. Soc.* **2014**, *136* (22), 8094–8099.

(106) Guarnera, S.; Abate, A.; Zhang, W.; Foster, J. M.; Richardson, G.; Petrozza, A.; Snaith, H. J. *J. Phys. Chem. Lett.* **2015**, *6* (3), 432–437.

(107) Xiao, Y.; Han, G.; Chang, Y.; Zhang, Y.; Li, Y.; Li, M. *J. Power Sources* **2015**, *286*, 118–123.

(108) Kim, H. S.; Lee, J. W.; Yantara, N.; Boix, P. P.; Kulkarni, S. A.; Mhaisalkar, S.; Grätzel, M.; Park, N. G. *Nano Lett.* **2013**, *13*, 2412–2417.

(109) Kaltenbrunner, M.; Adam, G.; Głowacki, E. D.; Drack, M.; Schwödiauer, R.; Leonat, L.; Apaydin, D. H.; Groiss, H.; Scharber, M. C.; White, M. S.; Sariciftci, N. S.; Bauer, S. *Nat. Mater.* **2015**, *14*, 1032–1039.

(110) Yin, X.; Chen, P.; Que, M.; Xing, Y.; Que, W.; Niu, C.; Shao, J. *ACS Nano* **2016**, *10*, 3630–3636.

(111) Li, R.; Xiang, X.; Tong, X.; Zou, J.; Li, Q. *Adv. Mater.* **2015**, *27*, 3831–3835.

(112) Edri, E.; Kirmayer, S.; Henning, A.; Mukhopadhyay, S.; Gartsman, K.; Rosenwaks, Y.; Hodes, G.; Cahen, D. *Nano Lett.* **2014**, *14*, 1000–1004.

(113) Xiao, Z.; Yuan, Y.; Shao, Y.; Wang, Q.; Dong, Q.; Bi, C.; Sharma, P.; Gruverman, A.; Huang, J. *Nat. Mater.* **2014**, *14*, 1–18.

(114) Choi, H.; Mai, C.-K.; Kim, H.-B.; Jeong, J.; Song, S.; Bazan, G. C.; Kim, J. Y.; Heeger, A. J. *Nat. Commun.* **2015**, *6*, 7348.

(115) Liu, Y.; Chen, Q.; Duan, H.-S.; Zhou, H.; Yang, Y.; Chen, H.; Luo, S.; Song, T.-B.; Dou, L.; Hong, Z.; Yang, Y. *J. Mater. Chem. A* **2015**, *3*, 11940–11947.

(116) Krüger, J.; Plass, R.; Cevey, L.; Piccirelli, M.; Grätzel, M.; Bach, U. *Appl. Phys. Lett.* **2001**, *79*, 2085–2087.

(117) Dualeh, A.; Moehl, T.; Tétreault, N.; Teuscher, J.; Gao, P.; Nazeeruddin, M. K.; Grätzel, M. *ACS Nano* **2014**, *8*, 362–373.

(118) Boschloo, G.; Häggman, L.; Hagfeldt, A. *J. Phys. Chem. B* **2006**, *110*, 13144–13150.

(119) Haque, S. A.; Palomares, E.; Cho, B. M.; Green, A. N. M.; Hirata, N.; Klug, D. R.; Durrant, J. R. *J. Am. Chem. Soc.* **2005**, *127*, 3456–3462.

(120) Park, N. G. *J. Phys. Chem. Lett.* **2013**, *4*, 2423–2429.

(121) Jung, M.-C.; Raga, S. R.; Ono, L. K.; Qi, Y. *Sci. Rep.* **2015**, *5*, 9863.

(122) Divitini, G.; Cacovich, S.; Matteocci, F.; Cinà, L.; Di Carlo, A.; Ducati, C. *Nat. Energy* **2016**, *1*, 15012–15017.

(123) Bergmann, V. W.; Weber, S. a. L.; Javier Ramos, F.; Nazeeruddin, M. K.; Grätzel, M.; Li, D.; Domanski, A. L.; Lieberwirth, I.; Ahmad, S.; Berger, R. *Nat. Commun.* **2014**, *5*, 5001.

(124) Nanova, D.; Kast, A. K.; Pfannmöller, M.; Müller, C.; Veith, L.; Wacker, I.; Agari, M.; Hermes, W.; Erk, P.; Kowalsky, W.; Schröder, R. R.; Lovrinčić, R. *Nano Lett.* **2014**, *14*, 2735–2740.

(125) Zhou, Y.; Vasiliev, A. L.; Wu, W.; Yang, M.; Pang, S.; Zhu, K.; Padture, N. P. *J. Phys. Chem. Lett.* **2015**, *6*, 2292–2297.

(126) Docampo, P.; Hey, A.; Guldin, S.; Gunning, R.; Steiner, U.; Snaith, H. J. *Adv. Funct. Mater.* **2012**, *22*, 5010–5019.

(127) Snaith, H. J.; Humphry-Baker, R.; Chen, P.; Cesar, I.; Zakeeruddin, S. M.; Grätzel, M. *Nanotechnology* **2008**, *19*, 424003.

(128) Kim, S.; Jeong Park, M.; Balsara, N. P.; Liu, G.; Minor, A. M. *Ultramicroscopy* **2011**, *111*, 191–199.

(129) Devaraj, A.; Gu, M.; Colby, R.; Yan, P.; Wang, C. M.; Zheng, J. M.; Xiao, J.; Genc, A.; Zhang, J. G.; Belharouak, I.; Wang, D.; Amine, K.; Thevuthasan, S. *Nat. Commun.* **2015**, *6*, 8014.

(130) Santhanagopalan, D.; Schreiber, D. K.; Perea, D. E.; Martens, R. L.; Janssen, Y.; Khalifah, P.; Meng, Y. S. *Ultramicroscopy* **2015**, *148*, 57–66.

(131) Wei, H.; Fang, Y.; Mulligan, P.; Chuirazzi, W.; Fang, H. H.; Wang, C.; Ecker, B. R.; Gao, Y.; Loi, M. A.; Cao, L.; Huang, J. *Nat. Photonics* **2016**, *10* (5), 333–339.

(132) Tan, Z.-K.; Moghaddam, R. S.; Lai, M. L.; Docampo, P.; Higler, R.; Deschler, F.; Price, M.; Sadhanala, A.; Pazos, L. M.; Credgington, D.; Hanusch, F.; Bein, T.; Snaith, H. J.; Friend, R. H. *Nat. Nanotechnol.* **2014**, *9* (9), 687–692.

(133) Sutherland, B. R.; Sargent, E. H. *Nat. Photonics* **2016**, *10* (5), 295–302.

(134) Ergen, O.; Gilbert, S. M.; Pham, T.; Turner, S. J.; Tan, M. T. Z.; Worsley, M. A.; Zettl, A. *Nat. Mater.* **2017**, *16* (5), 522–525.

(135) Leijtens, T.; Giovenzana, T.; Habisreutinger, S. N.; Tinkham, J. S.; Noel, N. K.; Kamino, B. A.; Sadoughi, G.; Sellinger, A.; Snaith, H. J. *ACS Appl. Mater. Interfaces* **2016**, *8* (9), 5981–5989.

(136) Ma, S.; Zhang, H.; Zhao, N.; Cheng, Y.; Wang, M.; Shen, Y.; Tu, G. *J. Mater. Chem. A* **2015**, *3* (23), 12139–12144.

(137) Zhang, J.; Xu, B.; Yang, L.; Mingorance, A.; Ruan, C.; Hua, Y.; Wang, L.; Vlachopoulos, N.; Lira-Cantú, M.; Boschloo, G.; Hagfeldt, A.; Sun, L.; Johansson, E. M. J. *Adv. Energy Mater.* **2017**, *7* (14), 1602736–1602743.

(138) Heo, J. H.; Im, S. H.; Noh, J. H.; Mandal, T. N.; Lim, C. S.; Chang, J. A.; Lee, Y. H.; Kim, H. J.; Sarkar, A.; Nazeeruddin, M. K.; Grätzel, M.; Seok, S. Il. *Nat. Photonics* **2013**, *7* (6), 486–491.

(139) Christians, J. A.; Fung, R. C. M.; Kamat, P. V. *J. Am. Chem. Soc.* **2014**, *136* (2), 758–764.

(140) Wijeyasinghe, N.; Regoutz, A.; Eisner, F.; Du, T.; Tsetseris, L.; Lin, Y. H.; Faber, H.; Pattanasattayavong, P.; Li, J.; Yan, F.; McLachlan, M. A.; Payne, D. J.; Heeney, M.; Anthopoulos, T. D. *Adv. Funct. Mater.* **2017**, *27* (35), 1701818–1701830.

(141) Habisreutinger, S. N.; Noel, N. K.; Snaith, H. J.; Nicholas, R. J. *Adv. Energy Mater.* **2017**, *7* (1), 1601079–1601086.

(142) Juarez-Perez, E. J.; Leyden, M. R.; Wang, S.; Ono, L. K.; Hawash, Z.; Qi, Y. *Chem. Mater.* **2016**, *28* (16), 5702–5709.

(143) Chen, B. A.; Lin, J. T.; Suen, N. T.; Tsao, C. W.; Chu, T. C.; Hsu, Y. Y.; Chan, T. S.; Chan, Y. T.; Yang, J. S.; Chiu, C. W.; Chen, H. M. *ACS Energy Lett.* **2017**, *2* (2), 342–348.

(144) Aristidou, N.; Eames, C.; Sanchez-Molina, I.; Bu, X.; Kosco, J.; Islam, M. S.; Haque, S. A. *Nat. Commun.* **2017**, *8*, 15218–15227.

(145) Li, W.; Dong, H.; Wang, L.; Li, N.; Guo, X.; Li, J.; Qiu, Y. *J. Mater. Chem. A* **2014**, *2*, 13587–13592.

(146) Xi, H.; Tang, S.; Ma, X.; Chang, J.; Chen, D.; Lin, Z.; Zhong, P.; Wang, H.; Zhang, C. *ACS Omega* **2017**, *2* (1), 326–336.

(147) Dong, G.; Xia, D.; Yang, Y.; Shenga, L.; Ye, T.; Fan, R. *ACS Appl. Mater. Interfaces* **2017**, *9* (3), 2378–2386.

(148) Liang, H.; Li, H.; Wang, Z.; Wu, F.; Chen, L.; Huang, X. *J. Phys. Chem. B* **2001**, *105* (41), 9966–9969.

(149) Yurdakul, S.; Bahat, M. *J. Mol. Struct.* **1997**, *412* (1–2), 97–102.

(150) Jones, L. H. *J. Chem. Phys.* **1954**, *22* (2), 217–219.

(151) Foropoulos Jr, J.; DesMarteau, D. D. *Inorg. Chem.* **1984**, *23* (23), 3720–3723.